8-5-2010

Experimental and Computational Investigation of Thermal-Flow Characteristics of Gas Turbine Reverse-Flow Combustor

Liang Wang
University of New Orleans

Experimental and Computational Investigation of Thermal-Flow Characteristics of Gas Turbine Reverse-Flow Combustor

A Thesis

Submitted to the Graduate Faculty of the
University of New Orleans
in partial fulfillment of the
requirements for the degree of

Master of Science
in
Engineering

by

Liang Wang

B.S. Tongji University of China, 2003

August, 2010

ACKNOWLEDGMENT

I would like to give my deepest thanks to my principal advisor Dr. Ting Wang for his sincere patient and thoughtful guidance throughout my three years of study and research with him.. Without his innovative ideas and hard work, there will not be this thesis. I have been privileged and honored to have Dr. Ting Wang as my advisor. I also take this opportunity to thank the other two members of my thesis committee, Dr. Kazim Akyuzlu and Dr. Martin Guillot..

I would also like to thank my colleague students and researchers from Energy Conversion and Conservation Center (ECCC), Dr. Dhanasekaran, Dr. Silaen, Jason Kent, Wayne Bridgeman, Thurmesh Chudasama and Lei Zhao and so many others for their kind help and beneficial discussions.

Lastly, I would like to thank my friends and family for their support and understanding. My heartfelt thanks go to my Dad, Mr. Jianzhong Wang, who is a constant source of inspiration in my whole life. I am also indebted to my Mom, Mrs. Xiaorong Wei, for instilling confidence in me.

TABLE OF CONTENTS

List of Figures vi
List of Tables xi
Nomenclature xiii
Abstract xv
Chapter 1 Introduction 1
1.1 Background 1
1.2 Introduction of reverse-flow combustor 2
1.3 Advantages and Disadvantages of reverse-flow combustor 6
1.4 Motivation and Objective 6
1.5 Approach 7
Chapter 2 Test facility and instrument 8
2.1 Test facilities 8
2.1.1 Wind tunnel system 8
2.1.2 Filter box 10
2.1.3 Blower, motor and variable speed drive 11
2.1.4 Diffuser 12
2.1.5 Heat exchanger and heating/cooling system 13
2.1.6 Screen pack 17
2.1.7 Contraction 19
2.1.8 Suction 23
2.1.9 Test section for reverse-flow combustor study 25
2.2 Instrument 37
2.2.1 Automatic probe traversing system 37
2.2.2 Automatic pressure scanning and data acquisition system 38
2.2.3 Thermocouple measuring and data acquisition system 43
2.2.4 Hot wire anemometry system 46
2.3 Qualification measurement 48
2.3.1 Uniformity of flow 48
2.4 Experiment methodology 50

2.4.1 Velocity and pressure measurements 50
2.4.2 Procedure for adjusting zero and span of signal conditioners 54
2.4.3 Procedure for calibrating pressure transducer 56
2.4.3 Procedure for temperature measurement 60
Chapter 3 Experiment result 62
3.1 The laboratory condition 62
3.2 Calibration 63
3.3 Cold-flow pressure measurement results 67
3.4 Uncertainty analysis of pressure measurements 70
3.5 Temperature measurement results 74
Chapter 4 Computational model 76
4.1 Modeling information 76
4.2 Meshes 78
4.2.1 Grid sensitive study 80
4.3 Physical characteristics of the problem and assumptions 81
4.4 Governing equations 81
4.5 Turbulence model 83
4.6 Boundary condition 88
Chapter 5 Computational result 90
5.1 Computational results and discussions 90
5.1.1 Case 1 (no-sheath, unheated) 91
5.1.2 Case 4 (sheathed, unheated) 97
5.1.3 Case 1(no-sheath, unheated) versus Case 4 (sheathed, unheated) 104
5.1.4 Case 2 (no-sheath, heated) 105
5.1.5 Case 5 (sheathed, heated) 106
5.1.6 Case 2 (no-sheathed, heated) versus Case 5 (sheathed, heated) 107
5.1.7 Case 3 (elevated gas turbine condition, no-sheath) 110
5.1.8 Case 6 (elevated gas turbine condition, sheathed) 114
5.1.9 Case 3 (elevated, no-sheathed) versus Case 6 (elevated, sheathed) 118
Chapter 6 Conclusions 120
6.1 Experiment cases 120

6.1.1 Laboratory condition, fluid mechanics study only 120
6.1.2 Laboratory condition, heat transfer study 120
6.2 Computational cases 121
6.2.1 Laboratory condition CFD simulation, fluid mechanics study only..... 121
6.2.2 Laboratory condition CFD simulation, heat transfer study 121
6.2.3 Real gas turbine condition simulation..... 122
6.3 Future work..... 122
References..... 123
Appendices
Appendix A: Estimate of the heating power needed to experimental test rig..... 125
Appendix B: Heat flux estimation for elevated condition 129
Appendix C: Laboratory pressure measurement data and comparison with the CFD results..... 134
Appendix D: Experimental temperature data and comparison with the CFD results..... 141
Appendix E: Thermocouple temperature measurement instruction..... 147
Vita..... 158

LIST OF FIGURES

Figure 1.1 MS7001EA combustion chamber arrangement 4

Figure 2.1 Plan view of the wind tunnel 10

Figure 2.2 (a) Filter box

(b) Frame of filter box 11

Figure 2.3 Fan, motor, inlet vane control and variable speed drive 12

Figure 2.4 The diffuser and its design schematic 13

Figure 2.5 The heat exchanger 15

Figure 2.6 Hot water heater, strainer and circulations pump 16

Figure 2.7 Schematic of the heating/cooling piping network 17

Figure 2.8 The Screen pack and its design schematic 18

Figure 2.9 Contraction nozzle 23

Figure 2.10 Suction box and blow 24

Figure 2.11 (a) Transition section for reverse flow combustor study

(b) Schematic of test section for reverse flow combustor study 25

Figure 2.12 Gas turbine reverse-flow combustor test ring simulating a $1/7^{th}$ sector of dump diffuser-combustor combination. There are two interchangeable test sections: one for flow measurements and the other one for heat transfer study 26

Figure 2.13 Gas turbine reversed-flow combustor heat transfer test rig simulating a $1/7^{th}$ sector of dump diffuser-combustor combination 27

Figure 2.14 Single combustion chamber model 28

Figure 2.15 Plastic sheath model 29

Figure 2.16 Overview of combustion chamber with pressure taps 30

Figure 2.17 Middle chamber with pressure taps 30

Figure 2.18 Middle chamber with radial pressure taps 31

Figure 2.19 Bottom chamber with pressure taps 31

Figure 2.20 Top chamber with pressure taps 32

Figure 2.21 Closed combustion chamber with heat gun accommodated inside 33

Figure 2.22 Transitional pieces instrumented with 80 thermocouples in (a) and(c), painted black spray-on rubber in (b) and (d) 34

Figure 2.23 Thermocouples on combustion chamber 35

Figure 2.24 Thermocouples on split combustion chamber 35
Figure 2.25 (a) Automatic traversing stage
(b) Automatic traversing stage motion controller and driver..... 37
Figure 2.26 Scanivalve pressure measurement system 39
Figure 2.27 Scanivalve pressure system connections and control 41
Figure 2.28 Scanivalve module and measurement mechanism..... 41
Figure 2.29 Overview of the Scanivalve pressure data acquisition system 42
Figure 2.30 In-house designed application's interface to control the pressure scanner system 43
Figure 2.31 Keithley model 2700-multimeter/data acquisition systems..... 44
Figure 2.32 Overview of temperature measurement system..... 44
Figure 2.33 Components used in the thermocouple measurement
(a),(b) and (c) are internal views of isothermal box setting up steps
(d),(e) and (f) are copper wires and RS232 connectors used to connect isothermal box and data acquisition board
(g),(h) and (i) are data acquisition board and its connectors
(j) and (k) are different views of heat gun accommodated in the combustion chamber
(l) is the thermal bottle contains the ice bath 45
Figure 2.34 Hot-wire anemometry and 3-D automatic traversing measuring system..... 47
Figure 2.35 Overview of the IFA 300 hot-wire data acquisition system 47
Figure 2.36 Velocity distributions (m/s) at the exit of the contraction 48
Figure 2.37 Velocity distributions (m/s) in the core region by removing the boundary layers at the exit of the contraction..... 49
Figure 2.38 Pitot-static tube 52
Figure 2.39 Dwyer Model 1430 Microtector 53
Figure 3.1 Calibration curves (pressure vs. voltage) of six pressure transducers 66
Figure 3.2 The averaged calibration line for all 6 transducer 67
Figure 3.3 Comparison of pressure distribution on the combustor and transition walls between sheathed and no-sheath cases 69
Figure 3.4 A block diagram illustrates the backward tracing procedure for identifying the primary measurands. The variables located outside the dashed box are primary measurands..... 72

Figure 3.5 Temperature comparisons between no-sheath and sheathed cases 75
Figure 4.1 (a) Computational configuration of sheathed case based on experimental test conditions with one full combustor and two adjacent half combustors in a periodic $1/7^{th}$ sector of the complete system
(b) Computational configuration of sheathed case for real gas turbine operating condition with one full combustor in a periodic $1/14^{th}$ sector of the complete system 77
Figure 4.2 Meshes of different parts of the reverse-flow combustor 79
Figure 4.3 (a) First method: the impinging holes are set us interior surfaces with zero thickness
(b) Second method: the impinging holes set as part of interior volume 80
Figure 5.1 The 3-D model of no-sheath Case simulating one full chamber and two adjacent half chambers (Case 1) 91
Figure 5.2 Pressure contour on mid-chamber and transitional piece walls (Case 1) 92
Figure 5.3 Representative pathlines (Case 1) 92
Figure 5.4 Velocity vector plots on different X-direction planes colored by pressure distribution (Case 1) 93
Figure 5.5 Velocity vector plots on different Y-direction planes with colored pressure distribution (Case 1) 93
Figure 5.6 Velocity vector plots on different Z-direction planes with colored pressure distribution (Case 1) 94
Figure 5.7 Velocity profile colored by static pressure contours at different locations (Case 1)
(a) X=0.6 plane velocity profile and static pressure contours 94
(b) Z=0 plane velocity profile and static pressure contours 94
(c) Radial plane halfway between two combustors 95
Figure 5.8 Comparison of static pressure between experimental and CFD data (Case1) .. 96
Figure 5.9 3-D model of sheathed Case simulating one full chamber and two adjacent half chambers (Case 4) 97
Figure 5.10 Sheath outside the transitional piece walls 98
Figure 5.11 Pressure contour on mid-chamber and transitional piece walls (Case 4) 98
Figure 5.12 Representative pathlines from inlet to exit of sheathed case (Case 4) 99
Figure 5.13 Velocity vector plots on different X-direction planes colored by pressure distribution (Case 4) 100

Figure 5.14 Velocity vector plots on different Y-direction planes with colored pressure distribution (Case 4) 100
Figure 5.15 Velocity vector plots on different Z-direction planes with colored pressure distribution (Case 4) 101
Figure 5.16 Velocity profile imposed by colored pressure distribution at different locations (Case 4)
(a) X=0.6 plane velocity profile and static pressure contours 101
(b) Z=0 plane velocity profile and static pressure contours 101
(c) Radial plane halfway between two combustors 102
Figure 5.17 Comparison between the experimental and CFD static pressure data (Case 4) 103
Figure 5.18 Comparison of CFD simulated static pressure contour between Case 1 (unheated, no-sheath) and Case 4 (unheated, sheathed) 104
Figure 5.19 (a) Temperature distributions on mid-chamber and transitional piece walls
(b) Temperature distributions in the dump diffuser around the combustor (Case 2) 105
Figure 5.20 (a) Temperature distributions on mid-chamber and transitional piece walls
(b) Temperature distributions in the dump diffuser around the combustor (Case 5) 106
Figure 5.21 Comparison of temperature distributions on mid-chamber between Case 2 (no-sheath, heated) and Case 5 (sheathed, heated) 107
Figure 5.22 (a) Temperature measurement locations' reference 108
(b) Temperature comparisons between Case 2 (no-sheath, heated) and Case 5 (sheathed, heated) 109
Figure 5.23 3-D model for elevated real gas turbine operating condition with a 1/14th computational domain without sheath by employing the periodic wall condition (Case 3) 110
Figure 5.24 Pressure contour on chamber and transitional piece walls for elevated conditions of Case 3 (elevated gas turbine condition, no-sheath) 111
Figure 5.25 Representative pathlines (Case 3) 111
Figure 5.26 Different views of velocity vector on X- planes colored by pressure (Case 3) 112
Figure 5.27 X=0 plane velocity profile with colored pressure contour (Case 3) 112

Figure 5.28 Z=0 plane velocity profile with colored pressure contour (Case 3)..... 112
Figure 5.29 (a) Temperature distributions on mid-chamber and transitional piece walls (b) Temperature distributions in the dump diffuser around the combustor for Case 3 (elevated gas turbine condition, no-sheath)..... 113
Figure 5.30 3-D model for elevated real gas turbine operating conditions with a 1/14th computational domain with sheath by employing periodic wall condition (Case 6)..... 114
Figure 5.31 Static pressure contour (Case 6) 115
Figure 5.32 Representative pathlines (Case 6)..... 115
Figure 5.33 Velocity vectors on different X-direction planes colored by static pressure (Case 6) 116
Figure 5.34 X=0 plane velocity profile with colored pressure contour (Case 6) 116
Figure 5.35 Z=0 plane velocity profile with colored pressure contour (Case 6)..... 116
Figure 5.36 (a) Temperature distributions on mid-chamber and transitional piece walls (b) Temperature distributions in the dump diffuser around the combustor for Case 6 (elevated gas turbine condition, sheathed) 117
Figure 5.37 Comparison of pressure distribution between Case 3 (elevated, no-sheath,) and Case 6 (elevated, sheathed)..... 118
Figure 5.38 Comparison of temperature distribution between Case 3 (elevated, no-sheath,) and Case 6 (elevated, sheathed)..... 119
Figure A-1 Schematic diagram of air flow moves perpendicular to a cylinder to simulate the cross flow passing through the combustion chamber and the transition piece..... 126
Figure A-2 Schematic diagram of air flow moves in parallel with the combustion chamber and the transitional piece..... 127
Figure B-1 Schematic diagram of air flow moves perpendicular to a cylinder to simulate the cross flow passing through the combustion chamber and the transition piece..... 129
Figure B-2 Schematic diagram of air flow moves in parallel with the combustion chamber and the transitional piece..... 131
Figure B-3 Overall heat transfer through the wall and resistance analogy 132
Figure D-1 E-type thermocouple (Millivolts) V.S. temperature (°C) curve..... 143

LIST OF TABLES

Table 1.1 Pressure drop effects (MS7001EA) 5
Table 2.1 Specifications of wire screen 17
Table 2.2 X-Y coordinates of top and bottom surface curvature of contraction..... 21
Table 2.3 X-Y coordinates of side surface curvature of contraction 22
Table 2.4 Static port location on combustor model 32
Table 2.5 Thermocouples' location record 36
Table 2.6 Thermocouple location on combustion chamber and transitional piece walls 36
Table 3.1 A representative initial and final conditions of room and transducers' offset voltages during one experiment..... 63
Table 3.2 Representative values of density and gravity used during the analysis 63
Table 3.3 Inlet airstream velocity in transition section upstream of test section at different running speeds..... 64
Table 3.4 Readings of water column heights, voltages of 6 transducers and differential pressures at various wind speeds 65
Table 3.5 Room conditions before and after Combustor pressure measurements for the sheathed case..... 65
Table 3.6 Equipments' specification list for pressure measurement..... 72
Table 3.7 Input data and results for zeroth, pretest and first uncertainty analysis..... 73
Table 3.8 A representative room conditions before and after temperature measurement.... 74
Table 4.1 Parameters and operating conditions for simulated cases..... 89
Table C-1 Displayed pressure transducer voltage values (raw data) and corrected voltage values at 60Hz for the no-sheath case 135
Table C-2 Displayed pressure transducer voltage values (raw data) and corrected voltage values at 60Hz for the sheathed case..... 136
Table C-3 Combustion chamber static gauge pressure at 60Hz for no-sheath case 137
Table C-4 Combustion chamber static gauge pressure at 60Hz for sheathed case..... 138

Table C-5 Comparison of measured experimental pressure with the CFD results (no-sheath, unheated)..... 139

Table C-6 Comparison of measured experimental pressure with the CFD results (sheathed, unheated) 140
Table D-1 Experimental thermocouple data (μ V) for no-sheath case..... 142
Table D-2 Experimental thermocouple data (μ V) for sheathed case 143
Table D-3 Temperature measurement (K) for no-sheath case 144
Table D-4 Temperature measurement (K) for sheathed case..... 144
Table D-5 Experimental temperature comparison between the no-sheath case and sheathed case..... 145
Table D-6 CFD temperature comparisons between Case 2(no-sheath, heated) and Case 5 (sheathed, heated) 146

NOMENCLATURE

a	local speed of sound (m/s)
c_p, c_v	Specific heat at constant pressure, volume (J/kg-K, Btu/lbm-°F)
Dij	Mass diffusion coefficient (m^2/s, ft^2/s)
E	Total energy, activation energy (J, Btu)
g	Gravitational acceleration (m/s^2 , ft/s^2)
H	Total enthalpy (energy/mass, energy/mole)
h	Heat transfer coefficient (W/m^2-K, Btu/ft^2-hr-°F)
h	Species enthalpy (energy/mass, energy/mole)
h_0	Standard state enthalpy of formation (energy/mass, energy/mole)
J	Mass flux; diffusion flux (kg/m^2-s, lbm/ft^2-s)
K	Equilibrium constant = forward rate constant/backward rate constant (units vary)
k	Kinetic energy per unit mass (J/kg, Btu/lbm)
k	Reaction rate constant, e.g., k1, k-1, $k_{f;r}$, $k_{b;r}$ (units vary)
k	Thermal conductivity (W/m-K, Btu/ft-hr-°F)
k_B	Boltzmann constant ($1.38x10^{-23}$ J/mole-K, $7.27x10^{-27}$ Btu/mole-°R)
k,kc	Mass transfer coefficient (units vary)
m	Mass (kg, lbm)
M	Mach number
M_w	Molecular weight (kg/kgmol)
Nu	Nusselt number = hL/k (dimensionless)
P	Pressure (Pa, atm, mm Hg, lbf/ft^2)
Pr	Prandtl number = α/ν (dimensionless)
q"	Heat flux (W/m^2 , Btu/ft^2-hr)
R	Gas-law constant ($8.31447x10^3$ J/kgmol-K, 1.98588 Btu/lbmol-°F)
Re	Reynolds number ≡ UL/ν (dimensionless)
S	Total entropy (J/K, J/kgmol-K, Btu/lbmol-°F)
s	Specific entropy
s_0	standard state entropy (J/kgmol-K, Btu/lbmol-°F)
Sc	Schmidt number = ν/D (dimensionless)
S_{ij}	Mean rate-of-strain tensor (s^{-1})
T	Temperature (K, °C, °R, °F)
t	Time (s)
t	thickness (m, ft)
U	Free-stream velocity (m/s, ft/s)
u; v; w	Velocity components (m/s, ft/s);
V	Volume (m^3, ft^3)

Greek Letter

α	Permeability, or flux per unit pressure difference (L/m^2-hr-atm, ft^3/ft^2-hr-(lbf/ft^2))
α	Thermal diffusivity (m^2/s, ft^2/s)
β	Coefficient of thermal expansion (K-1)
γ	Specific heat ratio, c_p/c_v (dimensionless)
Δ	Change in variable, final – initial (e.g., .p, .t, .H, .S, .T)
ε	Emissivity (dimensionless)
ε	Turbulent dissipation rate (m^2/s^3, ft^2/s^3)
ν	Dynamic viscosity (Pa-s, lbm/ft-s)
μ	Kinematic viscosity (m^2/s, ft^2/s)
ρ	Density (kg/m^3, lbm/ft^3)
σ	Stefan-Boltzmann constant (5.67×10^{-8} W/m^2-K^4, 1.71×10^{-9} Btu/hr-ft^2-°R^4)
σ_s	Scattering coefficient (m^{-1})
$\overline{\overline{\tau}}$	Stress tensor (Pa, lbf/ft^2)
τ	Shear stress (Pa, lbf/ft^2)
τ	Time scale, e.g., τ_c, τ_p (s)

ABSTRACT

Reverse-flow combustors have been used in heavy land-based gas turbines for many decades. A sheath is typically installed to provide cooling at an expense of large pressure losses, through small jet impingement cooling and strong forced convention channel flow. With the modern advancement in metallurgy and thermal-barrier coating technologies, it may become possible to remove this sheath to recover the pressure losses without melting the combustor chamber.

However, without the sheath, the flow inside the dump diffuser may exert nonuniform cooling on the combustion chamber. Therefore, the objective of this project is to investigate the flow pattern, pressure drop, and heat transfer in the dump-diffuser reverse-flow combustor with and without sheath to determine if the sheath could be removed. The investigation was conducted through both experimental and computational simulation. The results show that 3.3% pressure losses could be recovered and the highest wall temperature will increase 18% without the sheath.

Keywords: reverse-flow, combustor, impingement sheath, pressure drop, dump-diffuser, melting, nonuniform, thermal-barrier

CHAPTER ONE

INTRODUCTION

1.1 Background

Several world's leading suppliers of power generation, including General Electric, Siemens, Hitachi and Mitsubishi, have been using a reverse-flow type multiple-combustion system as part of their heavy-duty gas turbine system.

Gas turbines were first used for power generation in the 1950s and were used almost exclusively for peak duty. For this mode of service, designs were required that featured low specific cost and good starting reliability. Through the 1960s and 1970s advances in gas-turbine efficiency, reliability, and availability facilitated a wider range of applications for gas turbines. As operating hours increased, fuel cost assumed greater significance in optimizing machine design. The importance of this factor grew dramatically with the rapid rise in fuel prices following the oil crises.

As operating fuel costs became more important in gas-turbine economics, technology development was focused on improving efficiency, primarily through increasing firing temperature. The MS7001 design was originated by General Electric (GE) in 1966. At that time, there was an enormous demand in the U.S. for gas turbines with the capability for peak load power generation. The primary objective of the MS7001 program was to develop a larger gas turbine for power generation applications. The result of the MS7001 development program was a new gas turbine model that included a 17-stage compressor and a three-stage turbine that operated at 3600 rpm. In 1981, the MS7001F program began, and planners realized that the

larger gas turbine size would mean lower power plant specific cost, and a higher firing temperature would result in higher combined cycle efficiency. To achieve the higher firing temperatures many changes would be required to ensure no adverse affects on maintenance intervals. Key technology had been developed that would allow for this new design. These included new compressor airfoil designs that allowed for a higher inlet mass flow as well as new methods for large superalloy casting, which would allow for more efficient cooling of the buckets and nozzles. In the 1990s, advances in materials, cooling technology and design techniques had allowed GE MS7001 turbines to be operated with higher firing temperatures and airflows while achieving higher turbine output and efficiency. Improvements in combustion technology have also made significantly lower emission levels a reality. After 2000, however, designing gas turbines requires balancing all three major elements of life-cycle cost: capital cost, operating and maintenance (O&M cost and fuel cost. Determining the optimum design solution – that is, determining which advancements to incorporate – is a very complex exercise in designing for multiple objectives. One of the essential components that needs to be improved is the reverse-flow combustors. In the future, these combustors will handle low-Btu synthetic gas derived from coal/biomass or hydrogen-rich fuel.

1.2 Introduction of reverse-flow combustor

The essential feature of the combustor is to stabilize the flame in a high-velocity stream, where sustained combustion is difficult. The combustion process must be stable over a wide range of fuel flows required for ignition, start-up, and full power. It must perform within desirable ranges of emissions, exit temperature, and fuel properties and minimize the parasitic pressure drop between the compressor and turbine. The combustion hardware must be

mechanically simple, rugged, and small enough to be properly cooled by the available air. This hardware must have acceptable life and be accessible, maintainable, and repairable. The reverse-flow, multiple-combustion system is short, compact, lightweight and mounted within the flange-to-flange machine on the same turbine base as shown in Fig. 1.for the MS7001EA combustion chamber arrangement.

The MS7001FA combustion system arrangement consists of 14 combustion chambers. The liners are constructed of Hastelloy-X material. The size of the combustion liners provides the space required to completely burn residual fuel. Lighter fuels are also easily burned in these liners. Smaller-diameter combustors allow penetration of air jets into the combustor at acceptable pressure drops. Jet penetration is necessary to mix the air with the fuel quickly and obtain complete combustion without forming soot in fuel-rich pockets. The highly stir-red flame produced by these jets also reduces radiation to the liner walls with beneficial effect on liner life.

The combustion liner is carefully cooled to tolerate high-temperature gases located a few millimeters from the combustor liner wall. As firing temperatures increase, more air is needed to combine with the fuel for adequate combustion, and less air is available for liner wall cooling. This has been offset by a more efficient cooling system and by reducing the surface area (length) of the liner. Louver cooling, which has been highly successful and reliable over the years, has been replaced by slot cooling in the turbines with the highest firing temperatures. The slot cooling method reduces liner metal temperatures by 139C (250F) from an equivalent louver system.

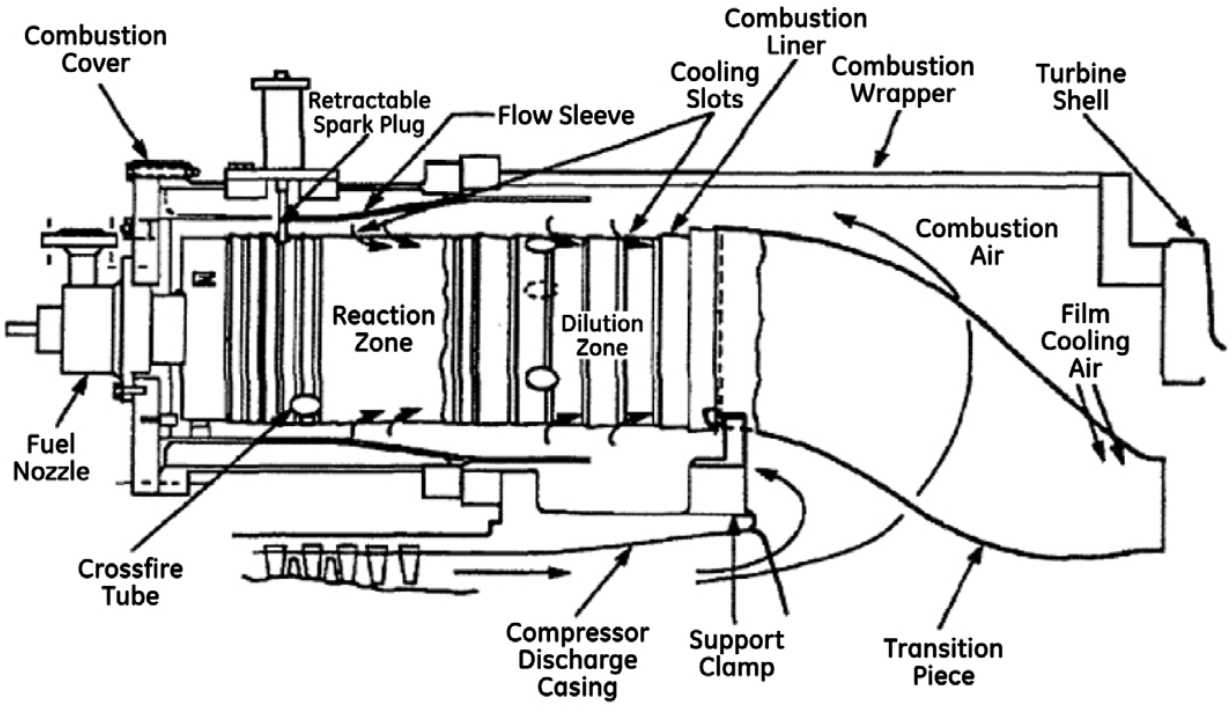

Figure 1.1 MS7001EA combustion chamber arrangement

The length of the combustor provides time to complete the combustion reaction for the variety of fuels burned in the turbine and then dilute the combustion products with excess air to form a temperature profile acceptable to the downstream turbine components. The temperature profile of hot gases entering the turbine sections is carefully developed to provide maximum life for the nozzles and buckets. The average radial profile from the combustors will produce lower temperatures near the bucket root where the centrifugal stress is maximum, and at the outer sidewall where nozzle bending stresses are also at a maximum.

The transition piece, which channels the high-temperature gas from the combustion liner to the first-stage turbine nozzle, is small enough to be cooled by air flowing reversely from the compressor. This provides effective cooling of the transition piece for firing temperatures up to

1010C (1850F). The outer portion of the transition piece near the first-stage nozzle is less effectively cooled, and at firing temperatures above 1010C (1850F), jet-film cooling is added.

The inner transition piece is surrounded by a perforated sleeve with the same general shape as the transition piece. This perforated sleeve forms an impingement cooling shell causing jets of compressor discharge air to be directed onto the transition piece body. The air, after impinging on the transition piece body, then flows forward (actually reversely towards the compressor) in the space between the impingement sleeve and transition piece into the annulus between the flow sleeve and the combustion liner. It then joins additional air flowing through bypass holes in the flow sleeve providing the air for the combustion/ cooling/ dilution processes. The impingement sleeve is fabricated of- AISI-304 stainless steel, the transition piece body of Nimonic 263, and the aft frame of cast FSX414. The internal surface of the transition piece has a thermal barrier coating to minimize metal temperatures and thermal gradients.

Higher firing temperatures require combustors that release more energy in a given volume. High volumetric heat release rates, which depend on higher turbulent mixing in the combustor primary zone, are achieved by raising the combustor pressure drop. Inserting air filtration, silencing, evaporative coolers or chillers into the inlet or heat recovery devices in the exhaust also causes pressure losses in the system. The effects of these pressure losses are unique to each design. Table 1 shows the effects on the MS7001EA, which are typical for the E technology family of scaled machines (MS6001B, 7001EA, 9001E).

Table 1: Pressure drop effects (MS7001EA)

4 Inches (10 mbar) H_2O Inlet Drop Produces:	4 Inches (10 mbar) H_2O Exhaust Drop Produces:
1.42% Power Output Loss	0.42% Power Output Loss
0.45% Heat Rate Increase	0.42% Heat Rate Increase
1.9 F (1.1 C) Exhaust Temperature Increase	1.9 F (1.1 C) Exhaust Temperature Increase

1.3 Advantages and Disadvantages of Reverse-flow combustor

The advantages of using a reverse-flow combustor are:

I. Reverse-flow combustor can reduce the length of the gas turbine and make the transportation much easier.

II. Reduced length will allow single shaft sitting on two bearings. This will reduce the vibration and maintenance problems.

III. The reverse-flow layout effectively uses the air flow to cool down the combustor liner and the transition piece as a counterflow heat exchanging process. The absorbed heat by the air is returned back to the system. In other words, the reverse-flow combustor cooling process is actually a preheating process for the air entering the combustor.

IV. The reverse-flow process also allows warmer air to serve as the dilution air to control the NOx formation instead of using other energy to preheat the dilution air or use cold air , which could quench the flame and produce CO.

V. Similarly, the preheat air also serves as wall jet film cooling on inside of the combustor liner. Penetration of air jet into the combustion chamber can enhance air-fuel mixing to achieve more effective combustion and help reduce NOx formation near the wall.

The disadvantages include increased material and manufacturing cost and pressure losses.

1.3 Motivation and Objective

Using the impingement sheath and flow sleeve to cool combustor and transition piece walls causes a large pressure drop. With modern advancements in metallurgical and thermal-barrier coating technology, it may become possible to remove the combustor's outer sheath to recover the pressure drop without melting the combustor chamber and the transition piece walls.

Without the sheath, however, the flow inside the dump diffuser may exert very nonuniform cooling on the combustor and transition piece. Therefore, the **objective** of this project is to investigate the flow pattern, pressure drop, and heat transfer in the dump diffuser and reverse-flow combustor with and without the combustor outer sheath.

1.5 Approach

This project will perform the following:

- Conduct both experimental and CFD simulation
- Use experimental data to validate CFD model, which can further simulate the real aerodynamic and thermodynamic behavior at elevated gas turbine pressure and temperature condition

CHAPTER TWO

TEST FACILITY AND INSTRUMENT

2.1 Test Facility

2.1.1 Wind Tunnel System

The wind tunnel and the accompanied data acquisition systems have been successfully constructed and established in the ECCC's (Energy Conversion and Conservation Center) laboratory. The detailed technical description of the wind tunnel components, the data acquisition systems, and the wind tunnel qualification data are provided. The wind tunnel is an open-circuit design, rated to provide 12,000 CFM airflow with a top wind speed of 41.5 m/s (333 ft/s or 91 mph). The speed of the wind tunnel is controlled by a constant-torque, variable frequency motor controller. The temperature of the wind tunnel flow can be cooled at a rate of 4.5^{o}C/min (8^{o}F/min) down to 10^{o}C (50^{o}F) and be heated at a rate of 0.77^{o}C/min (1.4^{o}F/min) up to 60^{o}C (140^{o}F). Four data acquisition systems are used, including an automatic traversing system, a four-channel hot wire anemometry, a 96-channel thermocouple acquisition system, and a 288-channel pressure scanning system.

Design and construction of the wind tunnel and auxiliary accessories have been successfully completed. The function of each subsystem has been tested, including heating/cooling system, boundary layer control system, probe traversing system, the pressure scanning and acquisition system, the hot wire system, and the thermocouple measurement system.

The test section was designed for studying the thermal/flow behaviors of the reverse-flow combustor which simulates the combustor system of GE's MS7001FA heave-duty gas turbine system.

The constructed wind tunnel is an open-circuit system (Fig. 2.1). The maximum velocity that can be reached in the test section is about 30 m/s (95 ft/sec or 65 mph). To filter out particles larger than 5 μm and to protect the hot-wire sensors to be used in the test section, a filter made of polyester felt is installed at the inlet of the fan. A fan with a capacity of 12,000 CFM, a rating of 30 bhp, and a static pressure of 10 inches water column is used. To control the fan speed, a variable frequency, constant-torque motor controller has been installed. A combination of motor controller and fan inlet vane can be used to reduce the flow speed down to 3 ft/sec without oscillation or instability. The flow passes through a diffuser from the fan to the flow straightener section, which includes a heat exchanger for controlling flow temperature, a screen pack, and a settling chamber. The densely packed fins of the heat exchanger serve as the first-stage flow straightener to break up large eddies (swirls) from the blower. A conventional honeycomb section is therefore not needed. The screen pack serves as the second stage flow straightener to break up the small eddies and make the flow more uniform. A contraction and two test sections are designed and constructed. Each wind tunnel component is described in the following sections.

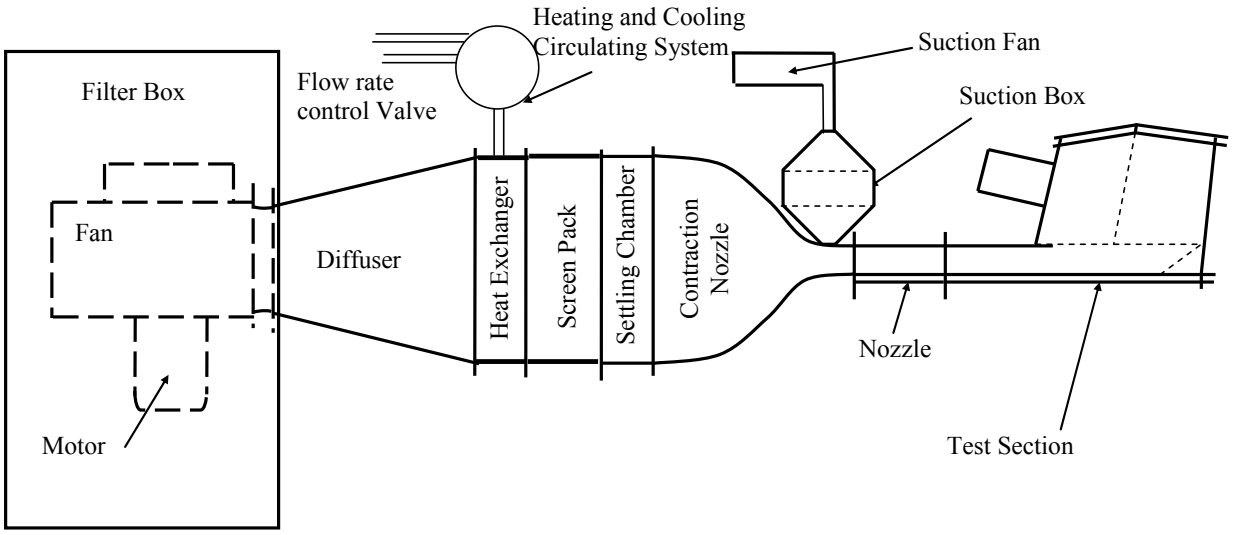

Figure 2.1 Plan view of the wind tunnel

2.1.2 Filter Box

To avoid the possibility of dust particles breaking the 3μm hot-wire sensors or the likelihood of drift in the sensor response due to contamination on the hot-wire sensors, a filter box is constructed and connected to the inlet of the blower. A layer of polyester felt, manufactured by Buffalo Felt Products Corp., is used to filter out any particles larger than 5μm. To reduce the large pressure drop across the thick felt, the filter box is specially designed to extend the felt surface area to the limit of the space available. Increasing the surface area reduces the flow speed and consequently reduces the pressure drop across the felt.

The surface area of this box is 44.13 m^2 (475 ft^2) and the flow speed at the maximum flow rate (120,000 CFM) is 0.15 m/s. The corresponding maximum pressure drop is approximately 5.08 mm (0.2 inch) H_2O. The box frame is constructed of 2″ x 2″ wooden bars and covered with nominal 2-inch chicken wire to support the deforming force from the felt under suction force. A thin sheet of muslin cloth cover is placed over the felt to filter out the large-size dust particles.

The filter box is shown in Fig. 2.2(a) and the frame on which the polyester felt is wrapped is shown in Fig. 2.2(b)

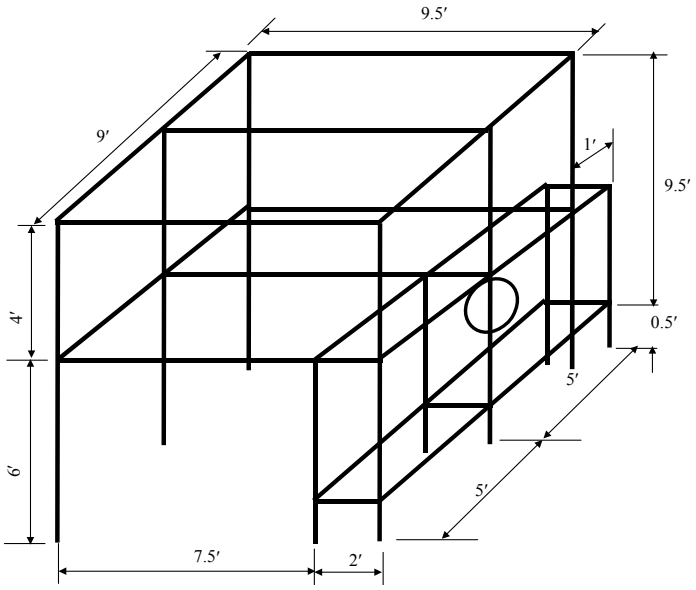

(a) (b)

Figure 2.2 (a) Filter box, (b) Frame of filter box

2.1.3 Blower, Motor and Variable Speed Drive

The blower is an airfoil bladed fan by Cincinnati Fan; model SQAF, size 270, class II/III Wheel, arrangement 4, CW Rotation, SQ Wheel, and TH Discharge. A 3-phase, 30-hp motor directly drives the fan. At full load, the fan's speed is 1756 rpm. The operating point of the blower is at 12,000 CFM and 10 inches water column (static pressure). The blower in equipped with an inlet vane control, which offers a stable flow control at low speeds.

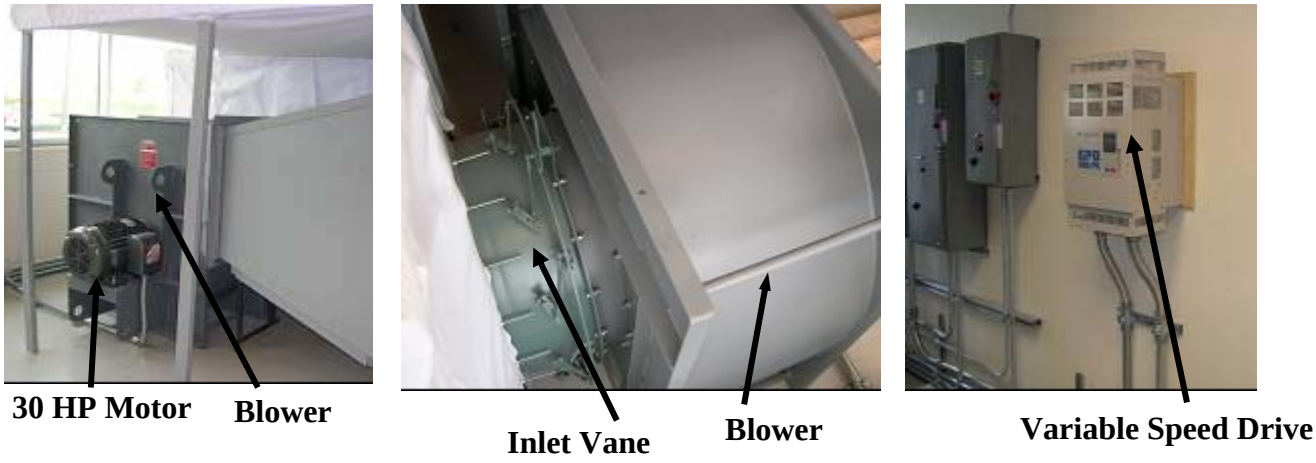

Figure 2.3 Fan, motor, inlet vane control and variable speed drive

A variable frequency, constant-torque motor controller (YASKAWA model GPD 506/P5) shown in Fig. 2.3 is used to control the blower speed. It is a high performance AC motor drive modulated by sine-coded pulse width that generates an adjustable voltage/frequency three-phase output for complete speed control of the induction motor. The motor controller is equipped with automatic stall prevention with a voltage boost to prevent nuisance tripping during load or line side transient conditions.

2.1.4 Diffuser

To reduce pressure loss in the flow straightener, a diffuser is installed to reduce flow speed before entering the flow straightener. The diffuser is designed and constructed in house. The diffuser is 48 inches long with an inlet cross-section of 26¼ inches x 23½ inches and an outlet cross-section of 48 inches x 48 inches. The diffuser is connected between the fan exit and the heat exchanger. Due to the constraint of the available space, the diffuser is designed with a large included angle that may cause flow separation at the diffuser exit. Considering the

blockage effect of the densely packed heat exchangers fins downstream, the separation is estimated to be relatively stable and will only cause additional pressure drop without affecting the uniformity of the flow after passing through the flow straightener. The detailed dimension of the diffuser is shown in Fig. 2.4.

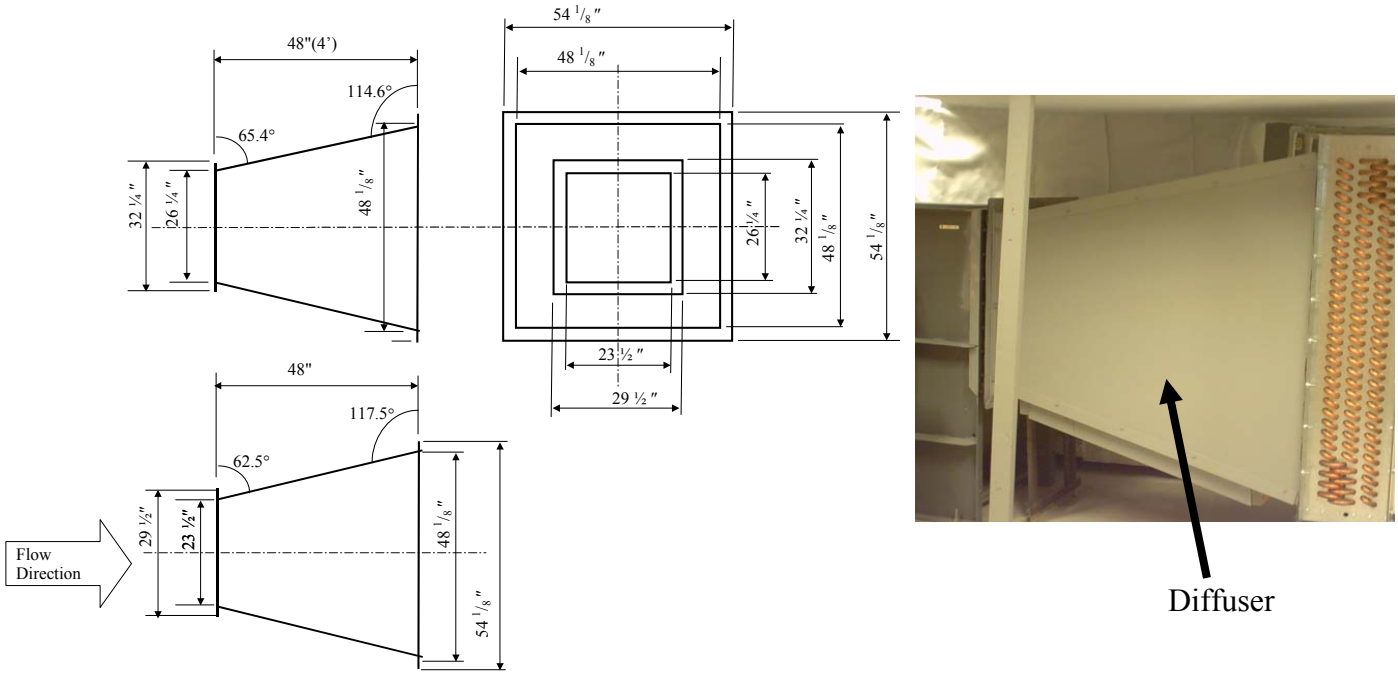

Figure 2.4 The diffuser and its design schematic

2.1.5 Heat Exchanger and Heating/Cooling System

The heat exchanger serves as a part of the flow straightener as well as the core for the temperature control system. The heat exchanger is connected at exit of the diffuser as shown in Fig. 2.5. As mentioned earlier, the densely packed fins, with an equivalent length-over-spacing-ratio (L /D) of 75, serve as the first-stage flow straightener that can effectively break down large swirl eddies generated by the upstream blower. A conventional honeycomb section is therefore not needed. The main function of the heat exchanger is to make the free-stream temperature uniform and provide a means to control the temperature in the test sections. The design of the

heat exchanger is based on the cooling load. The cooling rate is approximately 4.5°C/min (8°F/min). The lowest temperature can be reached is approximately 50°F, which is 8°F above the chilled water temperature. The cooling specifications of the heat exchanger (Fig.2.5) are:

A. Air side

Air volume flow rate	1,200 CFM
Required Capacity	94,000 BTU/Hr
Entry DB/WB temperature	80.0°F/68.2°F
Required DB/WB temperature	61.1°F/60.0°F (cooling)
Air side Pressure	14.812 Psia

B. Tube side

Fluid	Water
Fluid flow rate	25.0 GPM
Enter fluid temperature	42.0 °F

C. Coil Selection

Model Number	48 x 48-6R-58/144
Die Surface	5/8 – 1 ½ x 1.299 staggered (Flat-#1)
Face area	4 ft x 4 ft
Air velocity	750 ft/min
Number of circuits	8
Tube velocity	3.4 ft/sec
Configuration	Thermal Counterflow
Tube material	Copper
Tube wall thickness	0.020 inches

Fin material	Aluminum
Fin Thickness	0.0075 inches
Header Diameter	1.375 inches

D. Capacity

Total Capacity	331,085 BTU/Hr
Sensible heat capacity	24,500 BTU/Hr
Leaving DB/WB temperature	61.1°F/59.8°F
Leaving Fluid temperature	68.5°F
Fluid pressure drop	0.3 ft. H_2O
Air Friction	0.79 in. H_2O

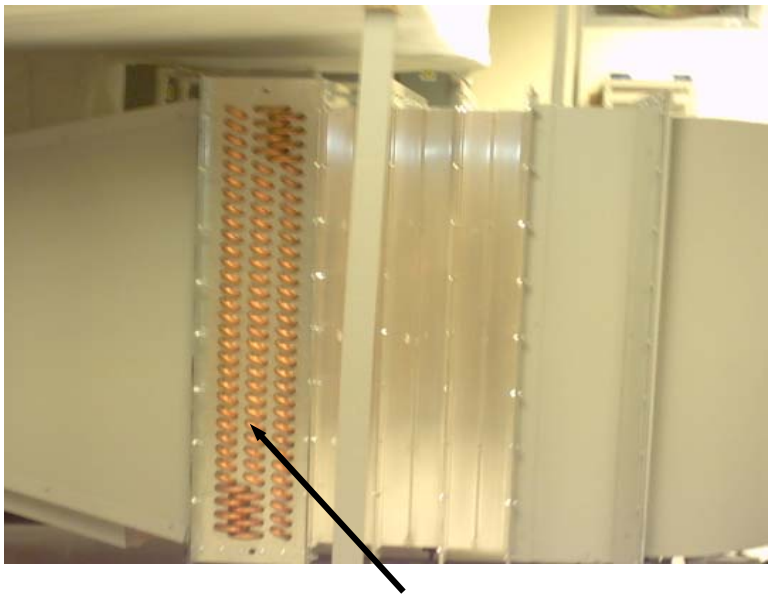

Figure 2.5 The heat exchanger

An 80-gallon residential electric water heater (Fig. 2.6) containing 4500 watt/240 volts copper elements, is used to supply hot water when hot air is needed in the test section. Since the wind tunnel is an open-circuit design, the air is exhausted into the laboratory. The entire laboratory (15ft x 30 ft x10ft) serves as the flow returning chamber as well as a weather-control room. The temperature can be raised at a rate of 0.77^{o}C/min (1.4^{o}F/min) up to 60^{o}C (140^{o}F) when the AC is turned off in the room. When cooling is needed in the test section, the heater would also be used as a chilled water buffer tank, when cooling is needed in the test section. The chilled water is provided by the building. The chilled or hot water is re-circulated into the heat exchanger by a 1.5 hp circulations pump shown in Fig. 2.6. A strainer is affixed to the circulating line to filter out any debris from the water. A schematic of the piping network for the heater and heat exchanger is shown in Fig. 2.7.

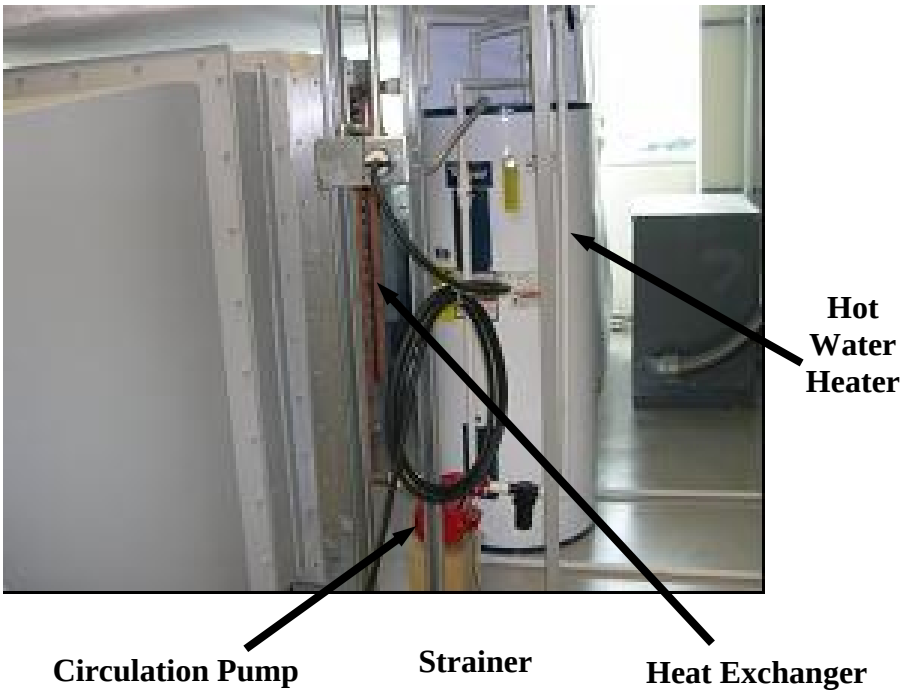

Figure 2.6 Hot water heater, strainer and circulations pump

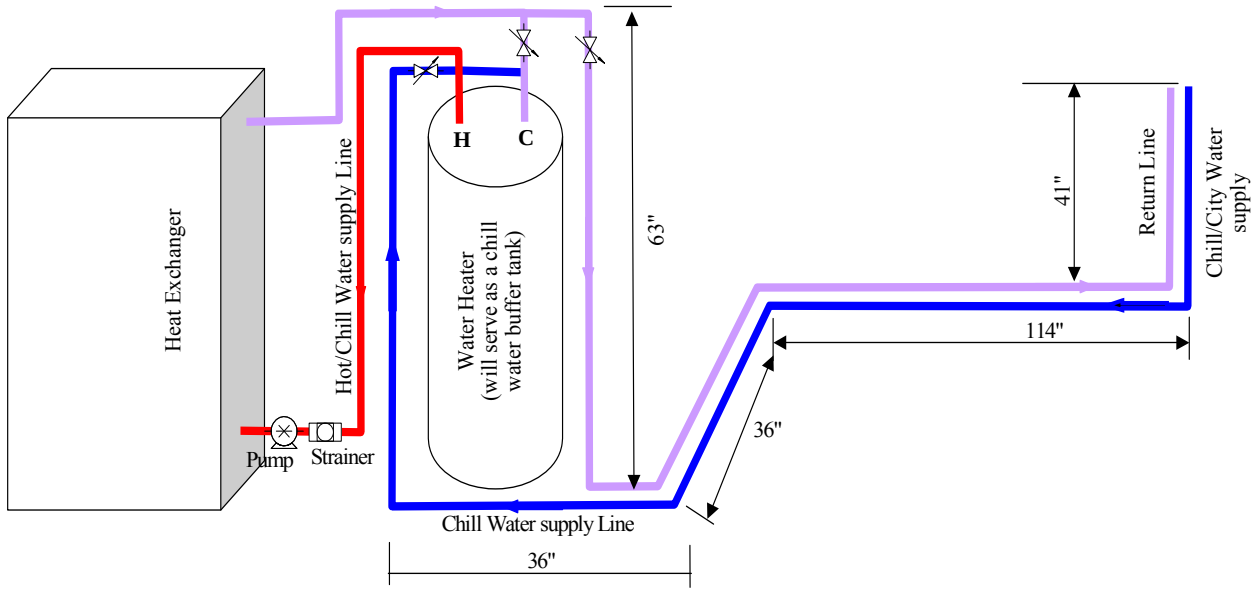

Figure 2.7 Schematic of the heating/cooling piping network

2.1.6 Screen Pack

The screen pack consists of five screen frames of three different mesh sizes. The screens are made of stainless steel wires and fastened with extruded aluminum frames. The screen pack is installed between the heat exchanger and the settling chamber as shown in Fig. 2.7. Their specifications are given in Table 2.1. The five screen frames are arranged in the order of 18, 24, 24, 30, 30 meshes from upstream to downstream.

Table 2.1: Specifications of Wire Screen

Mesh Count (per inch)	Wire Diameter (inch)	Mesh Opening (inch)	Open Area Ratio (percent)
18	0.0090	0.0466	70.2
24	0.0075	0.0342	67.2
30	0.0065	0.0268	64.8

Extruded aluminum bars, 5 cm wide and 0.32 cm thick, were welded to form a rectangular frame with an inside dimension of 4 ft x 4 ft. Each screen is then riveted between two frames. The 7.62 cm wide U channel, formed by bending 0.16 mm (1/16 inch) thick aluminum plate, is spaced between each two screens. The spacing between any two screens is 7.78 mm, which is about 360-500-screen wire diameter long. This spacing allows enough distance for the wire-generated wakes to decay. The first screen is 0.5 cm downstream of the heat exchanger, and the last screen is 7.5 cm away from the entrance of the settling chamber. This last spacer is fixed permanently with the settling chamber. Its junction is filled with body-filler and is sanded smooth. A detailed drawing of the screen pack is also shown in Fig. 2.8.

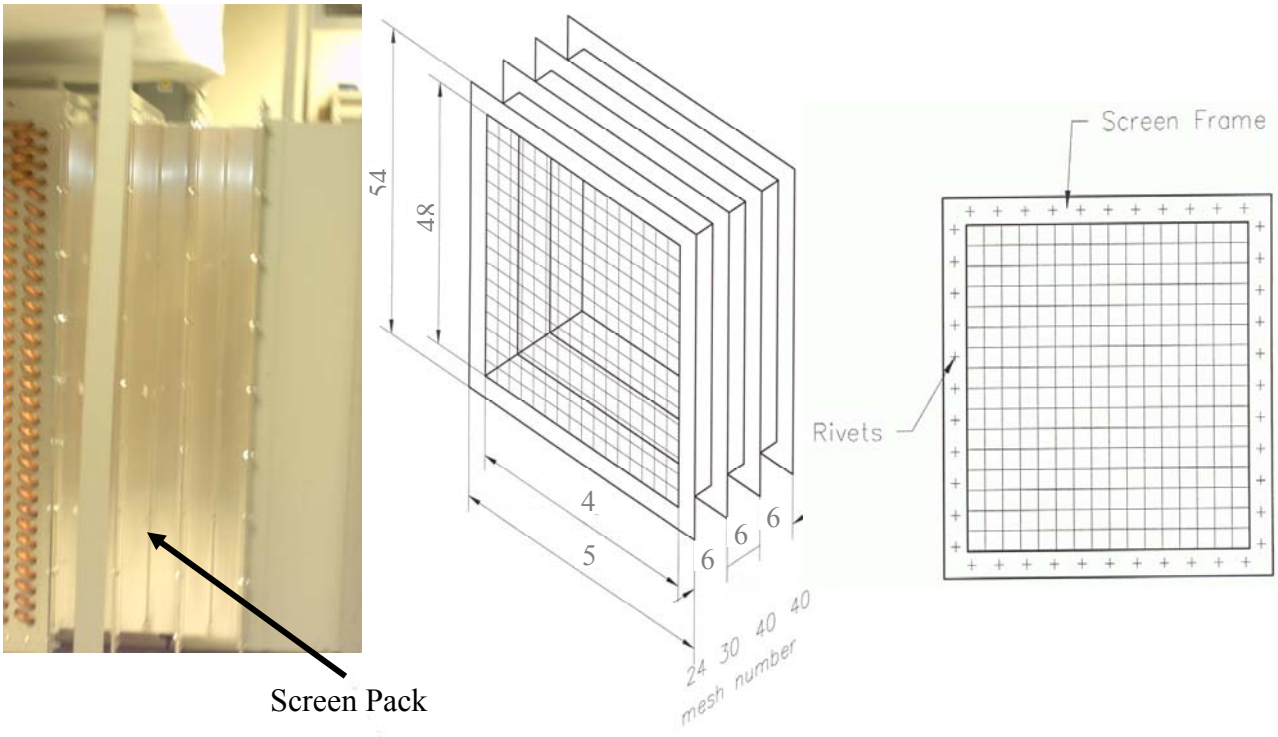

Figure 2.8 The Screen pack and its design schematic

2.1.7 Contraction

The contraction is three dimensional (Fig.2.9), with convergence in both the horizontal and vertical directions. The inlet area is 48 inches x 48 inches, and the outlet area is 36 inches x 0.5 inch. The contraction ratio is 10.8 with 48 inches total length. The vertical contraction ratio is 1.33, and the horizontal contraction is 8. Its contour is designed by two cubic curves with inflection point ($d^2y/dx^2 = 0$) at x/L = 0.6 in each direction. The curvature of both inlet and outlet planes are zero and extended flat for 1 inch. The curves for the top and bottom curvature are obtained as follows:

The equation for vertical direction curve is given as: $G_1 = F_1 - F_2$ (1)

Where

$$F_1(x) = a_1 x^3 + a_2 x^2 + a_3 x + a_4 \quad (2)$$

$$F_2(x) = a_5 x^3 + a_6 x^2 + a_7 x + a_8 \quad (3)$$

The boundary conditions are:

$F_1(x) = 24$ at x = 1.0 (inch)

$F_2(x) = 18$ at x = 48.0 (inches)

$\frac{dF_1(x)}{dx} = 0$ at x = 1.0 (inch) --- zero slope at the inlet

$\frac{dF_2(x)}{dx} = 0$ at x = 48.0 (inches) --- zero slope at the exit

$\frac{d^2F_1(x)}{dx^2} = 0$ at x = 28.8 (inches) --- location for the inflection point

$\frac{d^2F_2(x)}{dx^2} = 0$ at x = 28.8 (inches) --- location for the inflection point

$F_1(x) = F_2(x)$ at x = 28.8

$$\frac{dF_1(x)}{dx} = \frac{dF_2(x)}{dx}$$ at x = 28.8 --- matching slopes at the inflection point

The equation for the horizontal curve is given by: $G_2 = F_3 - F_4$ (4)

Where

$$F_3(x) = b_1 x^3 + b_2 x^2 + b_3 x + b_4 \quad (5)$$

$$F_4(x) = b_5 x^3 + b_6 x^2 + b_7 x + b_8 \quad (6)$$

The boundary conditions are:

$F_3(x) = 24$ at x = 1.0

$F_4(x) = 3$ at x = 48.0

$$\frac{dF_3(x)}{dx} = 0 \text{ at } x = 1.0$$

$$\frac{dF_4(x)}{dx} = 0 \text{ at } x = 48.0$$

$$\frac{d^2F_3(x)}{dx^2} = 0 \text{ at } x = 28.8$$

$$\frac{d^2F_4(x)}{dx^2} = 0 \text{ at } x = 28.8$$

$F_3(x) = F_4(x)$ at x = 28.8

$$\frac{dF_3(x)}{dx} = \frac{dF_4(x)}{dx}$$ at x = 28.8

The coefficients $a_1, a_2, a_3, a_4, a_5, a_6, a_7, a_8$ and $b_1, b_2, b_3, b_4, b_5, b_6, b_7, b_8$ are computed using an MS Excel program and the coordinates are tabulated in Tables 2.2 and 2.3. This contraction is constructed by cutting and welding 12 gauge galvanized steel plate. The corner is filled with polyurethane of a 1.6 cm radius to reduce secondary corner flow. Detail dimension of the contraction nozzle is shown in Fig. 2.9.

Table 2.2 x-y Coordinates of top and bottom surface curvature of contraction (Units: Inches)

x	y	x	y	x	y	x	y	x	y	x	y
1.00	24.00	9.20	23.48	17.40	22.13	25.60	20.31	33.80	18.62	42.00	18.05
1.20	24.00	9.40	23.45	17.60	22.09	25.80	20.26	34.00	18.60	42.20	18.04
1.40	24.00	9.60	23.43	17.80	22.05	26.00	20.21	34.20	18.57	42.40	18.04
1.60	24.00	9.80	23.40	18.00	22.01	26.20	20.16	34.40	18.55	42.60	18.03
1.80	23.99	10.00	23.37	18.20	21.97	26.40	20.12	34.60	18.52	42.80	18.03
2.00	23.99	10.20	23.35	18.40	21.93	26.60	20.07	34.80	18.50	43.00	18.03
2.20	23.99	10.40	23.32	18.60	21.88	26.80	20.02	35.00	18.48	43.20	18.02
2.40	23.98	10.60	23.29	18.80	21.84	27.00	19.97	35.20	18.46	43.40	18.02
2.60	23.98	10.80	23.27	19.00	21.80	27.20	19.92	35.40	18.44	43.60	18.02
2.80	23.97	11.00	23.24	19.20	21.76	27.40	19.88	35.60	18.41	43.80	18.02
3.00	23.97	11.20	23.21	19.40	21.72	27.60	19.83	35.80	18.40	44.00	18.01
3.20	23.96	11.40	23.18	19.60	21.67	27.80	19.78	36.00	18.38	44.20	18.01
3.40	23.95	11.60	23.15	19.80	21.63	28.00	19.73	36.20	18.36	44.40	18.01
3.60	23.94	11.80	23.12	20.00	21.59	28.20	19.68	36.40	18.34	44.60	18.01
3.80	23.93	12.00	23.09	20.20	21.54	28.40	19.64	36.60	18.32	44.80	18.01
4.00	23.92	12.20	23.06	20.40	21.50	28.60	19.59	36.80	18.31	45.00	18.01
4.20	23.91	12.40	23.03	20.60	21.46	28.80	19.54	37.00	18.29	45.20	18.00
4.40	23.90	12.60	23.00	20.80	21.41	29.00	19.49	37.20	18.27	45.40	18.00
4.60	23.89	12.80	22.97	21.00	21.37	29.20	19.45	37.40	18.26	45.60	18.00
4.80	23.88	13.00	22.93	21.20	21.32	29.40	19.40	37.60	18.24	45.80	18.00
5.00	23.87	13.20	22.90	21.40	21.28	29.60	19.36	37.80	18.23	46.00	18.00
5.20	23.85	13.40	22.87	21.60	21.23	29.80	19.31	38.00	18.22	46.20	18.00
5.40	23.84	13.60	22.83	21.80	21.19	30.00	19.27	38.20	18.20	46.40	18.00
5.60	23.83	13.80	22.80	22.00	21.14	30.20	19.23	38.40	18.19	46.60	18.00
5.80	23.81	14.00	22.77	22.20	21.10	30.40	19.19	38.60	18.18	46.80	18.00
6.00	23.80	14.20	22.73	22.40	21.05	30.60	19.15	38.80	18.17	47.00	18.00
6.20	23.78	14.40	22.70	22.60	21.01	30.80	19.11	39.00	18.16	47.20	18.00
6.40	23.76	14.60	22.66	22.80	20.96	31.00	19.07	39.20	18.15	47.40	18.00
6.60	23.75	14.80	22.62	23.00	20.92	31.20	19.03	39.40	18.14	47.60	18.00
6.80	23.73	15.00	22.59	23.20	20.87	31.40	19.00	39.60	18.13	47.80	18.00
7.00	23.71	15.20	22.55	23.40	20.82	31.60	18.96	39.80	18.12	48.00	18.00
7.20	23.69	15.40	22.51	23.60	20.78	31.80	18.93	40.00	18.11		
7.40	23.67	15.60	22.48	23.80	20.73	32.00	18.89	40.20	18.10		
7.60	23.65	15.80	22.44	24.00	20.68	32.20	18.86	40.40	18.10		
7.80	23.63	16.00	22.40	24.20	20.64	32.40	18.83	40.60	18.09		
8.00	23.61	16.20	22.36	24.40	20.59	32.60	18.79	40.80	18.08		
8.20	23.59	16.40	22.33	24.60	20.54	32.80	18.76	41.00	18.07		
8.40	23.57	16.60	22.29	24.80	20.50	33.00	18.73	41.20	18.07		
8.60	23.55	16.80	22.25	25.00	20.45	33.20	18.71	41.40	18.06		
8.80	23.52	17.00	22.21	25.20	20.40	33.40	18.68	41.60	18.06		
9.00	23.50	17.20	22.17	25.40	20.35	33.60	18.65	41.80	18.05		

Table 2.3 x-y Coordinates of sides surface curvature of contraction (Units: Inches)

x	y	x	y	x	y	x	y	x	y	x	y
1.00	24.00	9.20	22.16	17.40	17.45	25.60	11.07	33.80	5.18	42.00	3.16
1.20	24.00	9.40	22.08	17.60	17.31	25.80	10.91	34.00	5.09	42.20	3.15
1.40	24.00	9.60	21.99	17.80	17.17	26.00	10.74	34.20	5.00	42.40	3.13
1.60	23.99	9.80	21.90	18.00	17.03	26.20	10.57	34.40	4.92	42.60	3.12
1.80	23.98	10.00	21.81	18.20	16.89	26.40	10.41	34.60	4.83	42.80	3.11
2.00	23.97	10.20	21.72	18.40	16.74	26.60	10.24	34.80	4.75	43.00	3.10
2.20	23.96	10.40	21.62	18.60	16.60	26.80	10.07	35.00	4.67	43.20	3.08
2.40	23.94	10.60	21.53	18.80	16.45	27.00	9.90	35.20	4.60	43.40	3.07
2.60	23.92	10.80	21.43	19.00	16.30	27.20	9.74	35.40	4.52	43.60	3.06
2.80	23.90	11.00	21.33	19.20	16.15	27.40	9.57	35.60	4.45	43.80	3.06
3.00	23.88	11.20	21.23	19.40	16.01	27.60	9.40	35.80	4.38	44.00	3.05
3.20	23.86	11.40	21.13	19.60	15.86	27.80	9.23	36.00	4.32	44.20	3.04
3.40	23.83	11.60	21.03	19.80	15.71	28.00	9.06	36.20	4.25	44.40	3.04
3.60	23.80	11.80	20.92	20.00	15.55	28.20	8.90	36.40	4.19	44.60	3.03
3.80	23.77	12.00	20.82	20.20	15.40	28.40	8.73	36.60	4.13	44.80	3.02
4.00	23.74	12.20	20.71	20.40	15.25	28.60	8.56	36.80	4.07	45.00	3.02
4.20	23.70	12.40	20.60	20.60	15.10	28.80	8.39	37.00	4.01	45.20	3.02
4.40	23.66	12.60	20.49	20.80	14.94	29.00	8.22	37.20	3.96	45.40	3.01
4.60	23.62	12.80	20.38	21.00	14.79	29.20	8.06	37.40	3.91	45.60	3.01
4.80	23.58	13.00	20.26	21.20	14.63	29.40	7.90	37.60	3.86	45.80	3.01
5.00	23.54	13.20	20.15	21.40	14.48	29.60	7.74	37.80	3.81	46.00	3.01
5.20	23.49	13.40	20.03	21.60	14.32	29.80	7.59	38.00	3.76	46.20	3.00
5.40	23.44	13.60	19.92	21.80	14.16	30.00	7.44	38.20	3.72	46.40	3.00
5.60	23.39	13.80	19.80	22.00	14.00	30.20	7.29	38.40	3.67	46.60	3.00
5.80	23.34	14.00	19.68	22.20	13.84	30.40	7.15	38.60	3.63	46.80	3.00
6.00	23.29	14.20	19.56	22.40	13.69	30.60	7.01	38.80	3.59	47.00	3.00
6.20	23.23	14.40	19.43	22.60	13.53	30.80	6.88	39.00	3.56	47.20	3.00
6.40	23.17	14.60	19.31	22.80	13.37	31.00	6.74	39.20	3.52	47.40	3.00
6.60	23.11	14.80	19.18	23.00	13.20	31.20	6.61	39.40	3.48	47.60	3.00
6.80	23.05	15.00	19.06	23.20	13.04	31.40	6.48	39.60	3.45	47.80	3.00
7.00	22.99	15.20	18.93	23.40	12.88	31.60	6.36	39.80	3.42	48.00	3.00
7.20	22.92	15.40	18.80	23.60	12.72	31.80	6.24	40.00	3.39		
7.40	22.85	15.60	18.67	23.80	12.56	32.00	6.12	40.20	3.36		
7.60	22.78	15.80	18.54	24.00	12.39	32.20	6.00	40.40	3.33		
7.80	22.71	16.00	18.41	24.20	12.23	32.40	5.89	40.60	3.31		
8.00	22.64	16.20	18.28	24.40	12.07	32.60	5.78	40.80	3.28		
8.20	22.56	16.40	18.14	24.60	11.90	32.80	5.67	41.00	3.26		
8.40	22.49	16.60	18.01	24.80	11.74	33.00	5.57	41.20	3.24		
8.60	22.41	16.80	17.87	25.00	11.57	33.20	5.47	41.40	3.22		
8.80	22.33	17.00	17.73	25.20	11.41	33.40	5.37	41.60	3.20		
9.00	22.25	17.20	17.59	25.40	11.24	33.60	5.27	41.80	3.18		

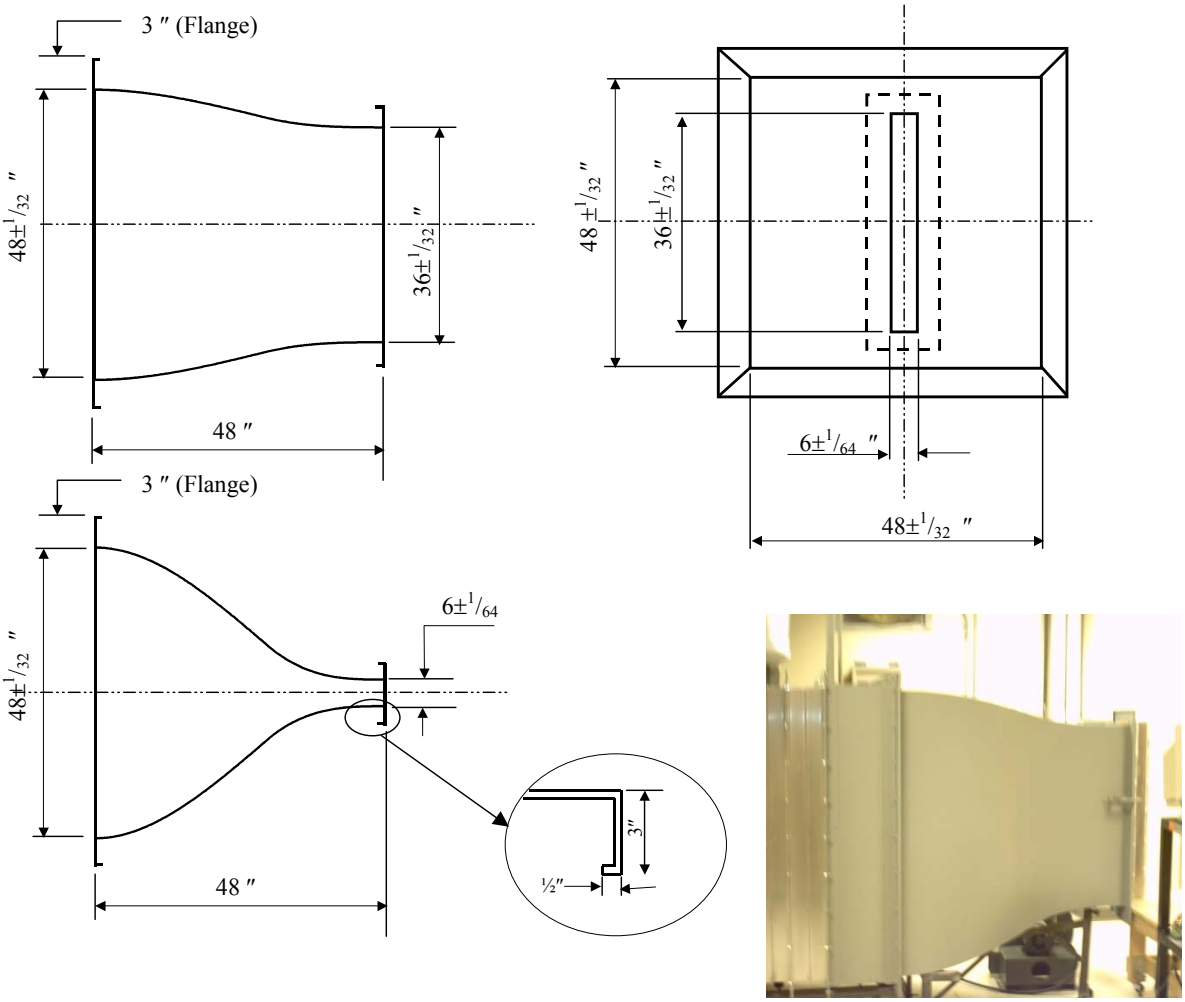

Figure 2.9 Contraction nozzle

2.1.8 Suction

To remove the low-momentum flow near the wall, a boundary layer suction box (Fig. 2.10) is installed between the contraction and test section. The perforated plate with staggered holes of 1/8″ diameter and 3/16″ staggered center is installed at the inlet of the test section. The open area ratio of the perforated plated is 40%. Two layers of 18-mesh screen are installed in the box to improve the inlet uniformity of suction flow. A detailed dimension of the suction box is shown in Fig. 2.10.

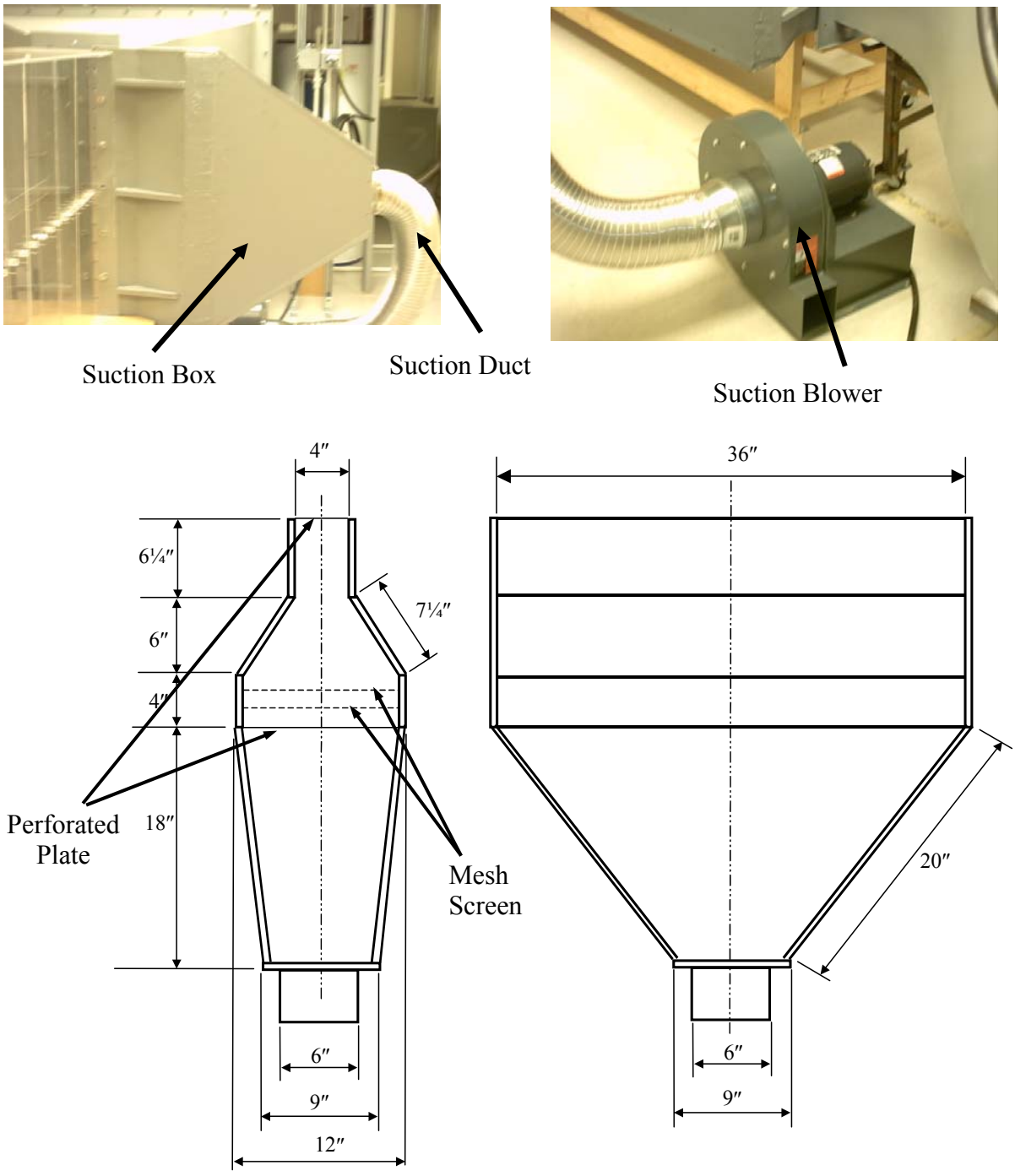

Figure 2.10 Suction box and blow

A six-inch flexible duct connects the suction box to a 3 hp high-pressure fan. The suction blower is powered by a 3 HP, 3-phase motor, and delivers 1127 CFM at 1 inch of water static pressure.

2.1.9 Test Section for Reversed-Flow Combustor Study

The reversed-flow combustor test section consists of a transition section that converts the rectangular exit of the contraction nozzle to a $1/7^{th}$ sector of a circle to simulate a part of the dump diffuser which accommodates reverse-flow can annular gas turbine combustors. The exit of the rectangular-to-circular transition section Fig.2.11 (a) is a section of a circular arc, which subtends an angle of 52° to the center of the circle. This accommodates one full combustor and two dummy one-half of a combustor. The arrangement of the combustors is shown in Fig.2.11 (b). There are two interchangeable test sections: one for flow measurements and the other one for heat transfer study.

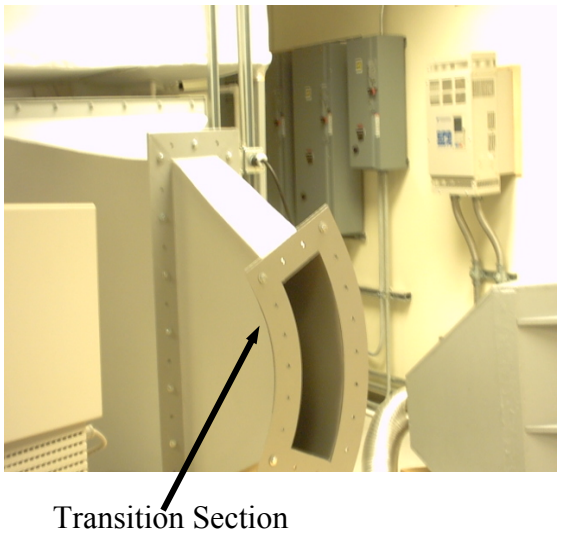

Figure 2.11 (a): Rectangular-to-Circular Transition section for the reverse flow combustor study

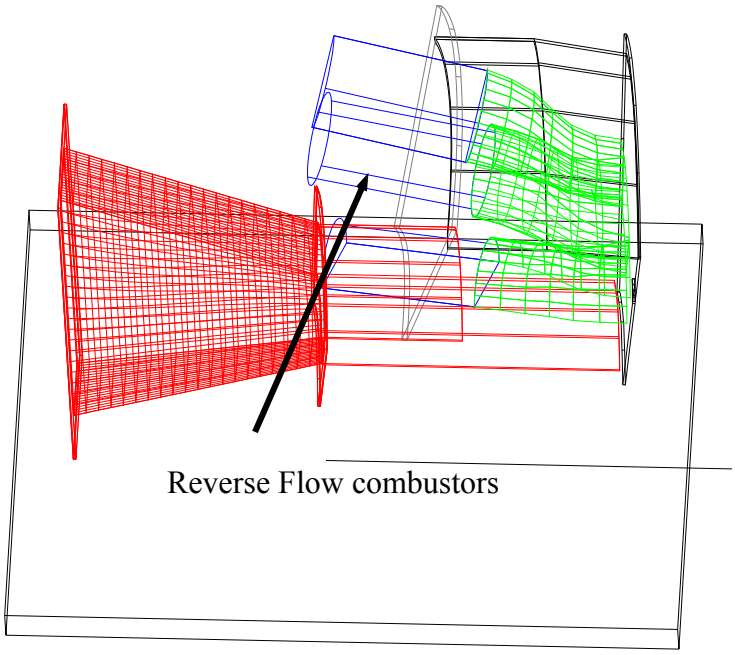

Figure 2.11 (b): Schematic of the test section for the reverse flow combustor study

Fig.2.12 and Fig.2.13 are showing the gas turbine reversed-flow combustor test rig simulating a 1/7th sector of dump diffuser-combustor combination, one for fluid mechanic study, and another for heat transfer study.

Figure 2.12 Gas turbine reversed-flow combustor test rig simulating a 1/7th sector of dump diffuser-combustor combination. There are two interchangeable test sections: one for flow measurements and the other one for heat transfer study

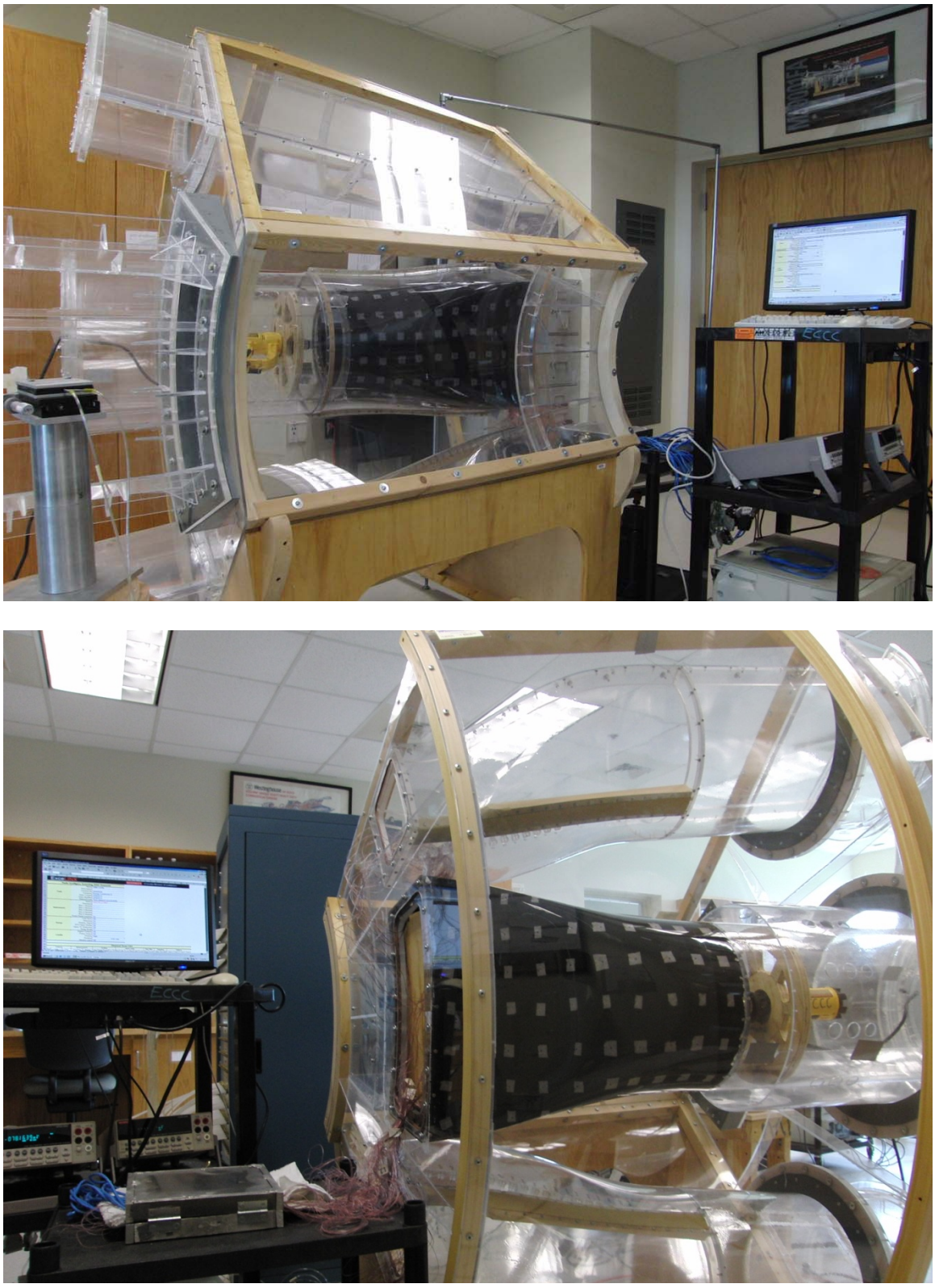

Figure 2.13 Gas turbine reversed-flow combustor heat transfer test rig simulating a 1/7th sector of dump diffuser-combustor combination

Figure 2.14 shows a scaled-down Plexiglas combustor model used as a visual reference to build the larger combustor model to be installed in the test section. The plexiglas combustor model is constructed via vacuum forming process. (Need to insert the description for the test section for flow study.) .

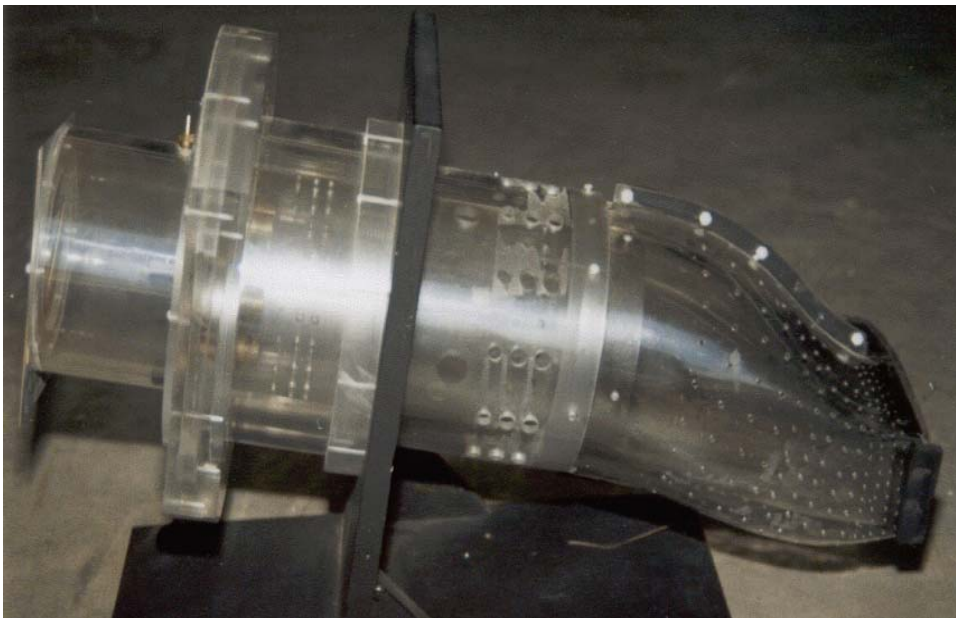

Figure 2.14 Single combustion chamber model

The transition piece was outfit with a sheath to provide two types of enhanced cooling. First, hundreds of holes were drilled on the sheath to provide air passages for creating hundreds of small jets that impinge on the transition piece and provide local enhanced cooling. Second, the narrow gap between the sheath and transitional piece serves as a narrow channel that speeds up the air flow and provides additional high convective cooling of the transitional piece and combustion chamber walls. The sheath surrounding the transition piece is seamlessly connected to the sleeve outside the combustion chamber wall. The plastic sheath model is showing in Fig.2.15.

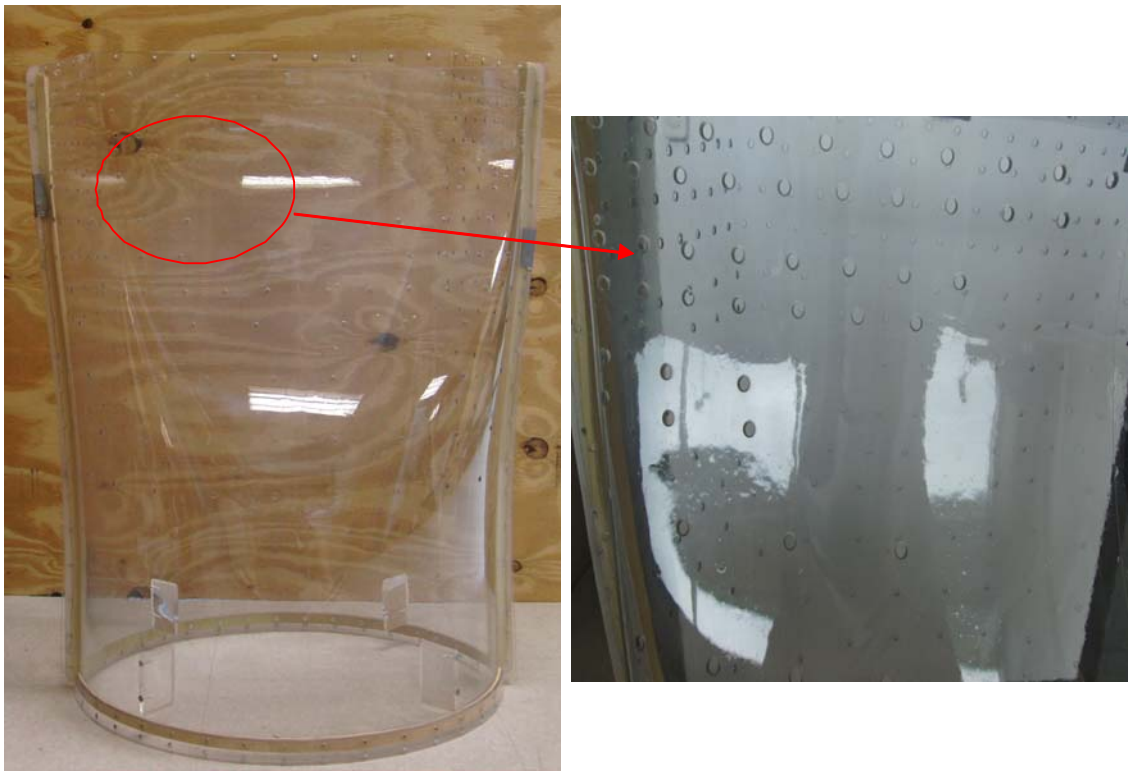

Figure 2.15 Plastic sheath model

For the fluid mechanic study test section, pitot-static tube is inserted into the rectangular-to-circular transition section to measure flow velocity by averaging at least five different locations in the same vertical cross section (see Section 2.4.1).

To monitor the pressure changes on the combustor chamber wall, 154 pressure taps installed. The overview of these pressure taps' location is showing in Fig.2.15. All these pressure taps are grouped into 8 serials, from Fig.2.16 to Fig.2.19 explain the pressure tap's locations with attached numbers. And Table 2.4 explains the acronyms of the pressure taps' naming system.

Then, apply section 2.4.2 (Procedure for Adjusting Zero and Span of Signal Conditioners) and section 2.4.3 (Procedure for Calibrating Pressure Transducer) to get the pressure measurement data.

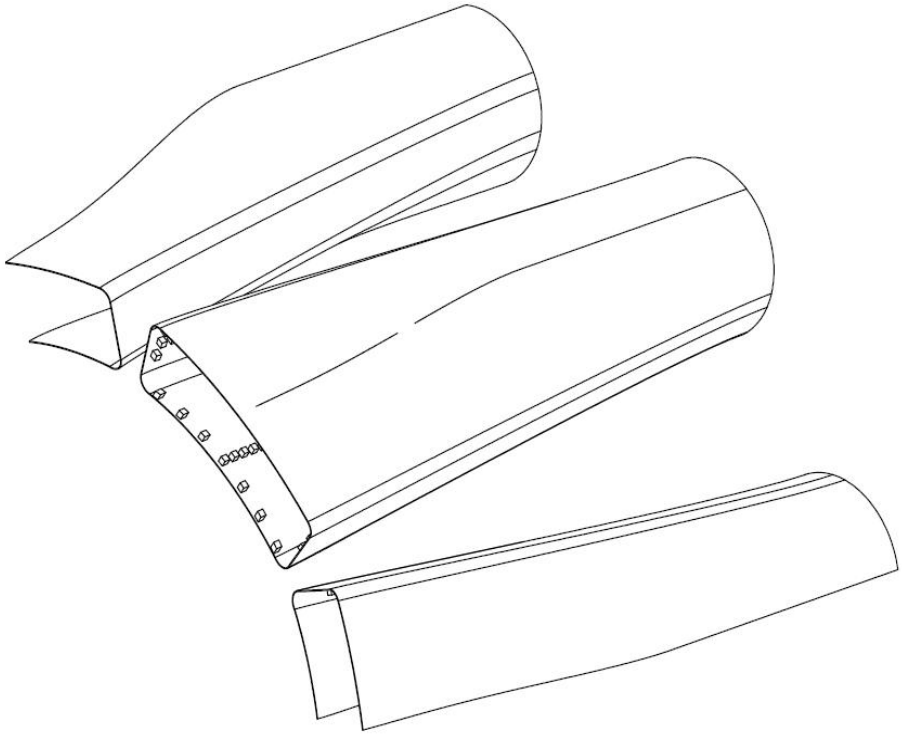

Figure 2.16 Overview of combustion chamber with pressure taps

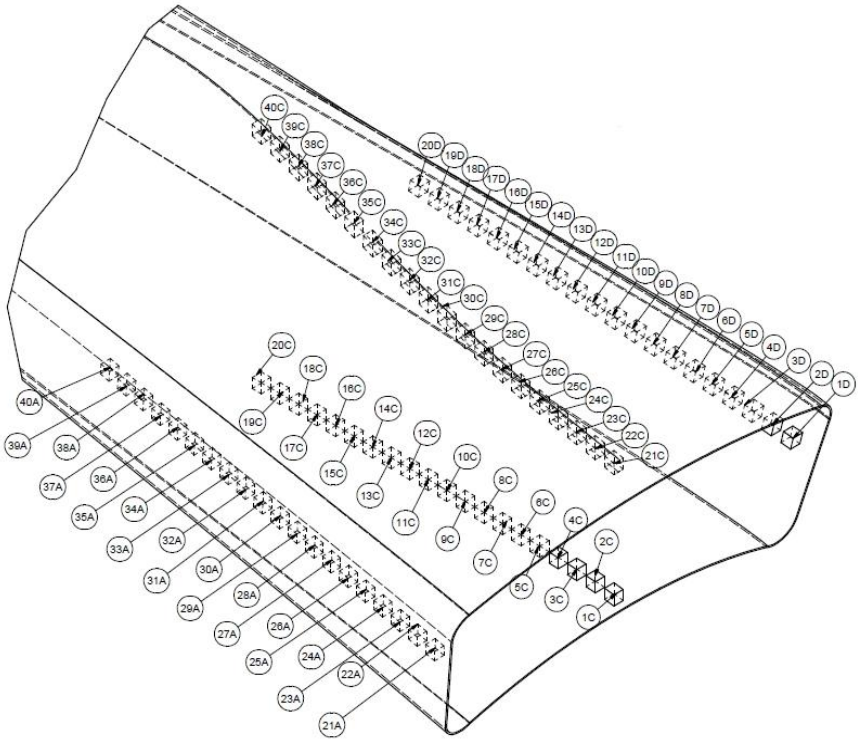

Figure 2.17 Middle chamber with pressure taps

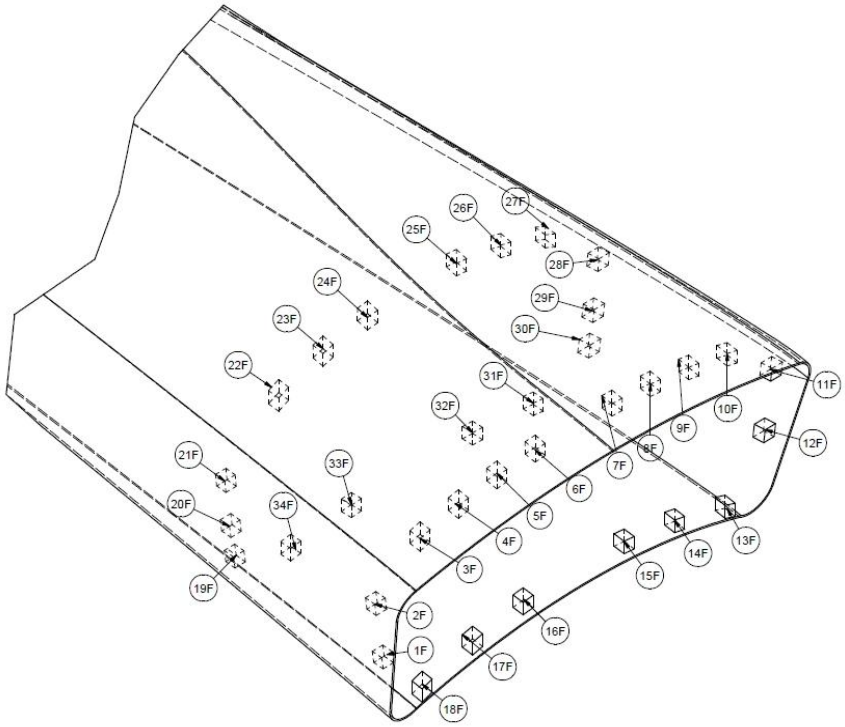

Figure 2.18 Middle chamber with radial pressure taps

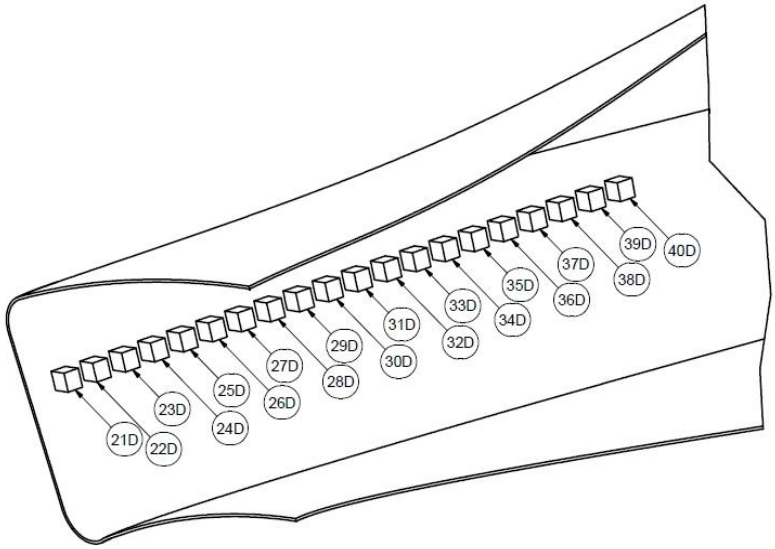

Figure 2.19 Bottom chamber with pressure taps

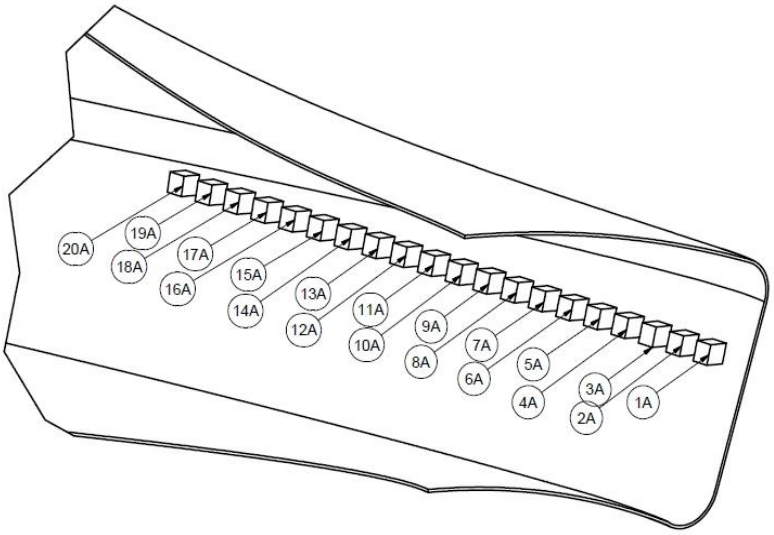

Figure 2.20 Top chamber with pressure taps

Table 2.4 Static port location on combustor model

Top Chamber:	Module Channel	5 1-20	
Middle Chamber:	Top:	Module Channel	1 21-40
	Bottom:	Module Channel	1 1-20
	Right:	Module Channel	6 1-20
	Left:	Module Channel	5 21-40
	Back:	Module Channel	2 19-34
	Front:	Module Channel	2 1-18
Bottom Chamber:	Module Channel	6 21-40	

In the heat transfer test section, the combustor chamber is heated by forced convection. Both ends of the mid–chamber are closed and a heat gun (1.55 kW) is installed inside the combustor chamber and blows hot air that is recirculated in the closed combustor (Fig.2.21) and provides the heated boundary condition for heat transfer study of the mid-chamber and transitional piece walls. The heated section is instrumented with 80 E-type (chromel-constantan) 36 gauge (0.01 inch) thermocouples, manufactured by Omega's Fine Duplex Insulated Thermocouple Wire (TT-E-36-1000). Each thermocouple is first taped to the designated location by applying a piece of scotch tape (Fig.2.22 (a) and (c)). Black spray-on rubber is then carefully painted on the surface to fasten the thermocouples (Fig.2.22 (b) and (d)). The power density is approximately rated 1.5W/cm^2. (see Appendix A for detail) This arrangement assures that the thermocouple junctions are well protected and fixed in place.

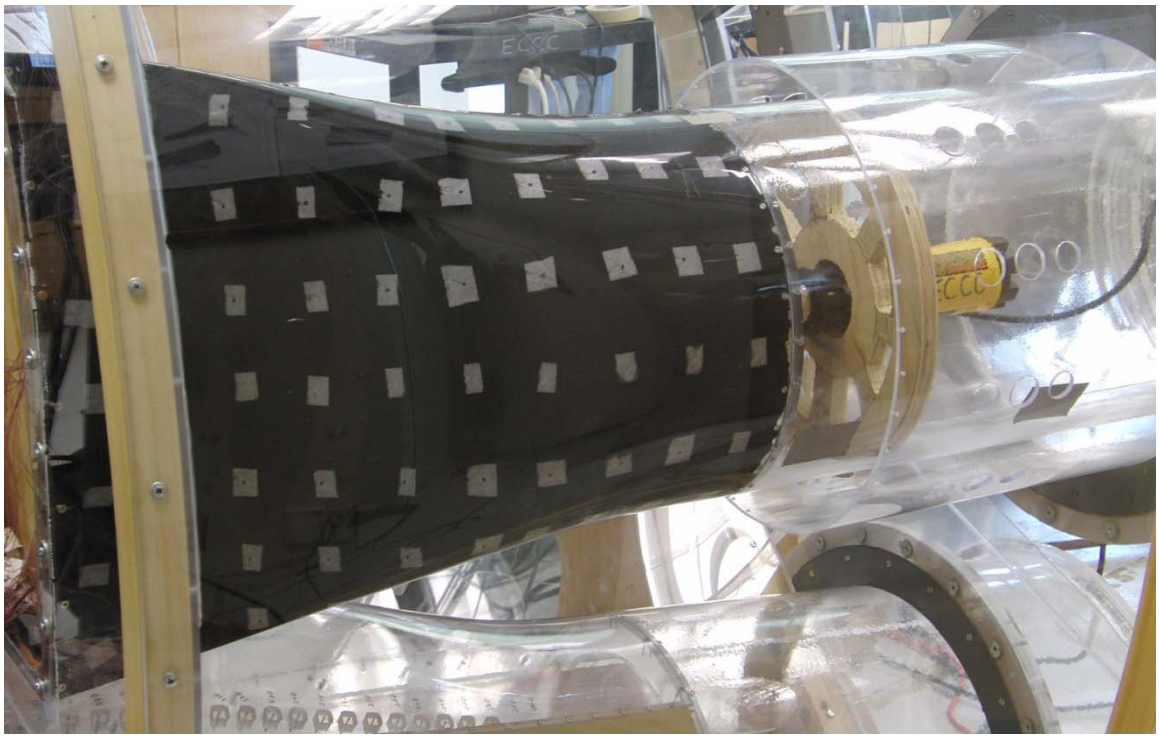

Figure 2.21 Closed combustor chamber with heat gun accommodated inside

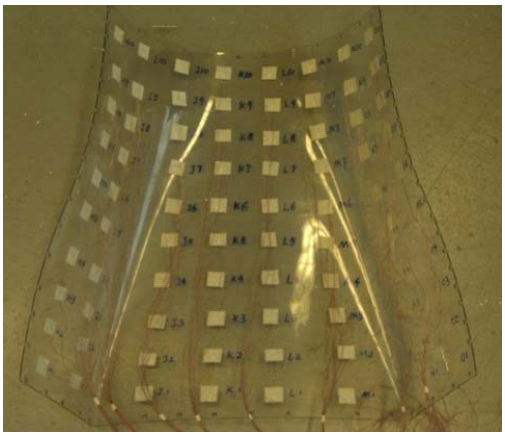

(a)

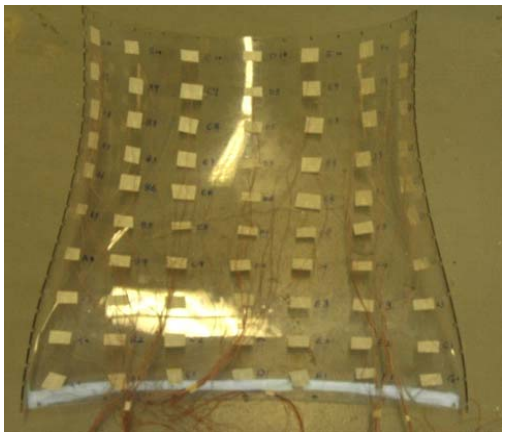

(c)

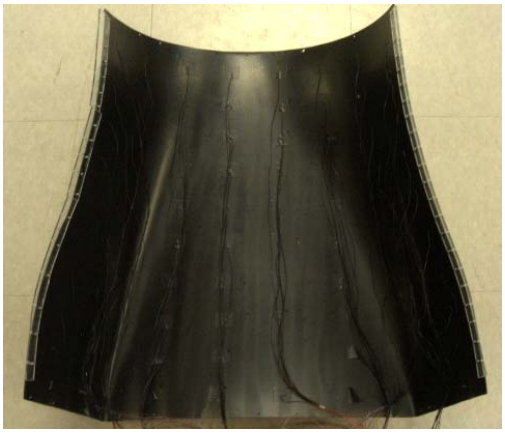

(b)

(d)

Figure 2.22 Transitional pieces instrumented with 80 thermocouples in (a) and(c), painted black spray-on rubber in (b) and (d)

There are eight columns (parallel to the main stream direction) of thermocouples instrumented on the transitional piece and combustion chamber walls. Each column has 10 thermocouples. These thermocouples' locations are shown in Fig.2.23 and Fig.2.24. These thermocouple columns are named according to their locations on the transitional piece and combustion chamber walls. Table 2.5 and Table 2.6 explain the acronyms of the thermocouple naming system.

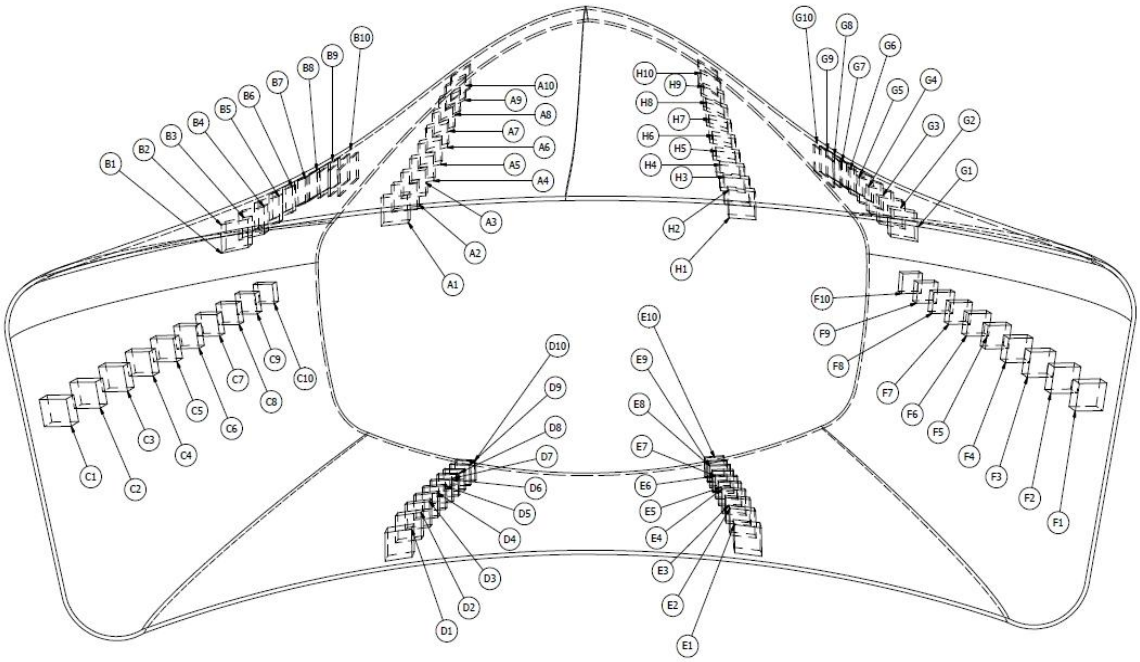

Figure 2.23 Thermocouples on combustion chamber

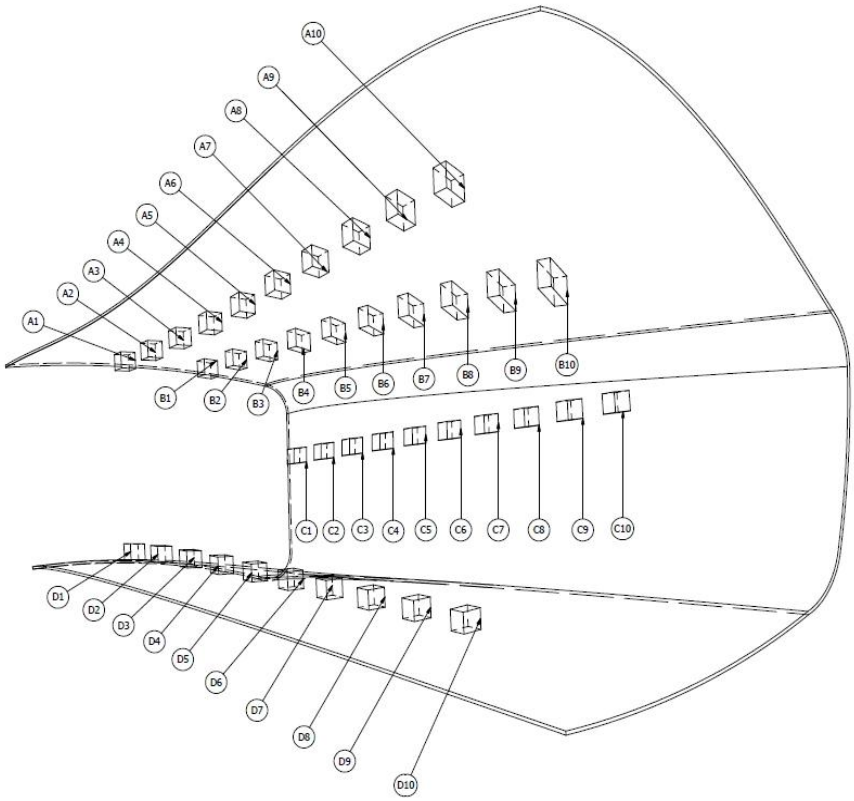

Figure 2.24 Thermocouples on split combustion chamber

Table 2.5 Thermocouples' location record

Number \ Column	A	B	C	D	E	F	G	H
1	TML	TL	L	BL	BR	R	TR	TMR
2	TML	TL	L	BL	BR	R	TR	TMR
3	TML	TL	L	BL	BR	R	TR	TMR
4	TML	TL	L	BL	BR	R	TR	TMR
5	TML	TL	L	BL	BR	R	TR	TMR
6	TML	TL	L	BL	BR	R	TR	TMR
7	TML	TL	L	BL	BR	R	TR	TMR
8	TML	TL	L	BL	BR	R	TR	TMR
9	TML	TL	L	BL	BR	R	TR	TMR
10	TML	TL	L	BL	BR	R	TR	TMR

Table 2.6 Thermocouple location on combustion chamber and transitional piece walls

TR	=	Top right column
TMR	=	Top-middle right column
TML	=	Top-middle left column
TL	=	Top left column
L	=	Left column
BL	=	Bottom left column
BR	=	Bottom right column
R	=	Right column

Then follows section 2.4.4 (Procedure for Temperature Measurement) to complete the measurement.

2.2 Instrument

2.2.1 Automatic Probe Traversing System

The automatic probe traversing system consists of a traversing stage and a motion controller/driver. The traversing stage is an ILS series linear stage of 100 mm travel range manufactured by Newport Corporation (Model No. LTA-HS).

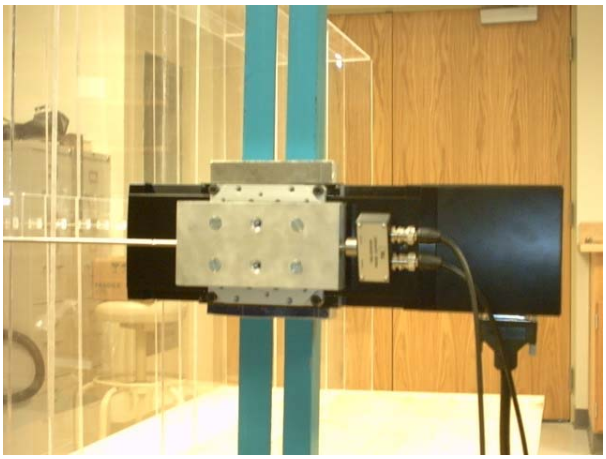

Figure 2.25 (a):Automatic traversing stage

Figure 2.25 (b):Automatic traversing stage motion controller and driver

The traversing stage shown in Fig. 2.25 (a) has the following specifications:

Base Material:	Extruded Aluminum
Drive Mechanism:	Backlash-free ball screw
Motor:	DC Servo motor UE404S2
Travel Range	100 mm
Resolution	0.5 μm
Uni-directional Repeatability	1.5 μm
Reversal Value (Hysteresis)	1 μm
One Axis Accuracy	5 μm

Maximum speed 50 mm/sec

The motion controller/driver ESP300 is a 2-axis controller upgradeable to 3-axis (Fig. 2.25(b)). The ESP300 is an integrated controller and driver in one chassis. It controls up to three axes of motion using any combination of DC and/or stepper motors. It uses a 32-bit, floating point, DSP processor for high precision synchronized control. A digital PID-FF (feed-forward) servo loop ensures precise velocity profile tracking and accurate positioning.

2.2.2 Automatic Pressure Scanning and Data Acquisition System

Pressure measurements are fundamental to many aerothermal and energy conversion experiments. Usually measurements taken at many points are needed. A Multiple Scanivalve System (MSS-48C) has been acquired from Scanivalve Inc. It is shown in Fig.2.26. This pressure system, employing a mechanical multiplexer mechanism, is designed with pneumatic selector switches, stepper motors, a pressure input panel, and a cabinet. The heart of the system is the Scanivalve Module, which is basically a rotational pneumatic selector switch. Each module connects 48 pressure inputs sequentially to a single pressure transducer mounted inside the module. The system accommodates a total of 6 modules and accepting a total of 288-channel pressure inputs. Each includes a 48-channel pneumatic selector switch, a 10-inch WC pressure transducer and a signal conditioner. Pressure transducers with different ranges can be installed to the system later.

Nowadays, many research and industrial facilities are employing pressure scanners with electronic switches, such as Intelligent Digital Sensor Array (DSA) products from Scanivalve Inc. or Pneumatic Intelligent Pressure Scanners (PIPS) from Pressure Systems, Inc. The electronic pressure scanners require one pressure transducer and one signal conditioner for each pressure

input, while the mechanical switch only uses one pressure transducer and signal conditioner for 48 channels. Calibrating one pressure transducer and one signal conditioner for one 48-channel

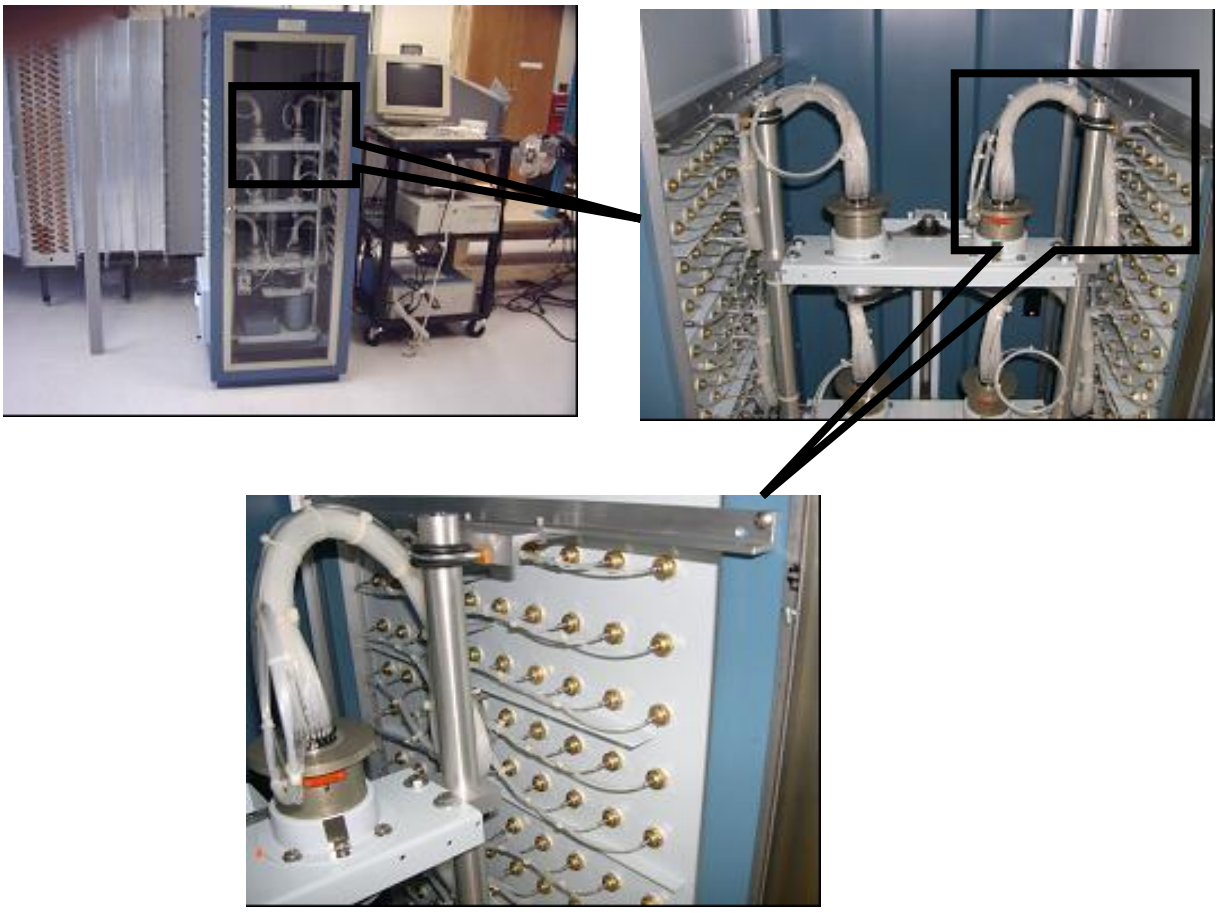

Figure 2.26 Scanivalve pressure measurement system

mechanical module is much easier than calibrating 48 transducers and signal conditioners. Furthermore, the pressure transducer can be easily replaced with different ranges for the mechanical module. The pressure transducer range for each electronic model is almost fixed (change is possible, but it is a cumbersome and expensive process). Therefore, this project chooses the conventional mechanical module system instead of the electronic module system.

Detailed electronic-mechanical operating mechanism and data acquisition process are shown in Figs.2.27 and Fig.2.28, respectively. The stepper motor drives the Scanivalve modules through the common drive shaft and the timing belt. At each step, one pressure input is connected to the

pressure transducer inside a specific module. The pressure signal is transferred and recorded to a data logger or a computer. The stepper motor is controlled by two commands “Home” and “Step”, and the rotation speed of the Scanivalve module (ie. scanning rate) is controlled by the command sent from the computer. The maximum scanning rate is 20 ports per second. A user interface is designed and constructed in house to control the rotation speed of the Scanivalve module and to synchronize the motor rotation and pressure reading. Two IC boards, model number PCIDAQ 1210 and CyPDISO 8P, are purchased from CyberResearch Inc. and installed to a personal computer. The IC board PCIDAQ is used to read the pressure data, while the IC board CyPDISO 8P is used to control the motor and thus rotation speed. After data is recorded, further analysis can be conducted offline. The overview of the Scanivalve pressure data acquisition system is shown in Fig.2.29.

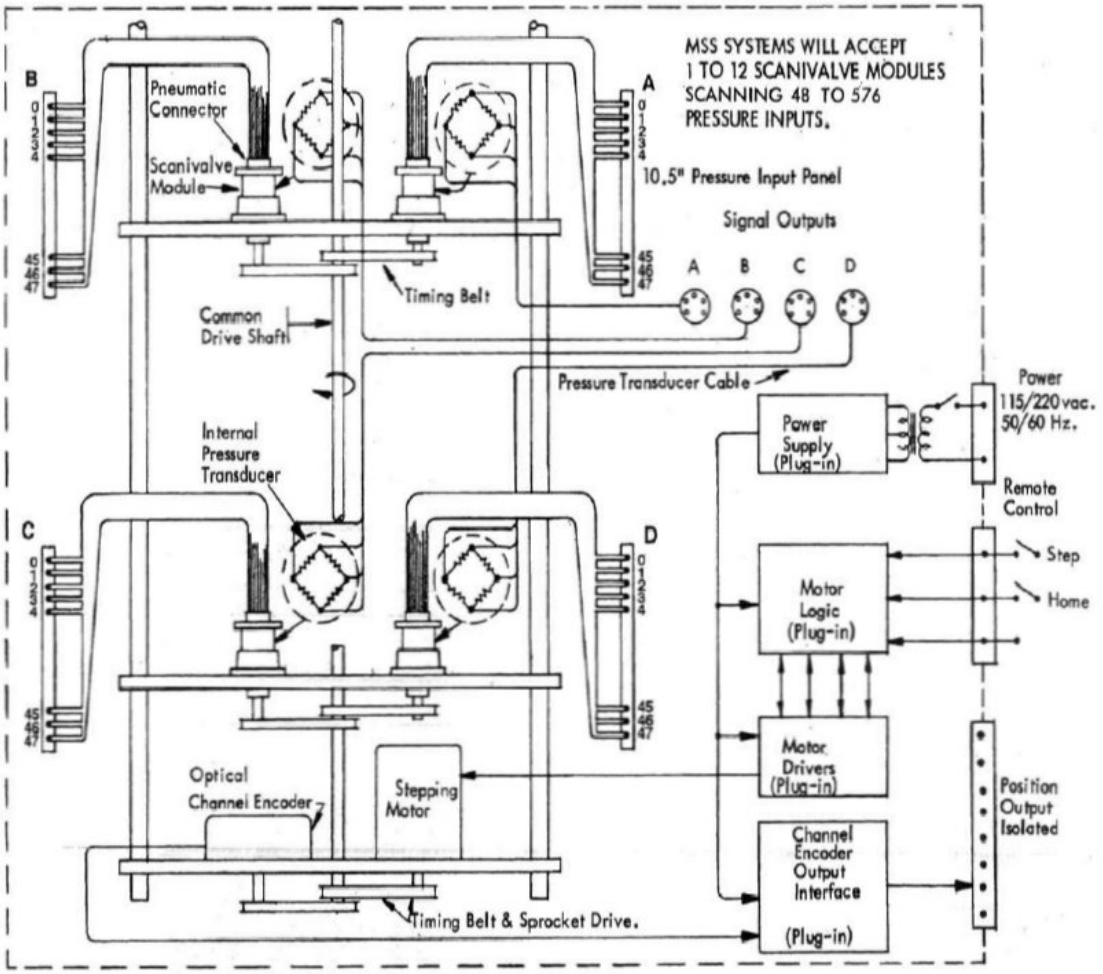

Figure 2.27 Scanivalve pressure system connections and control

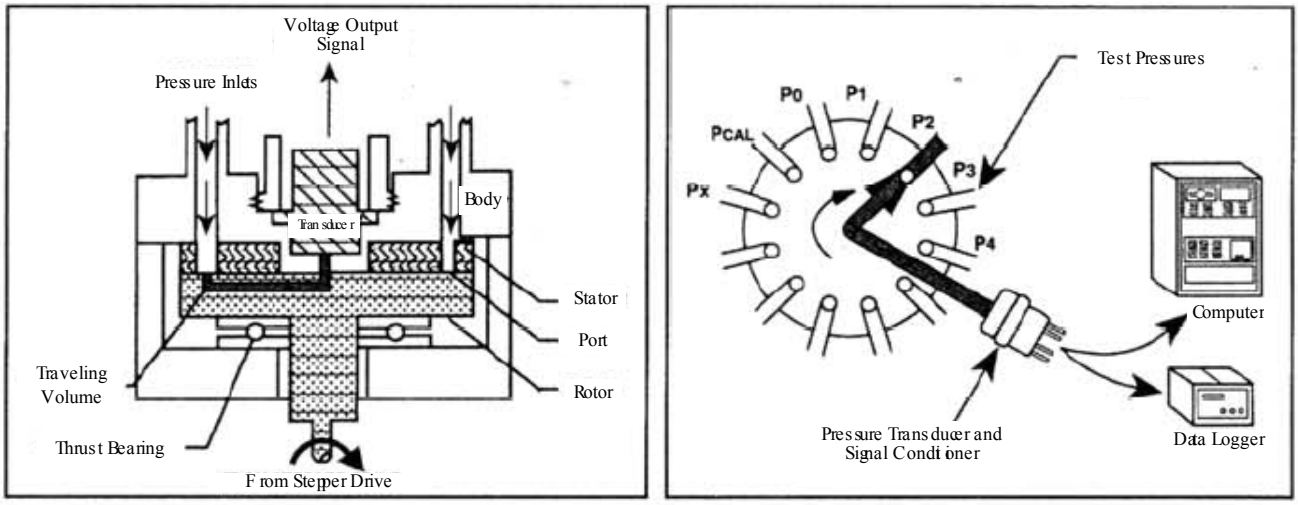

Figure 2.28 Scanivalve module and measurement mechanism

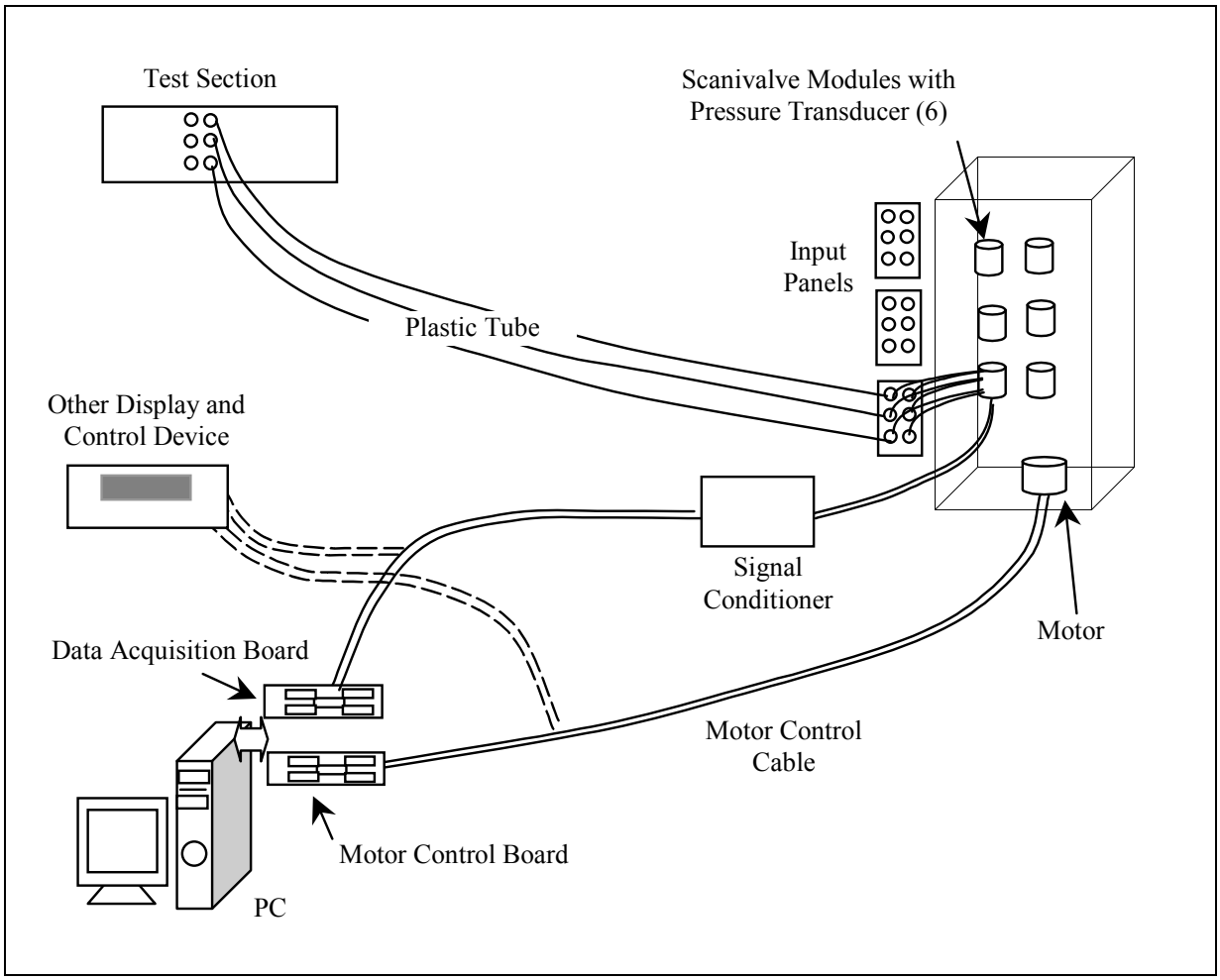

Figure 2.29 Overview of the Scanivalve pressure data acquisition system

To control the data acquisition process, a software application is developed in house using Visual Basic. Fig.2.30 shows the main interface of this software.

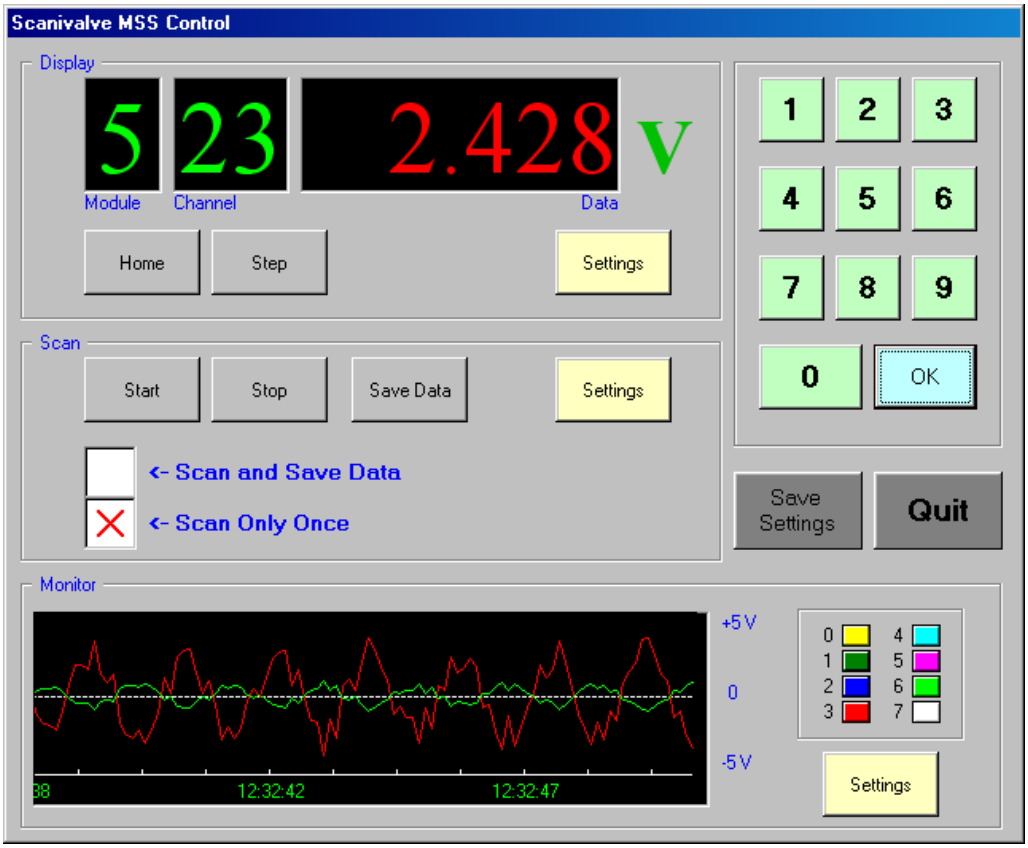

Figure 2.30 In-house designed application's interface to control the pressure scanner system

2.2.3 Thermocouple Measuring and Data Acquisition System

Two Keithley model 2700-multimeter/data acquisition systems shown in Fig.2.31 are used to measure the thermocouple voltage readings. The Model 2700 Multimeter/Data Acquisition System is a high-performance, half-rack instrument that combines the functionality and high channel count of a datalogger with the accuracy, convenience, and stability of 6-1/2-digit Digital Multimeter. The Model 2700 provides 80 channels or 40 differential channels of multiplexed measurement and control. The two multimeters give a total of 160 channels or 80 differential channels. The Model 2700 reads as low as 0.1 μV and provides a digitizing

capability with the equivalent of 22-bit A/D resolution. The highest scanning rate is 65 channels/second and the highest sampling speed is 2000/sec, which is more than sufficient for thermocouple measurements.

Two Keithley 2700-multimeter/data-acquisition systems

Thermocouple wires and RS 232 connectors at the back of the multimeter

Figure 2.31 Keithley model 2700-multimeter/data acquisition systems

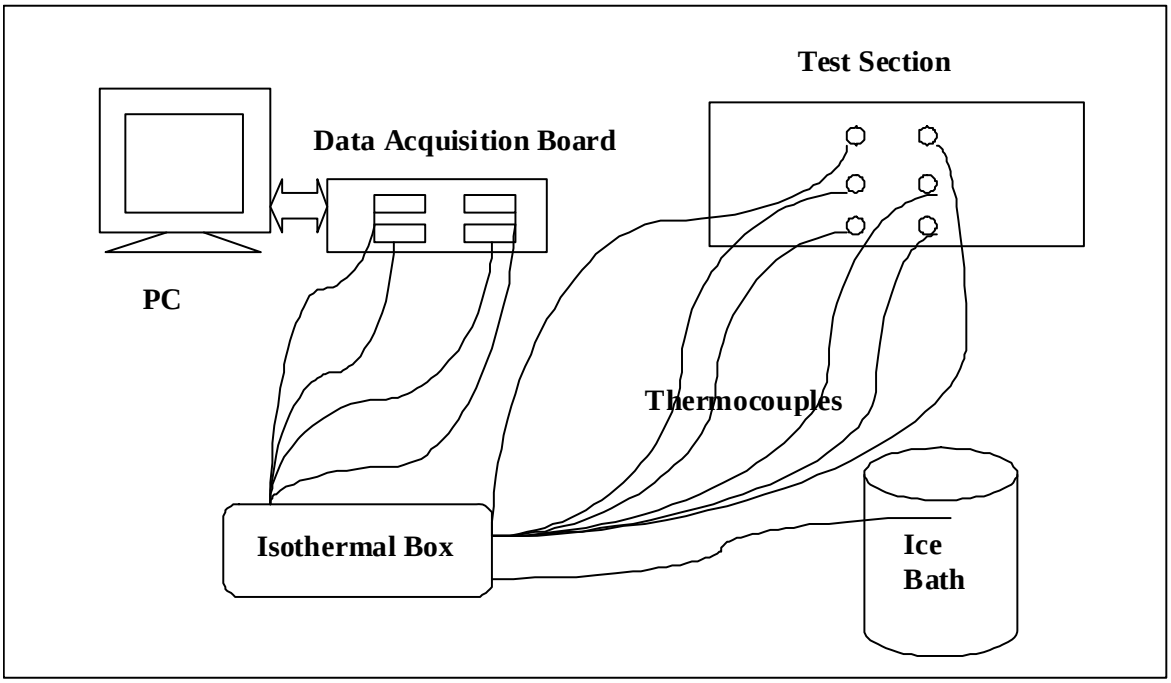

Figure 2.32 Overview of temperature measurement system

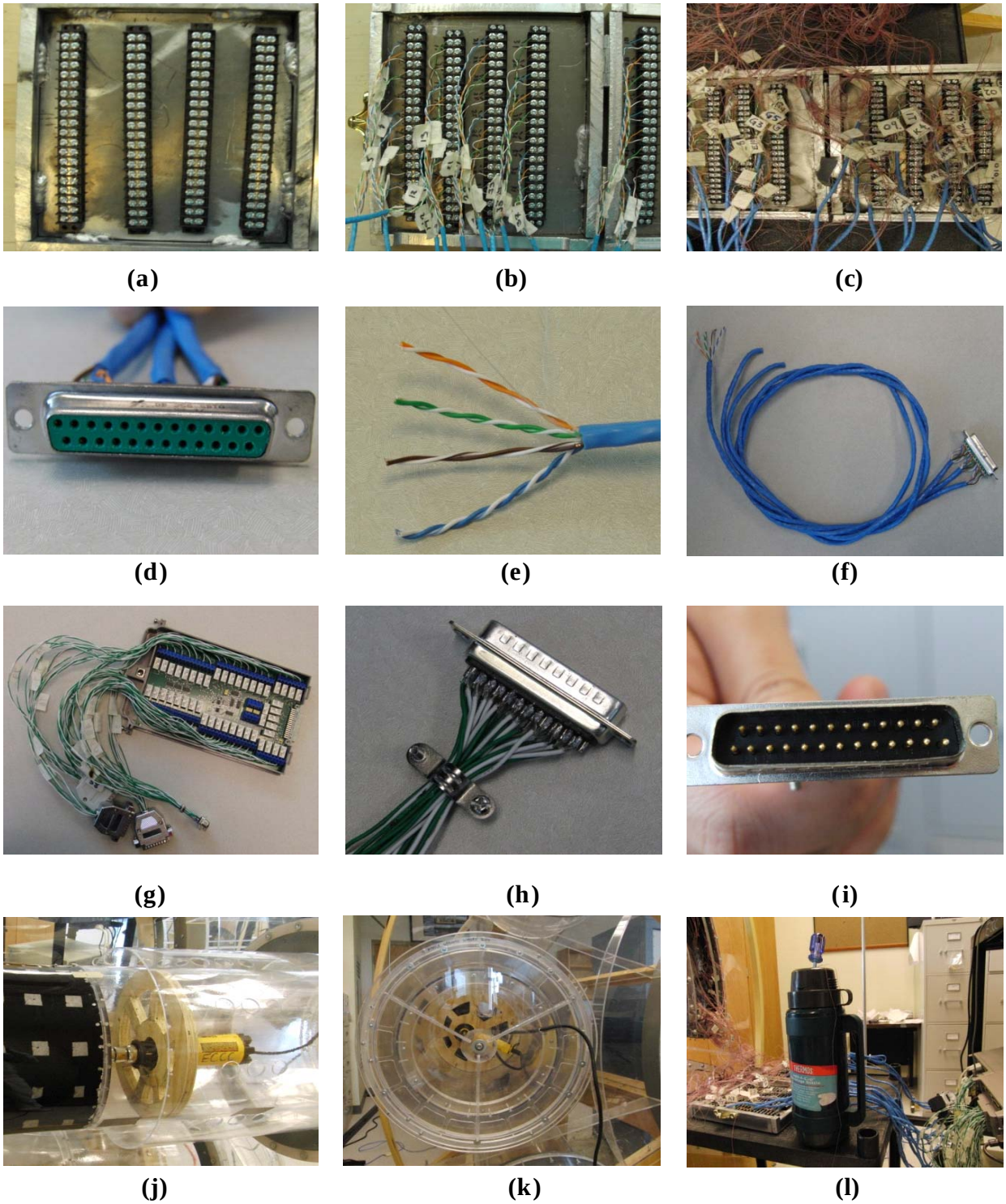

Figure 2.33 Components used in the thermocouple measurement (a),(b) and (c) are internal views of isothermal box setting up steps; (d),(e) and (f) are copper wires and RS232 connectors used to connect isothermal box and data acquisition board; (g),(h) and (i) are data acquisition board and its connectors ; (j) and (k) are different views of heat gun accommodated in the combustion chamber; (l) is the thermal bottle contains the ice bath

The temperature measurement system uses in-house designed isothermal box, which is fabricated by 1-inch thickness aluminum blocks. The isothermal box provides a massive body to isolate the thermocouple-copper junctions inside the isothermal box from the ambient temperature fluctuation and therefore reduces the unsteadiness-introduce uncertainty of the experiment. The constant ice melting temperature of the ice bath is used to be a reference temperature. The readings from the data acquisition system indicate the relative temperature difference between the thermocouple measurement location and the isothermal box temperature. To determine the absolute temperature at the thermocouple junction, the temperature difference between the isothermal box and ice bath is added on the data acquisition readings. Therefore, the actual temperature of the isothermal box is not important, rather the uniformity and steadiness of the isothermal box temperature provide a system that renders a good quality temperature measurement. Fig.2.32 shows the schematic of the thermocouple temperature measuring and data acquisition system. Fig.2.33 lists all the components used in this system.

2.2.4 Hot Wire Anemometry System

The hot wire anemometry system shown in Fig.2.34 is the core for measuring flow and turbulent structures. The IFA 300 hot-wire anemometer system, manufactured by TSI Inc., is expandable to 16 channels. It provides up to 300 kHz frequency response. Each module is designed with a built-in thermocouple circuit for measuring fluid temperature and for making temperature corrections. All operations, including setup, calibration, and data acquisition are software-controlled via an RS-232 interface. The existing IFA system has been upgraded to include three constant temperature modules and one constant current module. The constant temperature modules are used with hot wire sensors to measure flow and turbulence structures, while the constant current module is used with a cold wire to measure temperature fluctuations.

The hot-wire anemometry outputs are acquired and digitized via a 16-channel, 16-bit data acquisition system using the ADCWIN 16 A/D board (United Electronic Industries. Model No. ADCWIN 16). The overall system layout is shown in Fig.2.35.

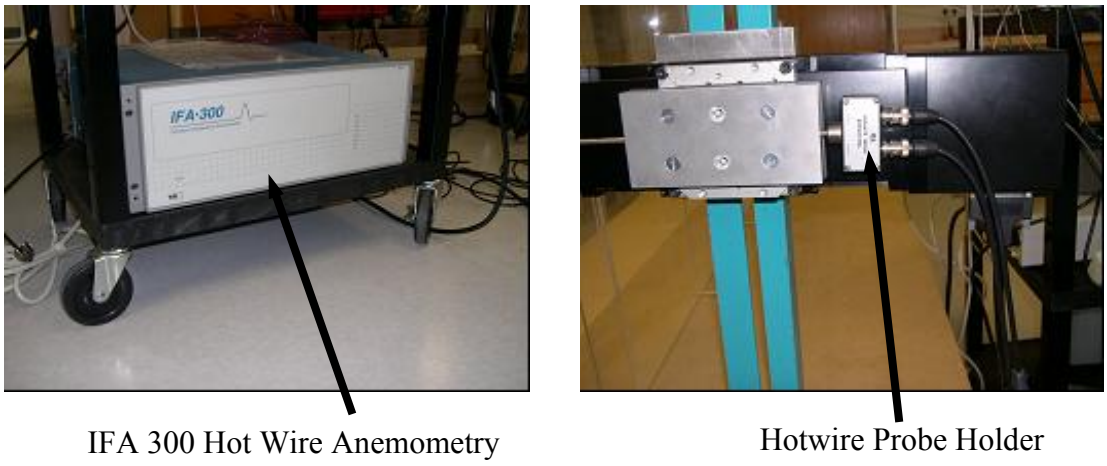

Figure 2.34 Hot-wire anemometry and 3-D automatic traversing measuring system

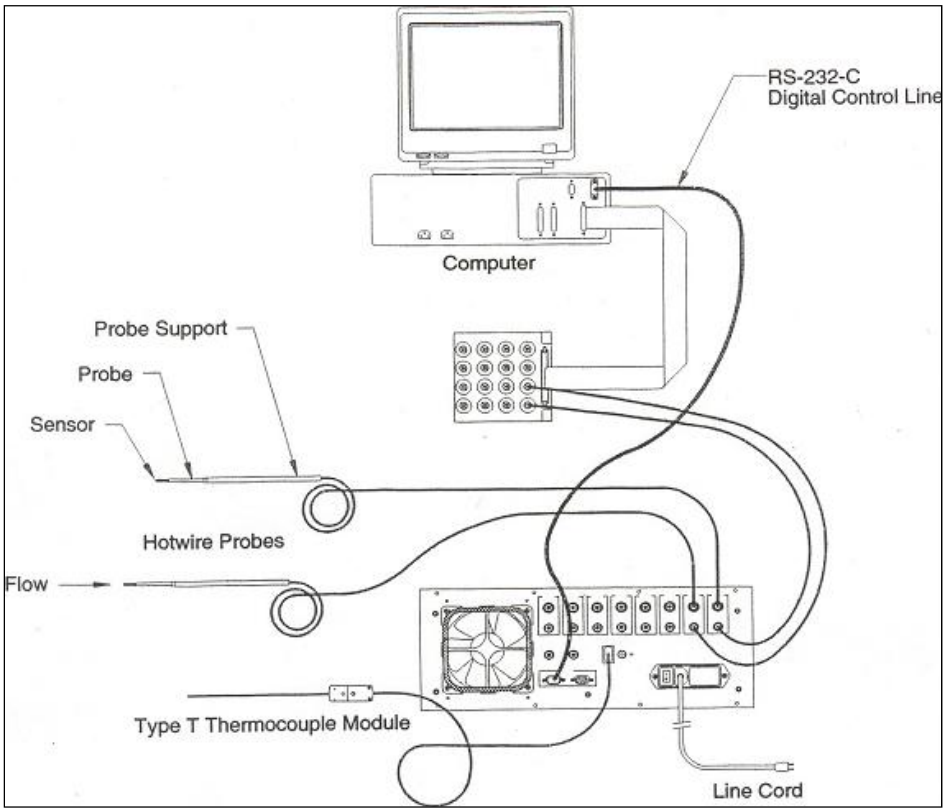

Figure 2.35 Overview of the IFA 300 hot-wire data acquisition system

2.3 Qualification Measurement

2.3.1 Uniformity of the Flow

To measure the uniformity of the flow from the wind tunnel, a measurement grid consisting of the grid size of 1″ x 1″ is created at the exit of the contraction nozzle. The velocity is measured at the nodes of the grid intersections as shown on the right hand side of Fig.2.36. The results in Fig.2.36 show that the flow is very uniform in the core region except in the thin boundary layers near the wall where the velocity is slower as expected. Fig.2.37 provides a more detailed view of the flow field in the core region by removing the boundary layers. The result shows that the flow is uniform within $\pm$1.16% in the core region.

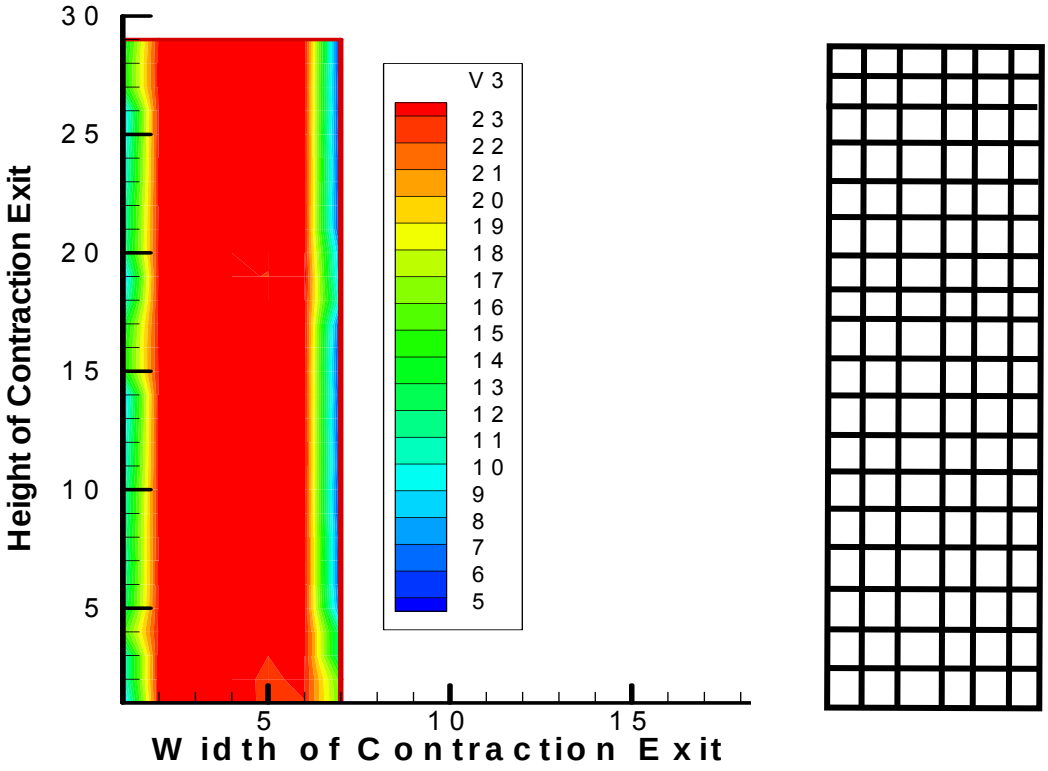

Figure 2.36 Velocity distributions (m/s) at the exit of the contraction

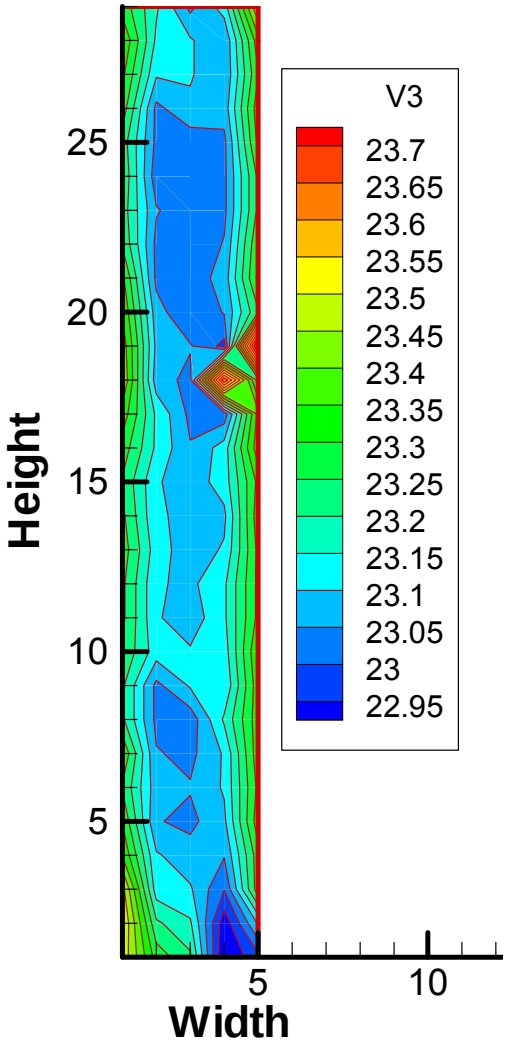

Figure 2.37 Velocity distributions (m/s) in the core region by removing the boundary layers at the exit of the contraction.

The qualification test shows the wind tunnel is successfully built to provide a uniform flow field. Further measurements will be conducted to measure the flow steadiness, temperature uniformity and steadiness, and turbulence structure at exit of the contraction.

2.4 Experiment Methodology

2.4.1 Velocity and Pressure Measurements

The pressure measurements procedure include setting the signal conditioners' zero and span adjustment, calibrating the pressure transducers, collecting static pressure measurements at various locations of the combustion chamber model and verifying the consistency of multiple data sets.

A pressure transducer converts a measured pressure into an analog electrical signal. Although there are various types of pressure transducers, one of the most common is the strain-gage base transducer. The conversion of pressure into an electrical signal is achieved by the physical deformation of strain gages that are bonded into the diaphragm of the pressure transducer and wired into a Wheatstone bridge configuration. Pressure applied to the pressure transducer produces a deflection of the diaphragm which introduces strain to the gages. The strain will produce an electrical resistance change proportional to the pressure. The electrical signal is then transferred to a signal conditioner.

Signal conditioners are the nucleus of any test measurement system. They receive output from the transducer, carry out basic processing of the signal, and pass the signal on to the display, storage, and analysis components. Signal conditioners may also supply an excitation voltage to power the transducer. In a typical measurement system, signal conditioning equipment is located between the transducer and the display. It conditions the transducer signal into a form the display can use. Some transducers have the signal conditioning electronics built into the body. This type of transducer can provide a high-level, low-impedance output signal that is immune to noise contamination caused by radio frequency interference or electromagnetic interference. The disadvantages include a limited temperature environment, resulting from the electronic

components and the large size of the transducer. Analog signal conditioners have been in use for decades. They are relatively simple in design employing a series of operational amplifiers for signal amplification. An analog signal conditioner's output is calibrated to a scale by adjusting zero and span potentiometers. These potentiometers can be interactive requiring repetitious calibration steps to obtain optimum scale accuracy. Analog signal conditioners are dependable devices with a low failure rate. Their operation is easily understood with little training required for their use. A drawback to analog signal conditioners is the intrinsic drift of potentiometers used for signal adjustment. This can lead to output drift over time. Potentiometers can also be awkward to adjust, complicating a calibration process.

A fluid flowing through a confined area exerts pressure consisting of two distinct components. These components are distinguished as the static pressure and the dynamic pressure. The static pressure does not cause any velocity change within the flow. The static pressure is usually measured by drilling a porthole through the container wall and connecting the porthole to a manometer. The drilled porthole must be perpendicular to the flow to ensure only the desired static pressure is attained. The dynamic pressure is due to the movement of the fluid. The static and dynamic pressures together make up the total or stagnation pressure. The stagnation pressure is measured by placing a pitot-static tube (Fig.2.38) directly parallel to the flow and connecting the pitot-static tube to a manometer.

A pitot-static tube (Fig.2.38) combines the static and stagnation pressure measurements into one device. It consists of a tube within a tube. The configuration is then placed in the duct facing upstream parallel to the flow of the fluid. The pressure tap facing upstream gives the stagnation pressure while the tap which is perpendicular to the flow gives the static pressure. When the pitot-static tube is in the fluid flow, the pressure difference between the stagnation and

static pressure can be measured using a manometer connected to each port. Applying Bernoulli's equation between the two pressure ports yields

$$\frac{p_{stg}g_c}{\rho_{air}g}+\frac{V_{stg}^2}{2g}+z_{stg}=\frac{p_{st}g_c}{\rho_{air}g}+\frac{V_{st}^2}{2g}+z_{st} \qquad \text{(Eq.2.1)}$$

p_x = pressure
g_c = gravitational constant
g = local gravity
V_x = velocity
ρ_x = density
z_x = elevation from datum

Where the subscripts "stg" represents the stagnation component and "st" represents the static component. The elevation difference between the stagnation and static port can be neglected. In addition, the velocity where the stagnation pressure is measured is zero. As a result Bernoulli's equation reduces to the following

$$\frac{p_{stg}g_c}{\rho_{air}}=\frac{p_{st}g_c}{\rho_{air}}+\frac{V_{st}^2}{2} \qquad \text{(Eq.2.2)}$$

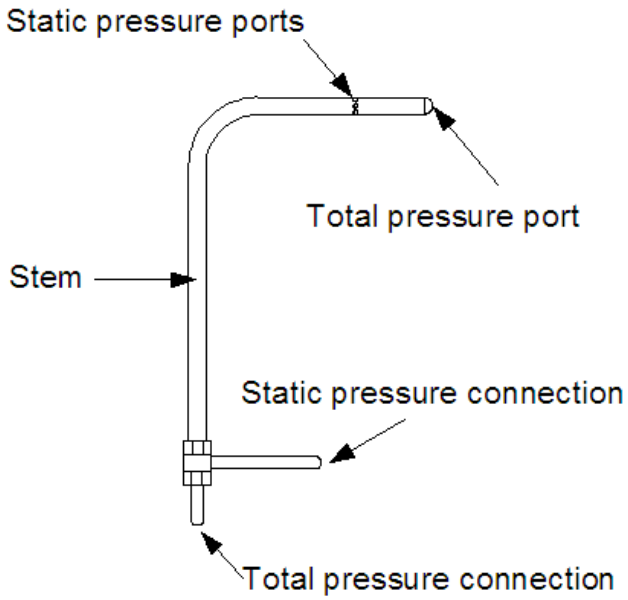

Figure 2.38 Pitot-static tube

After rearranging the following equation and solving for the velocity

$$V = \sqrt{\frac{2g_c}{\rho_{air}}\left(p_{stg} - p_{st}\right)} \qquad \text{(Eq.2.3)}$$

The subscript "st" was dropped to show the velocity at the static port is the same as the velocity of the airstream approaching the pitot-static tube. The gravitational constant is required if English units are being utilized, particularly if the unit of mass of the density is given in pound-mass (lbm). However, if SI units are being used the gravitational constant will be absent from the equation thereby reducing to

$$V = \sqrt{\frac{2\left(p_{stg} - p_{st}\right)}{\rho_{air}}} \qquad \text{(Eq.2.4)}$$

A manometer with the attached microtector (Fig. 2.39) connected to the pitot-static tube is used to acquire the pressure difference between the stagnation point and the static port by measuring the height of the water column.

Figure 2.39 Dwyer Model 1430 Microtector

By applying the hydrostatic equation the pressure difference is derived in the following manner

$$p_{stg} + \frac{\rho_{air} g}{g_c} x + \frac{\rho_{air} g}{g_c} \Delta h = p_{st} + \frac{\rho_{air} g}{g_c} x + \frac{\rho_{water} g}{g_c} \Delta h \qquad \text{(Eq.2.5)}$$

where Δh is the height of the water column. The vertical measurement x is measured from the centerline of the pitot-static tube to the immediate water interface in either leg of the manometer. For instance, if the manometer is located above the pitot-static tube, x is measured from the centerline to the lowest water interface. However, if the manometer is located above the pitot-static tube, x is measured from the centerline to the highest water interface. In either case, the terms containing x cancel which show that x is arbitrary. After the x terms cancel and rearrangement

$$\Delta P = p_{stg} - p_{st} = \Delta h(\rho_{water} - \rho_{air})g \qquad \text{(Eq.2.6)}$$

In the preceding equation $\rho_{water} \gg \rho_{air}$ therefore, ρ_{air} can be neglected thereby reducing to

$$\Delta P = p_{stg} - p_{st} = \Delta h \rho_{water} g \qquad \text{(Eq.2.7)}$$

2.4.2 Procedure for Adjusting Zero and Span of Signal Conditioners

1. Position Pitot-Static tube in the center of the transitional piece of combustor model.
2. Turn on computer, Voltage Regulator and Multiple Scanivavle System (MSS).
3. Open Scanivalve MSS Control Interface Program.
4. Choose the Module to be calibrated (**Module 1**) and select a channel which is opens to ambient pressure (**Channel 0**). “Channel open to ambient pressure” is any channels not connect to the combustor model.
    a. To toggle through Modules.
        - Use the mouse to highlight the Module field.

- Change the Module number 1-6 by pressing the desired number on the displayed number pad.

b. To toggle through Channels.

- Use the mouse to highlight the Channel field.
- Change the channel number 0-40 by pressing the “Step” button.
- Pressing the “Home” button returns the system to channel 0.

5. Setup Scanivalve MSS Control Interface Program.
    a. Refer to Appendix A for more detailed instructions.
    b. Select “Settings” of Display and check +/- 10V of Module to be calibrated.
    c. Select “Settings” of Scan and check only the channel that will be used during the calibration process. Uncheck any other channels not used during the calibration procedure. Be sure only one channel is selected.
6. Zero Signal Conditioner.
    a. Turn “Millivolt Input Range” knob of Signal Conditioner to lowest setting of 14-21.
    b. Observe voltage displayed on computer screen.
    c. Using a slotted screwdriver, adjust the “zero control” to display 0.000V on the screen by turning counter clockwise to reduce the voltage displayed and clockwise to increase the voltage displayed.
7. Record room conditions: Pressure, Temperature and Humidity.
8. Adjust Span of Signal Conditioner.

a. Connect the stagnation port of Pitot-Static tube to any channel of the Module to be calibrated, preferably the previous selected channel that opens to the ambient pressure.
b. If an alternate channel is selected be sure to also select the corresponding channel in the Scanivalve MSS Control Interface Program.
c. Leave the static port of the Pitot-Static tube open to the surroundings, preferably place static port in close proximity to the static port of transducer being calibrated.
d. Turn the wind tunnel "**On**" to its maximum level of 60Hz.
e. Observe voltage displayed on computer screen.
f. Using a slotted screwdriver, adjust the "span control" to display 5.000V on the screen by turning counter clockwise to reduce the voltage displayed and clockwise to increase the voltage displayed.

During the experiments, the measured data may migrate due to uncontrollable conditions. Therefore, it was necessary to record multiple readings and average them to attain an averaged value. By checking the "Scan and Save Data" field and pressing the "Start" button the displayed values were recorded to a text file. The data in the text file was later imported to Excel. In Excel statistical methods were employed to attain the approximate output voltage of the transducer.

2.4.3 Procedure for Calibrating Pressure Transducer

1. Position Pitot-Static tube in the center of the transitional piece of combustor model.
2. Position Manometer on a steady flat surface.
3. Zero-set the manometer

a. Use the leveling knobs of the manometer base to level the manometer.

b. Turn on the ammeter.

c. Set the micrometer to read 0mm at a reading of 25μA of the ammeter.

- Turn micrometer to 0mm.
- Adjust needle within micrometer by loosening locknut and turning needle counterclockwise to lower and clockwise to raise (view looking downward).
- Continue adjusting needle until 25μA is read from the ammeter.
- Tighten locknut.
- Check that manometer is leveled, micrometer reads 0mm and ammeter reads 25μA. Repeat step 3 as needed.

4. Turn on computer, Voltage Regulator and Multiple Scanivavle System (MSS).
5. Open Scanivalve MSS Control Interface Program.
6. Choose the Module to be calibrated (**Module 1**) and select a channel which is open to ambient pressure (**Channel 0**). "Channel open to ambient pressure" is any channels not connect to the combustor model.

a. To toggle through Modules.

- Use the mouse to highlight the Module field.
- Change the Module number 1-6 by pressing the desired number on the displayed number pad.

b. To toggle through Channels.

- Use the mouse to highlight the Channel field.
- Change the channel number 0-40 by pressing the "Step" button.

- Pressing the “Home” button returns the system to channel 0.

7. Setup Scanivalve MSS Control Interface Program.
    a. Refer to Appendix A for more detailed instructions.
    b. Select “Settings” of Display and check +/- 10V of Module to be calibrated.
    c. Select “Settings” of Scan and check only the channel which will be used during the calibration process. Uncheck any other channels not used during the calibration procedure. Be sure only one channel is selected.
8. Record room conditions: Pressure, Temperature and Humidity.
9. Record the voltage offset: The voltage displayed on the screen.
10. Turn the wind tunnel “**On**” to level of 10Hz.
11. Connect the stagnation port of the Pitot-Static tube to channel selected in step 6.
12. Leave the static port of the Pitot-Static tube open to the surroundings, preferably place static port in close proximity to the static port of transducer being calibrated.
13. Observe voltage displayed on computer screen. The voltage should increase if it does not increase check all connections. Also, check that the correct Module and Channel is selected in the Scanivalve MSS Controller Interface program.
14. Record voltage every second for a period of 30 seconds.
    a. In the Scanivalve MSS Controller Interface program check the field labeled “Scan and Save Data.”
    b. Press the “Start” button.
    c. Wait 30 seconds.
    d. Press the “Stop” button.
15. Disconnect Pitot-Static stagnation port from MSS channel.

16. Connect Pitot-Static stagnation port to High pressure port of manometer.
17. Leave Low pressure port of manometer open to surroundings, preferably place Low pressure port in close proximity to the static port of transducer being calibrated.
18. Adjust micrometer until the ammeter reads 25μA.
19. Record manometer measurement.
20. Disconnect Pitot - static tube from manometer.
21. Increase frequency of wind tunnel blower by 10Hz.
22. Repeat steps 11-21 until frequency of 60Hz is reached.

The room conditions changed throughout the experiment. Although it was not added to the procedures, the room conditions were recorded immediately after recording the manometer measurement. The variation in temperature, humidity and pressure of the room were insignificant and therefore not used to calibrate the pressure transducer. The temperature, humidity and pressure initially recorded in step 8 were used as the reference point.

When adjusting the microtector of the manometer it became apparent that it is beneficial to repeat a systematic method of measuring the water column. Sometimes the ammeter read beyond the limit of 50μA. In an attempt to maintain consistency in measurements, the needle of the microtector was backed out of the water column then reinserted each time this occurred. In addition, when measuring the water column of the manometer allow adequate time for the needle of the ammeter to steady. The manometer is very sensitive to changes of the water column height. The needle of the ammeter may seem to be steady on 25μA: however if not careful the needle will slowly move to a lesser or higher value. Therefore it is critical to allow ample time for the water column to settle in order to attain an accurate measurement.

In the theory section the term Δh represents horizontal different height of the water column. Also to reduce the error in measurement the height of the water column should be measured several times. The average of these readings is the pressure applied to the gage. The degree of uncertainty for the operator is indicated by the difference in these readings. When the readings are complete, the pressure should be removed and the zero setting of manometer rechecked. Any change in the zero position will indicate inaccurate readings. Should this happen, the zero-set and pressure measurement procedure should be repeated.

2.4.4 Procedure for Temperature Measurement

1. Turn on the wind tunnel, and slowly increase its speed to the highest.
2. Turn on the heat gun and observe the temperature variation inside the combustor chamber till it reaches a steady state within ±0.1C in one hour. (Usually it takes 3 hours to achieve steady state.)
3. Open the **ExceLINX**, and set up the configuration of the scanning.
4. Click "Start" in **ExceLINX** to begin scanning.
5. Repeat **step 4** till designated number of times scanning achieved, and each scanning should has some interval time (10 minutes at least is suggested).
6. Save the data into a excel file.

To make sure the measurement data is taken at a comparable steady state condition, repeatable measurements were taken. Since one scanning time takes approximate 30 seconds, the room temperature changes within this time frame is negligible(less than 1°C different in an hour) The data taken before the steady state is reached are not used for data analysis, but they are kept reference to observe the tendency of data changes. Here, the customize criteria of repeatability is

applied. The step by step description of how to use **ExceLINX** to collect the data is list in **Appendix E.**

CHAPTER THREE

EXPERIMENTAL RESULTS AND DISCUSSIONS

3.1 The Laboratory Condition

The ambient conditions (atmospheric pressure, humidity, and room temperature) are monitored during each experiment including the calibration tests. For a short experiment, the initial and final temperatures are recorded. For a long experiment, several intermediate readings of ambient conditions are recorded. Table 3.1 shows typical recorded room conditions before and after the experiment. It is important to monitor the change of ambient conditions to assess their unsteadiness for uncertainty analysis. The offset voltage represents the bias of a pressure transducer reading at zero pressure and it is obtained by connecting the transducers low pressure port to its high pressure port. Since the offset voltage of a pressure transducer is sensitive to room temperature, the value of each pressure transducer's offset voltage is also shown in Table 3.2. Although there are changes in temperature, humidity, and pressure of flow during each experiment, since the changes are minimal under current the study, they are treated as uncertainties by keeping the ambient conditions constant, such as the values shown in Table 3.2 for a representative experimental case.

Table 3.1 A representative initial and final conditions of room and transducers' offset voltages during one experiment

	Initial	Final
Temperature [°F]	77.3	78.6
Humidity [%]	51.5	52.7
Pressure [inHg]	30	29.985
V1 offset [volts]	0	-0.005
V2 offset [volts]	0.003	0.005
V3 offset [volts]	0.005	0.005
V4 offset [volts]	0.006	0.006
V5 offset [volts]	0.003	0.006
V6 offset [volts]	0.006	0.006
Manometer [mm]	0	0

Table 3.2 Representative values of water density and gravity used during analysis

Water Density [kg/m3]	998.2
Air Density [kg/m3]	1.28
Gravity [m/s2]	9.81

3.2 Calibration

Calibration is a validation of accuracy of a specific measurement technique via a piece of equipment against a standard. For this experiment, digital voltage readings from the Scanivalve system are calibrated against the water columns measured at different wind speeds as described in Chapter 2.

The speed of the wind tunnel is controlled by the frequency controller. The motor speed increases as the frequency increases. The height of the water column is measured from the manometer with the attached micrometer which can detect the water column height within 0.01mm. The voltage outputs of the transducers are recorded from the Scanivalve Software Interface. After measuring the height of the water column Eq.2.7 is used to calculate the

differential pressure and Eq.2.4 is used to calculate the air velocity in the rectangular-to-circular transition section, as shown in Table 3.3. A pressure versus voltage calibration curve can be obtained for each pressure transducer.

Table 3.3 Inlet airstream velocity in the transition section upstream of the test section at different wind speeds

Frequence (HZ)	ΔH (inch)	ΔH (m)	ΔP (Pa)	Velocity (m/s)
5	0.02	0.00	4.97	2.88
10	0.08	0.00	19.87	5.76
15	0.16	0.00	39.75	8.14
20	0.24	0.01	59.62	9.97
25	0.36	0.01	89.43	12.21
30	0.54	0.01	134.15	14.95
35	0.72	0.02	178.87	17.27
40	0.92	0.02	228.55	19.52
45	1.20	0.03	298.11	22.29
50	1.50	0.04	372.64	24.92
55	1.82	0.05	452.14	27.45
60	2.16	0.05	536.60	29.91

There are six pressure transducers. All of them are of the same model and were purchased at one batch, so it is interesting to know if all of them have a similar calibration curve. Table 3.4 shows that the calibration data of each module and Fig.3.1 shows the calibration curve (actually a liner line) of all six transducers. It can be seen that these six lines are sufficiently close, so a single averaged pressure-voltage calibration curve has been used for all modules in Fig. 3.2. The minor deviations from the averaged calibration line are included in the uncertainty analysis as the bias of calibration.

Table 3.4 Readings of water column heights, voltages of 6 transducers and differential pressures at various wind speeds

Frequence (Hz)	Module C1 (V)	Module F2 (V)	Module B3 (V)	Module E4 (V)	Module A5 (V)	Module D6 (V)	Average (V)	Δ P (Pa)	Δh (water in)
10	0.14	0.14	0.14	0.14	0.14	0.14	0.14	57.07	0.23
20	0.61	0.60	0.61	0.60	0.60	0.60	0.60	275.75	1.11
30	1.39	1.37	1.39	1.37	1.38	1.37	1.38	573.70	2.31
40	2.49	2.45	2.49	2.45	2.46	2.45	2.46	1030.60	4.15
50	3.91	3.82	3.88	3.83	3.87	3.85	3.86	1576.92	6.35
60	5.61	5.46	5.56	5.47	5.52	5.52	5.52	2297.27	9.25

After calibrating the modules, the combustor chamber pressure measurements were able to be performed. As always before starting any pressure measurements the room conditions have to be recorded. Table 3.5 shows the room conditions before and after the combustor chamber pressure measurements were taken for sheathed case.

Table 3.5 Room conditions before and after Combustor pressure measurements for the sheathed case

	Initial	**Final**
Temperature [°F]	77.3	78.6
Humidity [%]	51.5	52.7
Pressure [inHg]	30	29.985
V1 offset [volts]	0	-0.005
V2 offset [volts]	0.003	0.005
V3 offset [volts]	0.005	0.006
V4 offset [volts]	0.006	0.007
V5 offset [volts]	0.003	0.004
V6 offset [volts]	0.006	0.008
Manometer [mm]	0	0

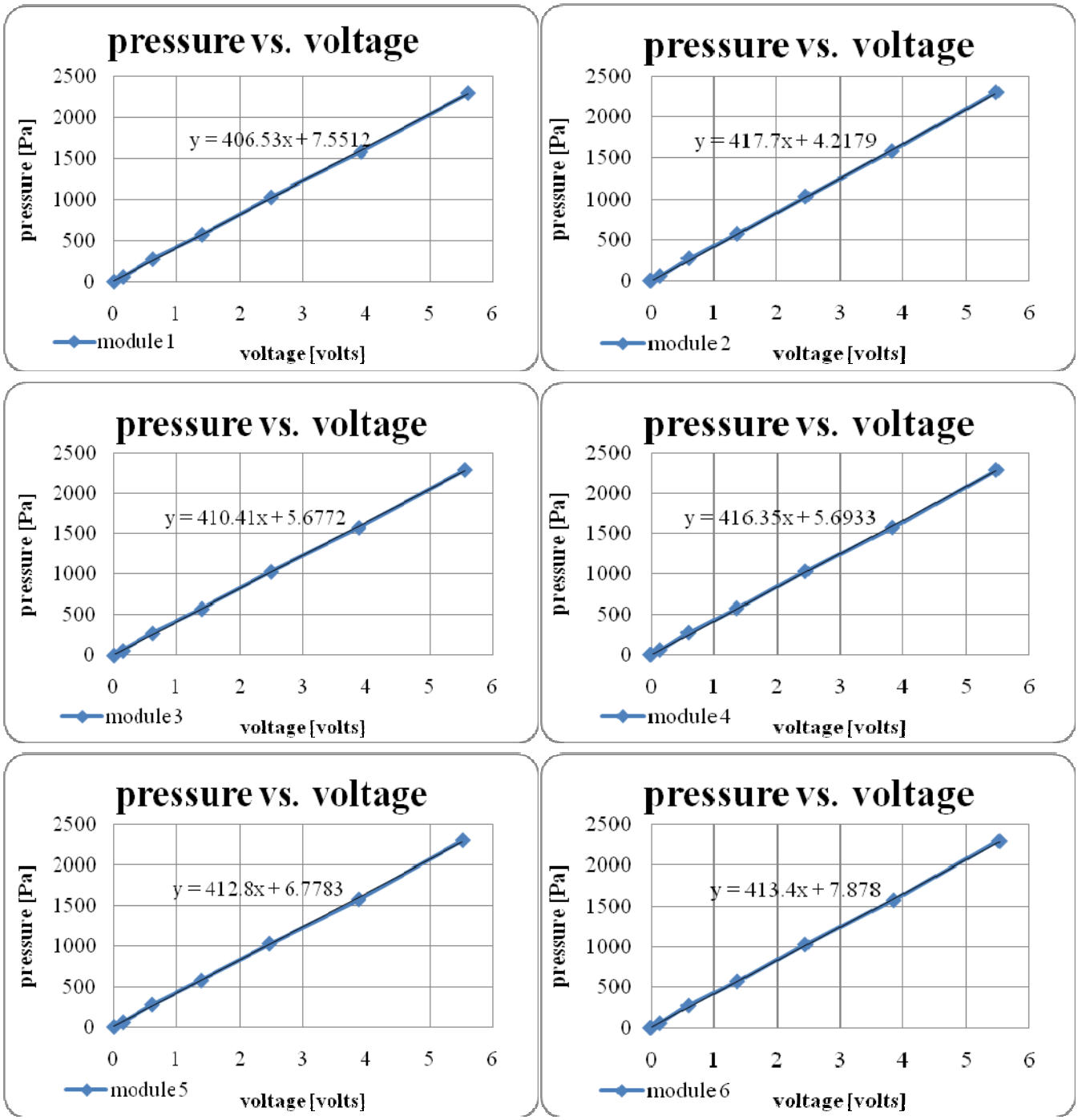

Figure 3.1 Calibration curves (pressure vs. voltage) of six pressure transducers

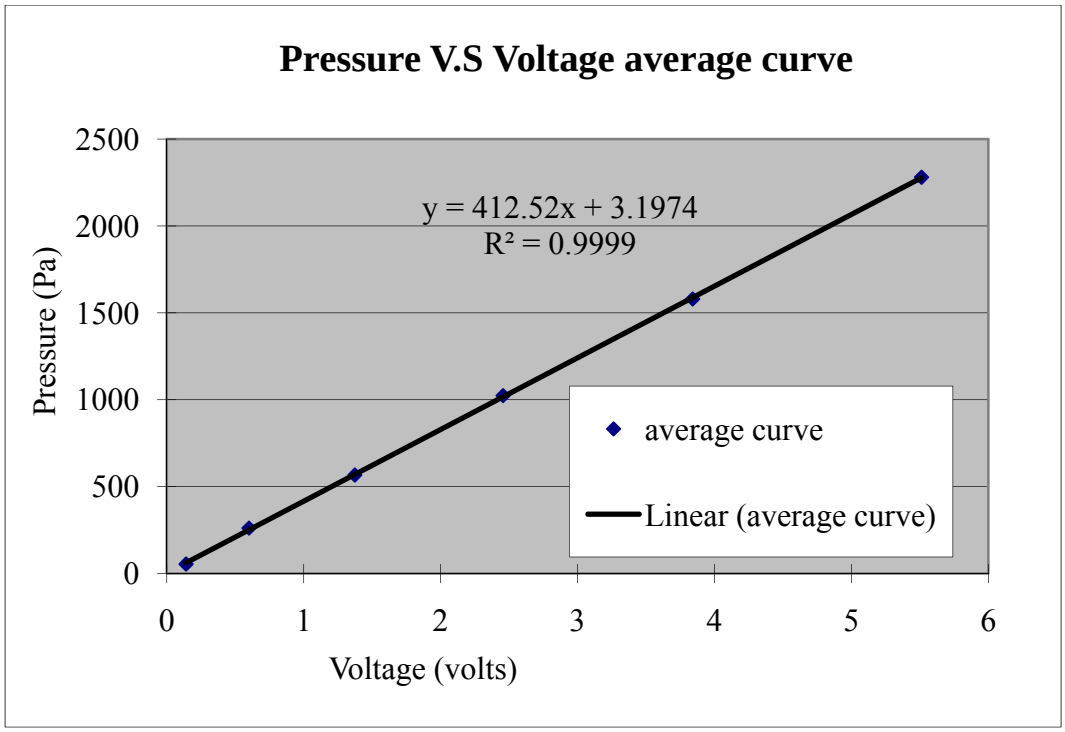

Figure 3.2 The averaged calibration line for all 6 transducer

3.3 Cold-Flow Pressure Measurement Results

Each case measurement was taken 5 times in 30-minute intervals. The average of these 5 measurements is shown in the following figures. The results of sheathed and no-sheath cases are compared in Fig.3.3 for the same speed (60HZ). Removing the sheath recover most of pressure losses. The local static pressure difference does not represent the pressure recovery because the flow pattern and flow direction change. Some areas are subject to flow impingement with increased pressure when the sheath is removed, while some other areas may be located in a wake flow showing a drop of static pressure. The pressure recovery with the removal of the sheath can be approximately obtained by measuring the total pressure losses between the inlet and outlet of the test section or indirectly derived from the increased flow rate. The sheathed case has the

static gauge pressure of around 1000 Pascal (0.145 psia) level while the no-sheath case has the static gauge pressure of around 2000 Pascal (0.29 psia) level at the same pressure tap location.

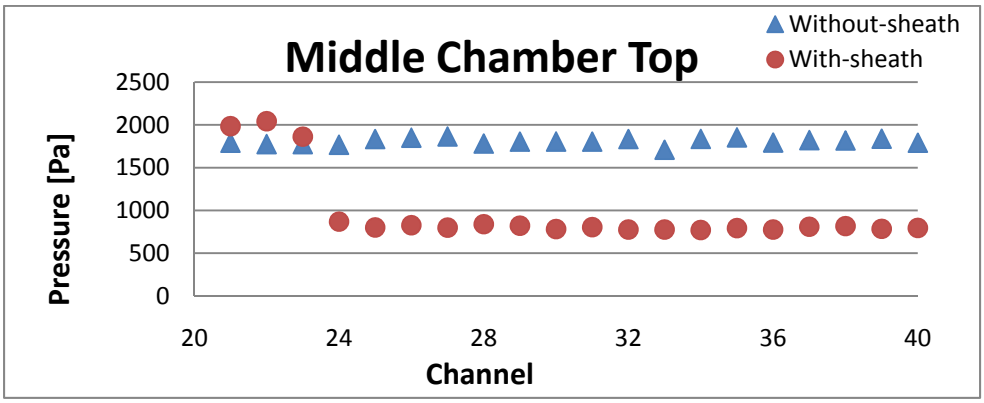

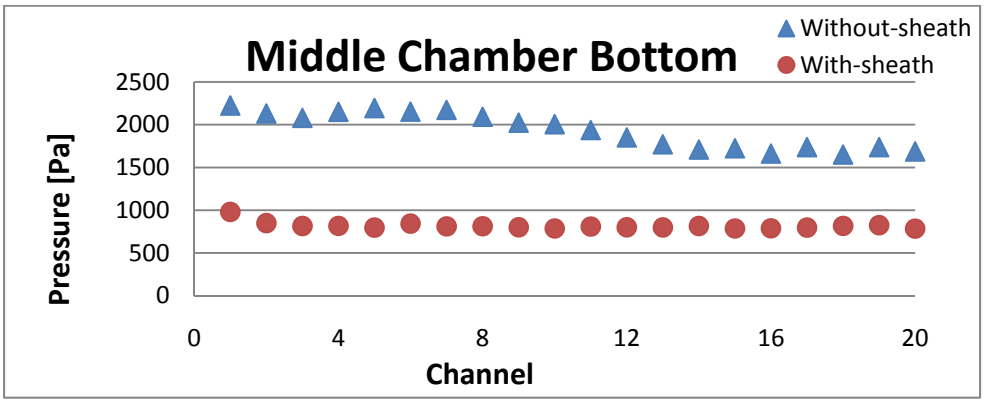

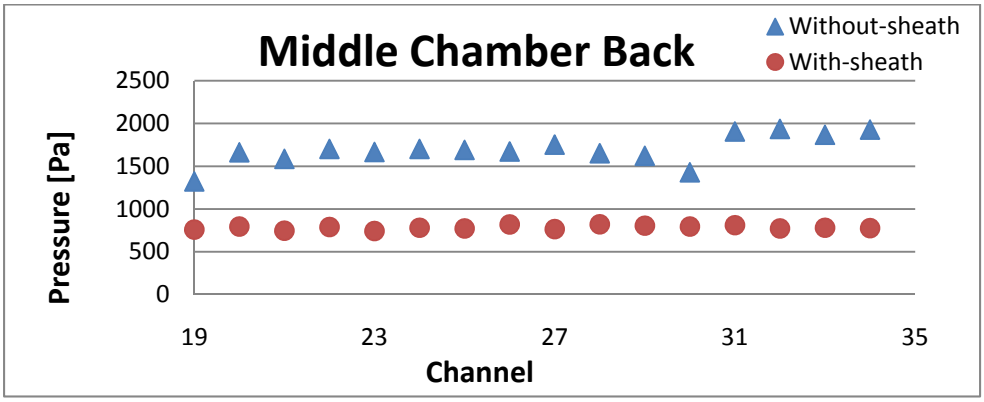

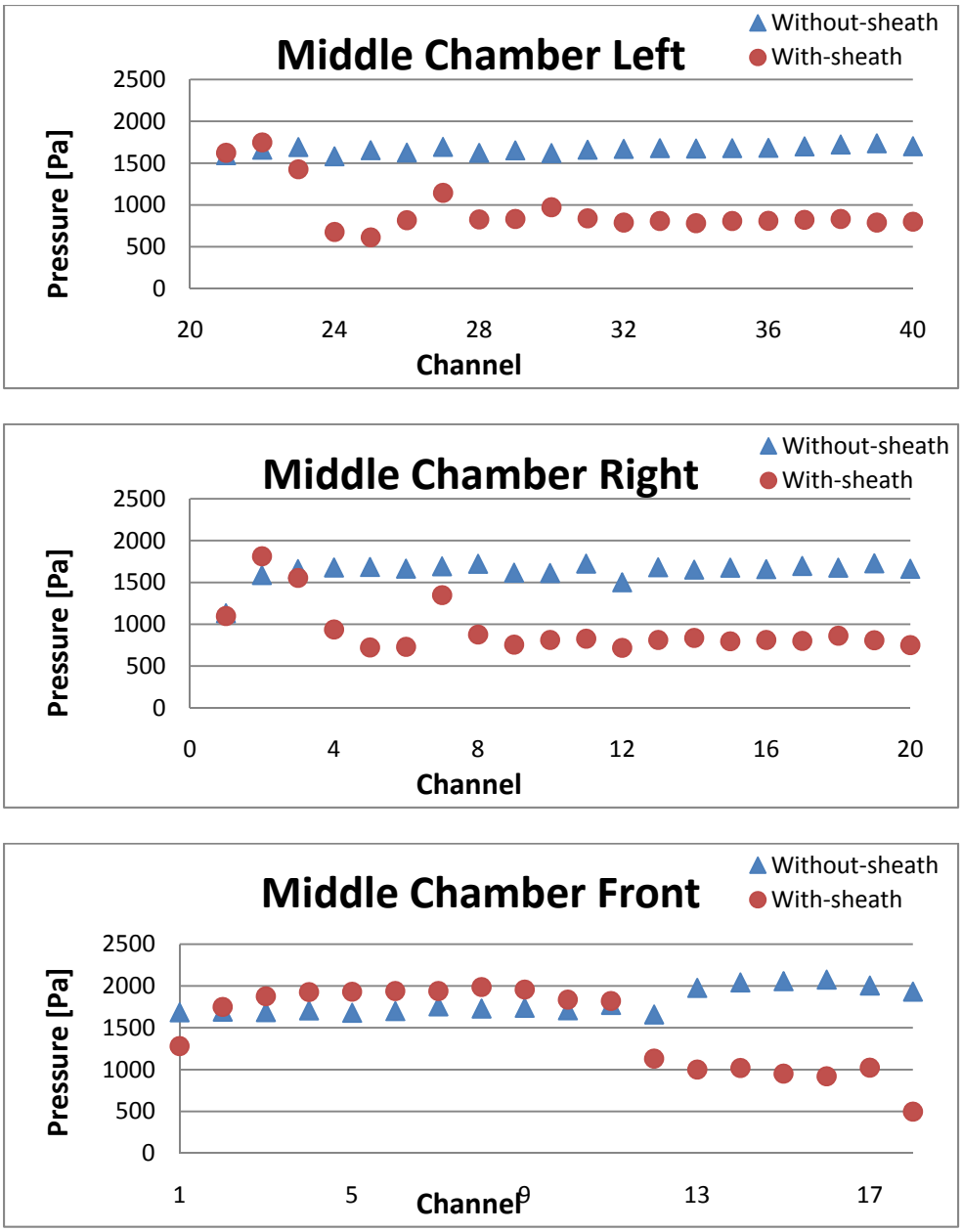

Figure 3.3 Comparison of pressure distribution on the combustor and transition walls between sheathed and no-sheath cases

3.4 Uncertainty Analysis of Pressure Measurements

An experiment designed to determine an effect, demonstrate a law, or estimate the numerical value of a physical variable will be affected by errors due to instrumentation, methodology, presence of confounding effects and so on. Experimental uncertainty estimates are needed to assess the confidence in the results. The expected resultant of this experiment is an array of pressure measurement values, one for each pressure tap location. Equipment used in this experiment is list in the Table 3.6. The pressure is computed from the measured data as

$$p = \Delta h * \left(\rho_{water} - \rho_{humid\,air}\right) g \qquad \text{(Eq.3.1)}$$

The variables ρ_{water} and $\rho_{humid\,air}$ in the preceding equation are dependent variables, which are the resultants of other measurements. For these dependant variables, a procedure of backward "tracing" was taken until the root was found. A simplified block diagram (Fig.3.4.) illustrates the tracking of each variable. The number of possible independent variable has not been exhausted.

Using Eq.3.1 to calculate density of humid air,

$$\rho_{humid\,air} = \frac{p_d}{R_d * T} + \frac{p_v}{R_v * T} \qquad \text{(Eq.3.2)}$$

Where: $\rho_{humid\,air}$ = Density of the humid air (kg/m³)

p_d = Partial pressure of dry air (Pa)

R_d = Specific gas constant for dry air, 287.05 J/(kg·K)

T = Temperature (K)

p_v = Pressure of water vapor (Pa)

R_v = Specific gas constant for water vapor, 461.495 J/(kg·K)

The pressure of water vapor may be calculated from the saturation vapor pressure and relative humidity. It is found by Eq.3.2

$$p_v = \phi * p_{sat} \quad \text{(Eq.3.3)}$$

Where: $\phi =$ Relative humidity and $p_{sat} =$ Saturation vapor pressure

The saturation vapor pressure of water at any given temperature is the vapor pressure when relative humidity is 100%. A simplification of the regression used to find this, can be formulated as Eq.3.3

$$p_{sat} = 6.1078 \times 10^{\frac{7.5T - 2048.625}{T - 35.85}} \quad \text{(Eq.3.4)}$$

Notes:

- This will give a result in mbar (millibar), 1 mbar = 0.001 bar = 0.1 kPa = 100 Pa
- p_d is found considering partial pressure, resulting in:

$$p_d = p - p_v \quad \text{(Eq.3.5)}$$

Where p simply denotes the absolute pressure in the observed system

The results of the uncertainty analysis vary with the stage of evolution of the analysis or with the level of replication on which the analysis is based. The method used in this analysis is Moffat (1982) and Wang and Simon (1988).

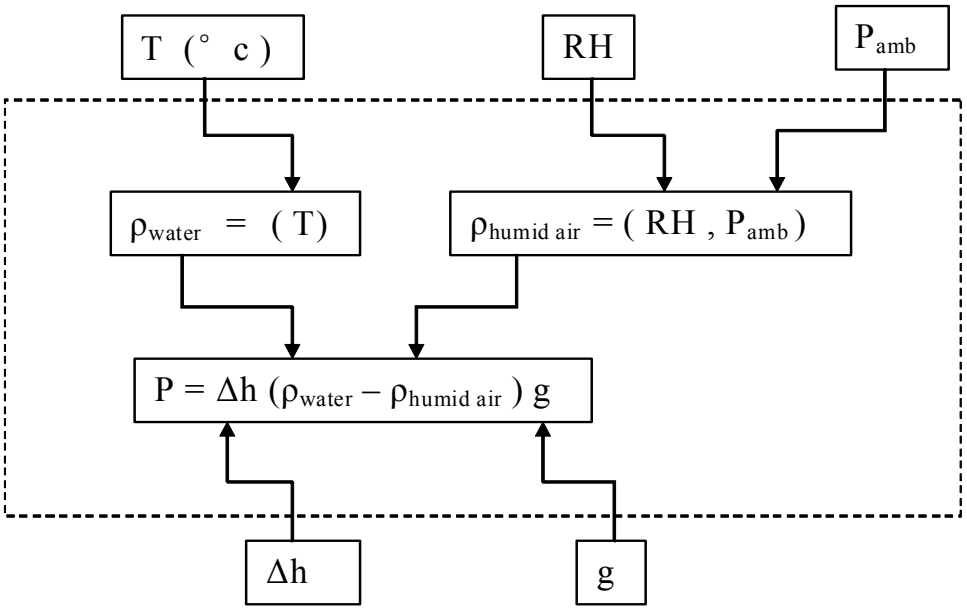

Figure 3.4 A block diagram illustrates the backward tracing procedure for identifying the primary measurands. The variables located outside the dashed box are primary measurands

Table 3.6 Equipments' specification list for pressure measurement

Equipemt	Brand&Manufactor	Reading Rang	Accuracy
Manometer	OMEHA Model HHP-2000	Pressure	0.1% Reading ±0.1% FS
Thermometer	EXTECH Model RH401	Temperature 0 ~122 F	±1.8F
Thermometer	EXTECH Model RH401	Humidity 0.0 to 100.0% RH	±3% RH
Pressure Transducer	Setra System Model 264		±1.0% FS
Signal Conditioner	SCSG		0.002% FS

Because of the uncertainty of instrument imprecision, Zeroth-Order Analysis was made in the early stages of the test program design, made by the uncertainty of instrument imprecision.

The Zeroth-Order uncertainty results were used to assist in selecting the instruments, which was based on precision error only.

$$\delta X_R = \left\{ \sum_i \left[\left(\frac{\partial X_R}{\partial X_i} \right) \delta X_i \right]^2 \right\}^{\frac{1}{2}} \quad \text{(Eq.3.6)}$$

Pretest Analysis added an uncertainty associated with the calibration of the system to the uncertainty associated with instrument imprecision.

$$\delta X_{i,p} = \left[\left(\delta X_{i,o} \right)^2 + \left(\delta X_{i,c} \right)^2 \right]^{\frac{1}{2}} \quad \text{(Eq.3.7)}$$

First-Order Analysis further added the uncertainty associated with unsteadiness of the system to the uncertainty associated with instrument imprecision.

$$\delta X_{i,1} = \left[\left(\delta X_{i,o} \right)^2 + \left(\delta X_{i,u} \right)^2 \right]^{\frac{1}{2}} \quad \text{(Eq.3.8)}$$

Nth-Order Analysis include uncertainties caused by imprecision, unsteadiness, calibration error and errors in the correction models incorporated to minimize all known bias errors.

$$\delta X_{i,p} = \left[\left(\delta X_{i,o} \right)^2 + \left(\delta X_{i,c} \right)^2 + \left(\delta X_{i,u} \right)^2 \right]^{\frac{1}{2}} \quad \text{(Eq.3.9)}$$

Finally, Table 3.7 shows the total uncertainty analysis for this pressure measurement experiment.

Table 3.7 Input data and results for zeroth, pretest and first uncertainty analysis

Independent variable	Instrument	Nominal value	Uncertainty of imprecission	Uncertainty of unsteadiness	Uncertainty of calibration	Zeroth order (%)	Pretest (%)	First order (%)	Nth order (%)
P , V/m-H_2O	pressure tansducer	2	0	0.05	0.02	0	1	2.693	3.978
V_L, , V	signal conditioner	10	0.0002	0	0	0.002	0.002	0.002	0.002
Tamb , °C	thermometer	25	0.3	0.1	0	0.0075	0.0075	0.008	0.008
ΔH_{water} , cm	manometer	20	0.03	0.1	0	0.15	0.15	0.522	0.522
RH , %	thermometer	60	6	3	0	0.0001	0.0001	0.0001	0.0001
Pamb , pascal	digital manometer	101325	100	50	0	0.0002	0.0002	0.0002	0.0002
total						0.151	1.011	2.743	4.511

3.4 Temperature Measurement Results

It is important to record room conditions during the experiment. Table 3.8 shows the room conditions before and after temperature measurement

Table 3.8 A representative room conditions before and after temperature measurement

	Initial	*Final*
Temperature [°C]	18.7	23.9
Pressure [Kpa]	101.9	101.9
Humidity [%]	50.9	40.2

Figure 3.5 reflects the comparison of temperature measurement results between no-sheath and sheathed case. The temperature measurements of the no-sheath case are always about 2~5 K (3.6~9°F) higher than the corresponding measurements of the sheathed case. The sheath does help to increase the cooling effect. The biggest temperature difference happened at the top-left of the mid-chamber, which is about 8 K (13°F), and indicates 2.5% extra cooling with sheath employed.

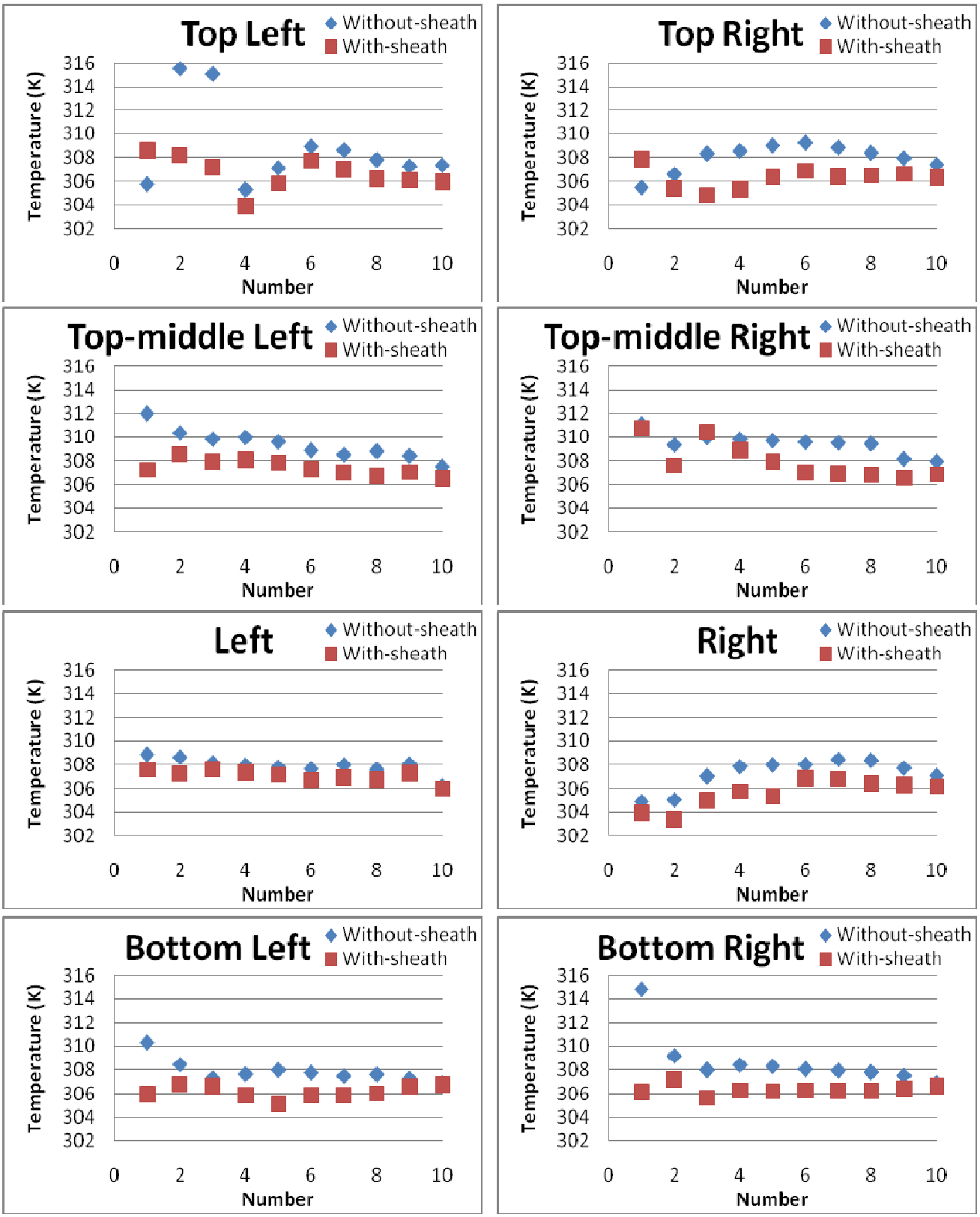

Figure 3.5 Temperature comparisons between no-sheath and sheathed cases

CHAPTER FOUR

COMPUTATIONAL MODEL

4.1 Modeling Information

In addition to the experiment, simulation using computational fluid dynamics (CFD) is conducted. The purpose of conducting CFD analysis is to use the experimental data to verify the computational model and further use the validated model to simulate conditions under real gas turbine operating conditions. For the verification cases, the geometry of the computational domain and the boundary conditions are built with one full combustor and two adjacent half combustors based on a periodic sector of 1/7th of the complete reverse-flow combustor system (Fig. 4.1a). Their boundary conditions are set exactly as the test conditions described in Chapter 2. For the cases simulating a real gas turbine operating condition, the computational configuration is built with one full combustor in a periodic section of 1/14th of the complete system (Fig. 4.1b).

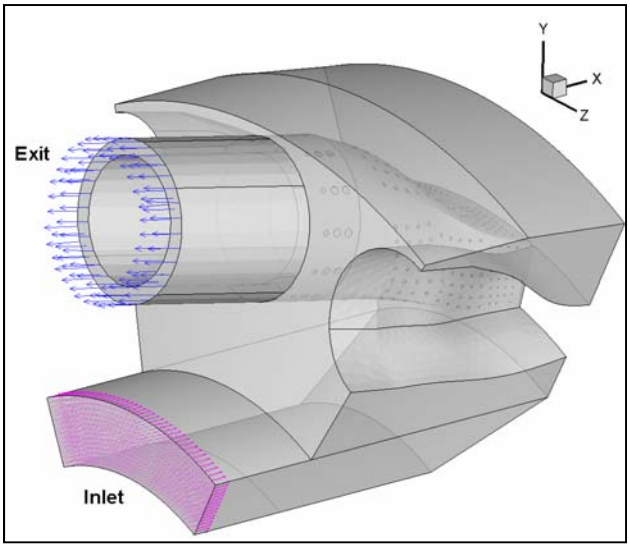

(a)

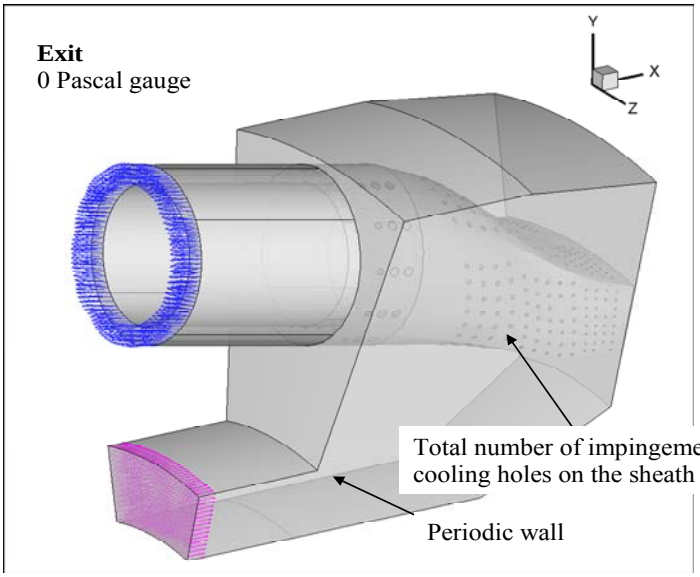

Inlet
Mass flow rate: 32 kg/s
Temperature: 700K

- Operating pressure 16 atm.
- No slip condition at the wall.
  u = 0, v = 0, w = 0
- Constant heat flux 310000W/m^2 at the
  mid-chamber and transitional piece
- Inlet turbulence intensity: 1%

(b)

Figure 4.1 (a) Computational configuration of sheathed case based on experimental test conditions with one full combustor and two adjacent half combustors in a periodic 1/7th sector of the complete system (b) Computational configuration of sheathed case for real gas turbine operating condition with one full combustor in a periodic 1/14th sector of the complete system

4.2 Meshes

The mesh used in this study is generated using GAMBIT (version 2.4.6). Unstructured T-grids are used in meshing the whole domain for this complicated geometry. All together there are 207,215 nodes, 1,990,756 faces and 948,940 cells for no-sheath case; for the sheathed case, there are 2,527,520 nodes, 2,527,520 faces and 1,206,030 cells. Meshes of each part for the sheathed case are shown in detail in Fig.4.2.

During the meshing process, special effort has been expended to mesh hundred of small impinging holes. Two different methods have been used. One method sets the hole as an interior surface with at least ten nodes and cells on it as shown in Fig.3.4a. Another leaves the holes as part of interior volume with denser cells being meshed surrounding the holes as shown in Fig.4.3b. The first method needs more work and computational time because of the larger number of mesh sizes, while the second method can save more than 30% of computational time. It was initially thought that the first method would produce a better result because the flow is expected to drastically accelerate at the impinging holes interface. However, comparison of these two methods shows the difference is less than 1%. Considering the minimal benefits that can be obtained by the first method, the second method is therefore selected for this project.

During the computational iteration process, occasionally very high or low, velocity, pressures, and temperature could occur and the computation will be interrupted. To avoid this situation, realistic values of upper and lower bounds of velocity, pressure, and temperature are imposed. Building an appropriate computational grid is essential for achieving computation convergence in this study. Due to the many small impinging holes in this study, quite a bit of time has been spent building and continuously improving the quality of successful computational grids.

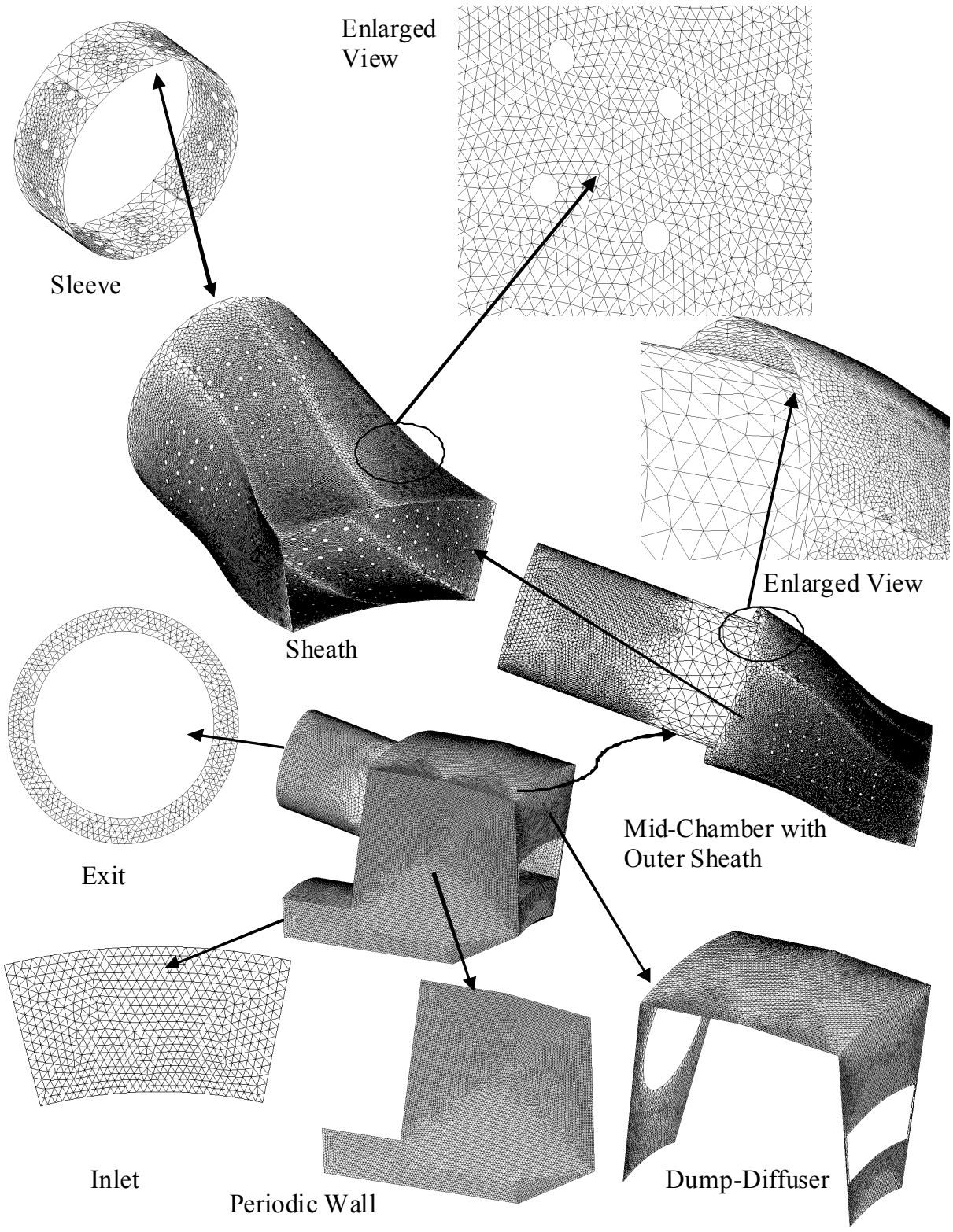

Figure 4.2 Meshes of different parts of the reverse-flow combustor

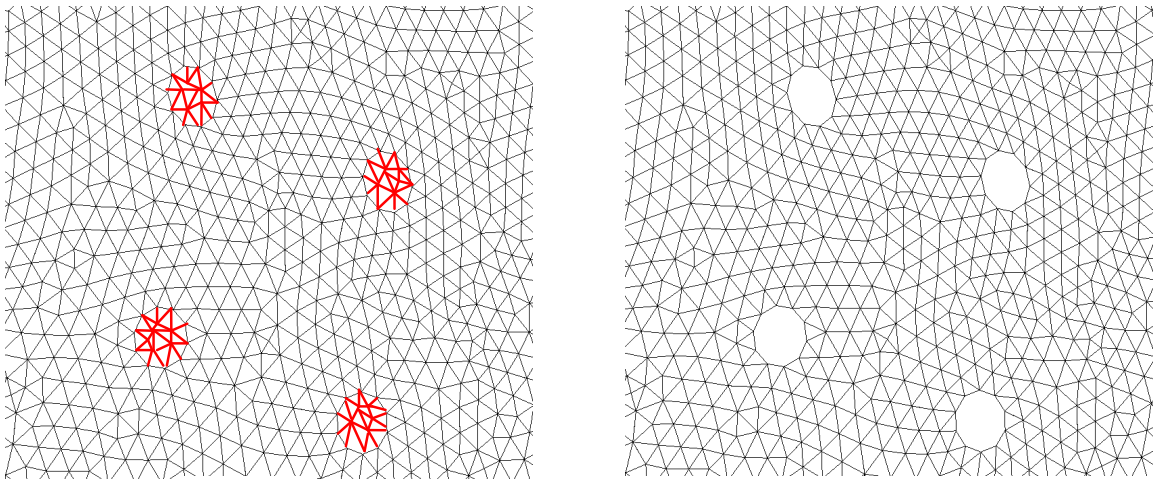

Figure 4.3 (a) First method: the impinging holes are set us interior surfaces with zero thickness (b) Second method: the impinging holes set as part of interior volume

4.2.1 Grid Sensitivity Study

A grid sensitivity study of two different mesh numbers (about 1.2 million cells and 2.5 million cells) of the same case (sheathed case) have been performed and investigated. The computational time for the low mesh number case is about 60 hours and for the high mesh number case is about 200 hours of physical clock time run through a cluster of 16 parallel processors. The temperature variation within the whole domain between these two mesh numbers lies within 17k to 25k (4.8%-7.1%), based on the maximum wall temperature T_{max}=350K. At the exit, the difference of mass weighted temperature is about 1.1k (0.39%). Although the grid independence has not been achieved, for the purpose of the current study, 8% of computational uncertainty is acceptable. Therefore the mesh number of around 1.2 million is used for this study, which saves more than 70% of the computational time.

4.3 Physical Characteristics of the Problem and Assumptions

The physical characteristics of the problem are as follow:

1. Steady state, three-dimensional.
2. Newtonian fluids with variable properties as function of temperature and pressure.
3. Compressible flow.
4. No-slip condition (zero velocity) is imposed on wall surfaces.
5. Periodic boundary condition is used.

4.4 Governing Equations

The equations for conservation of mass, conservation of momentum, and energy equation are given as:

$$\nabla \cdot (\rho \vec{v}) = S_m \tag{4.1}$$

$$\nabla \cdot (\rho \vec{v}\vec{v}) = -\nabla p + \nabla \cdot \left(\bar{\bar{\tau}} \right) + \rho \vec{g} + \vec{F} \tag{4.2}$$

$$\nabla \cdot (\vec{v}(\rho E + p)) = \nabla \cdot \left(\lambda_{eff} \nabla T - \sum_j h_j \vec{J}_j + \left(\bar{\bar{\tau}}_{eff} \cdot \vec{v} \right) \right) \tag{4.3}$$

where λ_{eff} is the effective conductivity ($\lambda+\lambda_t$, where λ_t is the turbulence conductivity) and J_j is the diffusion of species j.

The stress tensor $\bar{\bar{\tau}}$ is given by

$$\bar{\bar{\tau}} = \mu \left[\left(\nabla \vec{v} + \nabla \vec{v}^T \right) - \frac{2}{3} \nabla \cdot \vec{v} I \right]. \tag{4.4}$$

where μ is the molecular dynamic viscosity, I is the unit tensor, and the second term on the right-hand side is the effect of volume dilatation. The three terms on the right-hand side of the equation (4.3) represent heat transfer due to conduction, species diffusion, and viscous dissipation. The energy E is defined as

$$E = h - \frac{p}{\rho} + \frac{v^2}{2} \tag{4.5}$$

where h is the sensible enthalpy and for incompressible flow and is given as

$$h = \sum_j Y_j h_j + \frac{p}{\rho}. \tag{4.6}$$

Y_j is the mass fraction of species j and

$$h = \int_{T_{ref}}^{T} c_{p,j} dT \tag{4.7}$$

where T_{ref} is 298.15 K.

Compressible flows are typically characterized by the total pressure P_0 and total temperature T_0 of the flow. For an ideal gas, these quantities can be related to the static pressure and temperature by the following:

$$\frac{p_0}{p} = \exp\left(\frac{\int_{T}^{To} \frac{C_p}{T} dT}{R} \right) \tag{4.8}$$

For constant C_p, Equation 4.8 reduces to

$$\frac{p_0}{p} = \left(1 + \frac{\gamma - 1}{2} M^2\right)^{\gamma/(\gamma-1)} \tag{4.9}$$

$$\frac{T_o}{T} = 1 + \frac{\gamma - 1}{2} M^2 \tag{4.10}$$

These relationships describe the variation of the static pressure and temperature in the flow as the velocity and Mach number change under isentropic conditions. For example, given a pressure ratio (total to static) from inlet to exit, Equation 4.9 can be used to estimate the exit Mach number in a one-dimensional isentropic flow. For air, Equation 4.9 predicts a choked flow (Mach number of 1.0) at an isentropic pressure ratio, p/p_0, of 0.5283. This choked flow condition will be established at the point of minimum flow area (e.g., in the throat of a nozzle). In the subsequent area of expansion, the flow may either accelerate to a supersonic flow, in which the pressure will continue to drop, or return to subsonic flow conditions, which will decelerate with a pressure rise. If a supersonic flow is exposed to an imposed pressure increase, a shock will occur with a sudden pressure rise and deceleration across the shock.

4.5 Turbulence Model

The velocity field in turbulent flows always fluctuates. As a result, the transported quantities such as momentum, energy, and species concentration fluctuate as well. The fluctuations can be on a small scale and high frequency, which is computationally expensive to be directly simulated. To overcome this, a modified set of equations that are computationally less expensive to solve can be obtained by replacing the instantaneous governing equations with their time-averaged, ensemble-averaged, or otherwise manipulated to remove the small time scales. However, the modifications of the instantaneous governing equations introduce new unknown variables. Many turbulence models have been developed to determine these new unknown variables in terms of known variables. General turbulence models widely available are:

a. Spalart-Allmaras
b. k-ε models:

- Standard k-ε model
- RNG k-ε model
- Realizable k-ε model

c. k-ω model

- Standard k-ω model
- Shear-stress transport (SST) k-ω model

d. Reynolds Stress

e. Large Eddy Simulation

The standard k-ε turbulence model, which is the simplest two-equation turbulence model, is used in this simulation due to its suitability for a wide range of wall-bound and free-shear flows. The standard k-ε turbulence is based on the model transport equations for the turbulence kinetic energy, k, and its dissipation rate, ε. The model transport equation for k is derived from the exact equation; however, the model transport equation for ε is obtained using physical reasoning and bears little resemblance to its mathematically exact counterpart.

The standard k-ε turbulence model is robust, economic for computation, and accurate for a wide range of turbulent flows. The turbulence kinetic energy, k, and its rate of dissipations, ε, are calculated from the following equations

$$\frac{\partial}{\partial x_i}(\rho k u_i) = \frac{\partial}{\partial x_j}\left[\left(\mu + \frac{\mu_t}{\sigma_k}\right)\frac{\partial k}{\partial x_j}\right] + G_k + G_b - \rho\varepsilon - Y_M + S_k \qquad (4.11)$$

and

$$\frac{\partial}{\partial x_i}(\rho \varepsilon u_i) = \frac{\partial}{\partial x_j}\left[\left(\mu + \frac{\mu_t}{\sigma_\varepsilon}\right)\frac{\partial \varepsilon}{\partial x_j}\right] + C_{1\varepsilon}\frac{\varepsilon}{k}(G_k + C_{3\varepsilon}G_b) - C_{2\varepsilon}\rho\frac{\varepsilon^2}{k} + S_\varepsilon . \qquad (4.12)$$

In equations (4.8) and (4.9), G_k represents the generation of turbulence kinetic energy due to the mean velocity gradients and is defined as

$$G_\kappa = -\overline{\rho u_i' u_j'} \frac{\partial u_j}{\partial x_i}. \tag{4.13}$$

G_b represents the generation of turbulence kinetic energy due to buoyancy and is calculated as

$$G_b = \beta g_i \frac{\mu_t}{\mathrm{Pr}_t} \frac{\partial T}{\partial x_i}. \tag{4.14}$$

$\mathrm{Pr_t}$ is the turbulent Prandtl number and g_i is the component of the gravitational vector in the i-th direction. For standard k-ε model the value for $\mathrm{Pr_t}$ is set 0.85 in this study. The coefficient of thermal expansion, β, is given as

$$\beta = -\frac{1}{\rho}\left(\frac{\partial \rho}{\partial T}\right)_p. \tag{4.15}$$

Y_M represents the contribution of the fluctuating dilatation in compressible turbulence to the overall dissipation rate, and is defined as

$$Y_M = 2\rho\varepsilon M_t^2 \tag{4.16}$$

where M_t is the turbulent Mach number which is defined as

$$M = \sqrt{\frac{k}{a^2}} \tag{4.17}$$

where a $\left(\equiv \sqrt{\gamma RT}\right)$ is the speed of sound.

The turbulent viscosity, μ_k, is calculated from equation

$$\mu_k = \rho C_\mu \frac{k^2}{\varepsilon}. \tag{4.18}$$

The values of constants $C_{1\varepsilon}$, $C_{2\varepsilon}$, C_μ, σ_k, and σ_ε used are

$C_{1\varepsilon} = 1.44$, $C_{2\varepsilon} = 1.92$, $C_\mu = 0.09$, $\sigma_k = 1.0$, $\sigma_\varepsilon = 1.3$.

The turbulence models are valid for the turbulent core flows, i.e. the flow in the regions somewhat far from the walls. The flow very near the walls is affected by the presence of the walls. Viscous damping reduces the tangential velocity fluctuations and the kinematic blocking reduces the normal fluctuations. The solution in the near-wall region is very important because the solution variables have large gradients in this region.

Wall functions, which are a collection of semi-empirical formulas and functions, are employed to connect the viscosity-affected region between the wall and the fully-turbulent region. The wall functions consist of:

- laws-of-the-wall for mean velocity and temperature (or other scalars)
- formulas for near-wall turbulent quantities

There are two types of wall function: (a) standard wall function and (b) non-equilibrium wall function. The former is employed in this study. The wall function for the momentum is expressed as

$$U^+ = \frac{1}{\kappa}\ln\left(Ey^+\right) \tag{4.19}$$

where

$$U^+ \equiv \frac{U_P C_\mu^{1/4} k_P^{1/2}}{\tau_w / \rho} \tag{4.20}$$

$$y^+ \equiv \frac{\rho C_\mu^{1/4} k_P^{1/2} y_P}{\mu} \tag{4.21}$$

and

κ = von Karman constant (= 0.42)

E = empirical constant (= 9.793)

U_P = mean velocity of fluid at point P

k_P = turbulence kinetic energy at point P

y_P = distance from point P to the wall

μ = dynamic viscosity of the fluid.

The wall function for the temperature is given as

$$T^+ \equiv \frac{(T_w - T_P)\rho c_p C_\mu^{1/4} k_P^{1/2}}{\dot{q}} = \begin{cases} \Pr y^+, y^+ \langle y_T^+ \\ \Pr_t \left[\frac{1}{\kappa} \ln(Ey^+) + P \right], y^+ \rangle y_T^+ \end{cases} \tag{4.22}$$

where P is given as

$$P = 9.24 \left[\left(\frac{\Pr}{\Pr_T} \right)^{3/4} - 1 \right] \left[1 + 0.28 e^{-.007 \Pr/\Pr_T} \right] \tag{4.23}$$

and

r = density of the fluid

c_p = specific heat of fluid

q = wall heat flux

T_P = temperature at cell adjacent to the wall

T_W = temperature at the wall

Pr = molecular Prandtl number

$\Pr_t$ = turbulent Prandtl number (0.85 at the wall)

A = 26 (Van Driest constant)

κ = 0.4187 (von Karman constant)

E = 9.793 (wall function constant)

U_c = mean velocity magnitude at $y^+ = y^+_T$

y^+_T = non-dimensional thermal sublayer thickness.

In this project, the CFD simulated model's Y+ value is about 75 at the mid-chamber wall which is the place of most concerned. This Y+ value is adequate to use the standard-wall function.

In the k-ε model, the k equation is solved in the whole domain, including the wall-adjacent cells. The boundary condition for k imposed at the wall is

$$\frac{\partial k}{\partial n} = 0 \tag{4.24}$$

where n is the local coordinate normal to the wall. The production of kinetic energy, G_k, and its dissipation rate, □, at the wall-adjacent cells, which are the source terms in k equation, are computed on the basis of equilibrium hypothesis with the assumption that the production of k and its dissipation rate assumed to be equal in the wall-adjacent control volume. The production of k and □ is computed as

$$G_k \approx \tau_w \frac{\partial U}{\partial y} = \tau_w \frac{\tau_w}{\kappa \rho C_\mu^{1/4} k_p^{1/4} y_P} \tag{4.25}$$

and

$$\varepsilon_P = \tau_w \frac{C_\mu^{3/4} k_p^{3/2}}{k y_P}. \tag{4.26}$$

4.6 Boundary Conditions

Boundary conditions for all the computational cases simulated in this study are summarized in Table 4.1.

Table 4.1 Parameters and operating conditions for simulated cases

No-sheath cases

Parameter	***case 1***	***case 2***	***case 3***
Simulated condition	Lab conditon	Lab conditon	Real GT
Fluid	Compressible	Compressible	Compressible
Operating condition	103000 (Pa)	103000 (Pa)	1621200 (Pa)
Inlet	Pressure inlet: 500 (Pa)	Pressure inlet: 500 (Pa)	mass flow rate: 32 (kg/s)
Exit	Pressure outlet: -1675 (Pa)	Pressure outlet: -1675 (Pa)	Pressure outlet: 0 (Pa)
constant heat flux on mid-chamber and transitional piece	0 (W/m^2)	1500 (W/m^2)	310000 (W/m^2)

Sheathed cases

Parameter	***case 4***	***case 5***	***case 6***
Simulated condition	Lab conditon	Lab conditon	Real GT
Fluid	Compressible	Compressible	Compressible
Operating condition	103325 (Pa)	103325 (Pa)	1621200 (Pa)
Inlet	Pressure inlet: 200 (Pa)	Pressure inlet: 200 (Pa)	mass flow rate: 32 (kg/s)
Exit	Pressure outlet: -2000(Pa)	Pressure outlet: -2000 (Pa)	Pressure outlet: 0 (Pa)
Constant heat flux on mid-chamber and transitional piece	0 (W/m^2)	1500 (W/m^2)	310000 (W/m^2)

CHAPTER FIVE

COMPUTATIONAL RESULT

5.1 Computational Results and Discussions

In this study, a total of six CFD Cases using four different geometrical models are conducted and four experimental Cases are processed.

- No-sheath model:

  Case 1. Laboratory conditions employed fluid mechanics study only (corresponding to Experimental Case 1)

  Case 2. Laboratory conditions employed both fluid mechanics and a heat transfer study (corresponding to Experimental Case 2)

  Case 3. Elevated high pressure and temperature conditions as in a real GT employed both fluid mechanics and a heat transfer study

- Sheathed model:

  Case 4. Laboratory conditions employed fluid mechanics study only (corresponding to Experimental Case 3)

  Case 5. Laboratory conditions employed both fluid mechanics and heat transfer study (corresponding to Experimental Case 4)

  Case 6. Elevated high pressure and temperature conditions as in a real GT employed both fluid mechanics and a heat transfer study

5.1.1 Case 1 (no-sheath, unheated)

To verify the validity of the computational results**,** Case 1 employs 103,500 Pascal absolute total pressure as the inlet condition, which is the same total pressure supplied by the wind tunnel. The computed pressure will be compared with the actual pressure measurements of Experimental Case 1.

The 3-D computational domain is shown in Fig. 5.1. A pressure distribution on the mid-chamber and transitional piece walls is shown in Fig. 5.2. The representative pathlines for Case 1 are shown in Fig. 5.3. Some pathlines are seen to quickly get into the combustor sleeve from the inner part of dump diffuser, while some pathlines show the flow circulating a bit in the outer dump diffuser before it moves into the combustor sleeve.

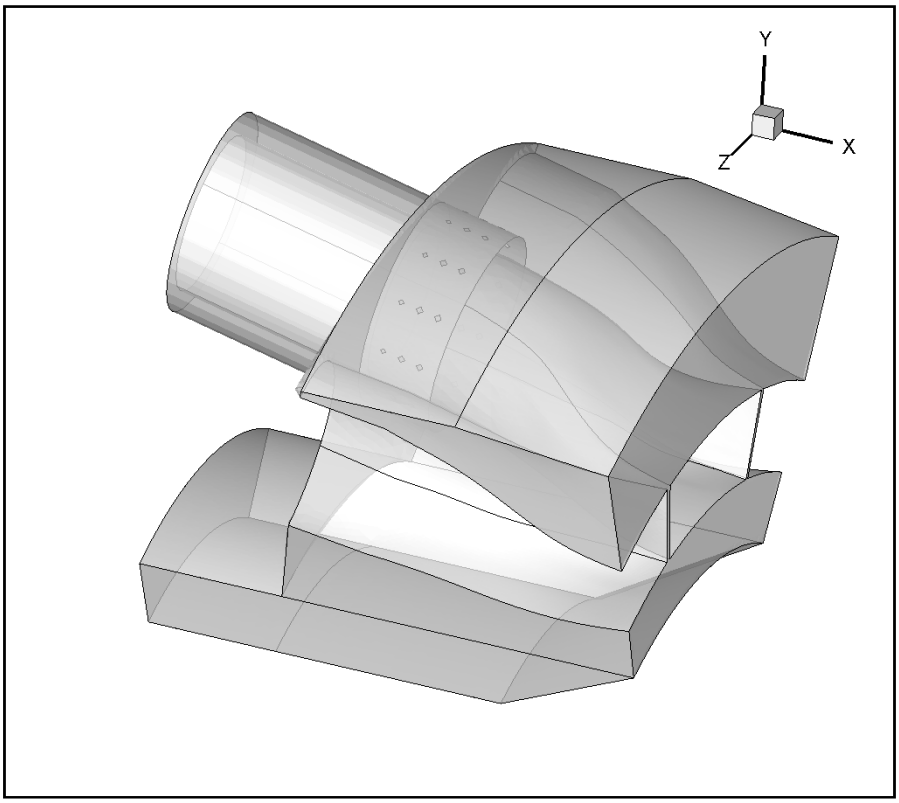

Figure 5.1 The 3-D model of no-sheath Case simulating one full chamber and two adjacent half chambers (Case 1)

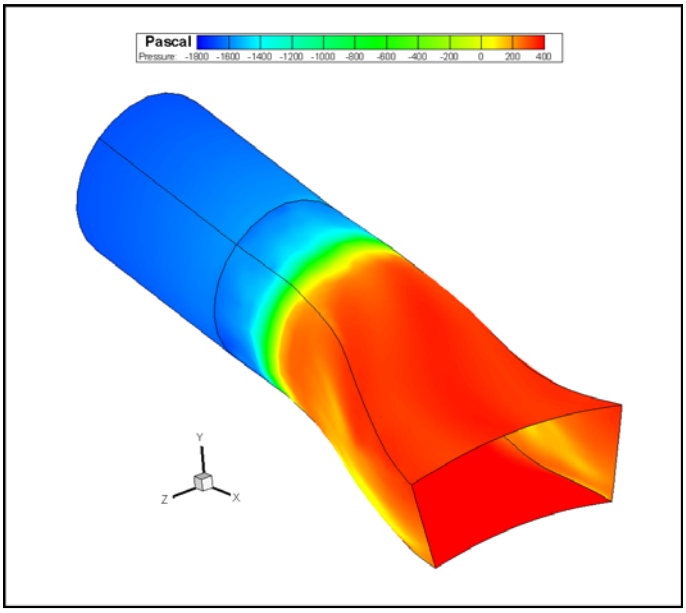

Figure 5.2 Pressure contour on mid-chamber and transitional piece walls (Case 1)

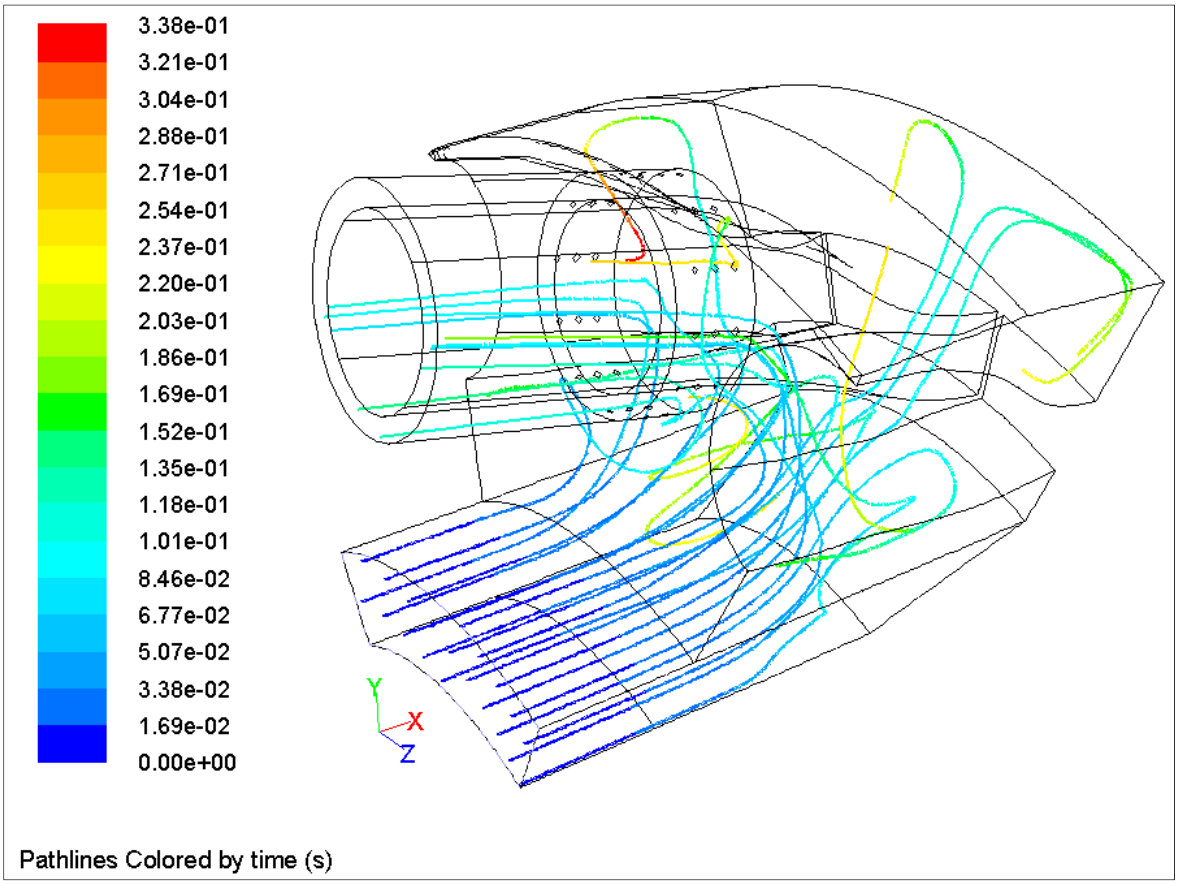

Figure 5.3 Representative pathlines (Case 1)

Velocity vector profile colored by static pressure distribution are shown in different planes on the directions of X (main flow direction in the dump-diffuser), Y (vertical) and Z (horizontal) respectively (Fig. 5.4, Fig. 5.5, and Fig. 5.6). The flow field shows a complex pattern with areas of stagnation, circulation, and flow reversal.

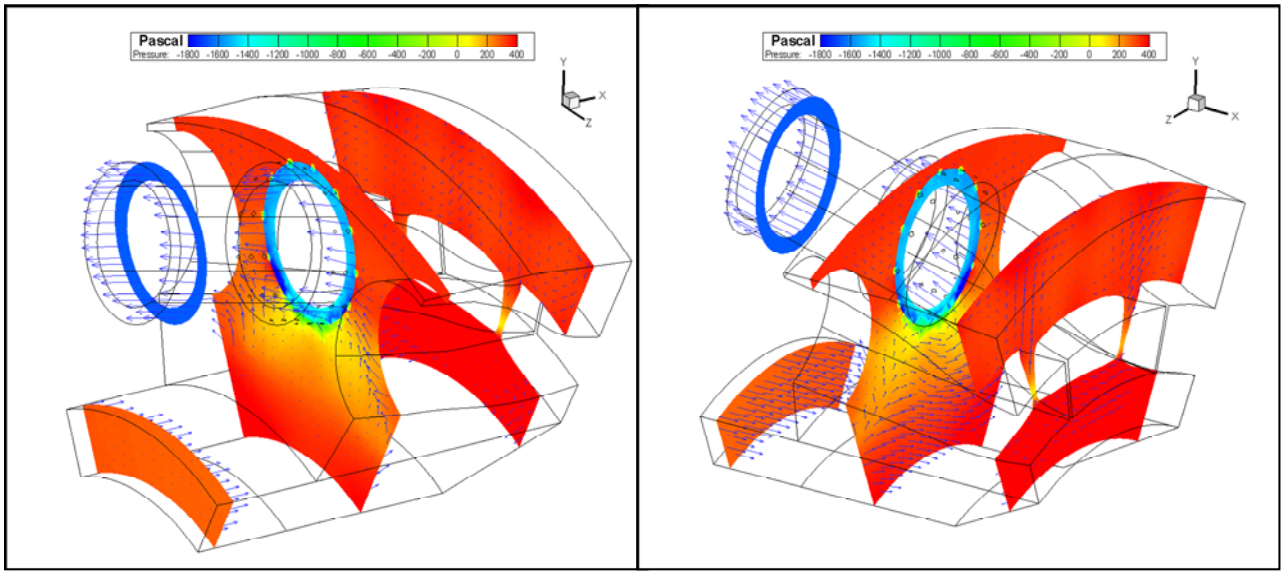

Figure 5.4 Velocity vector plots on different X-direction planes colored by pressure distribution (Case 1)

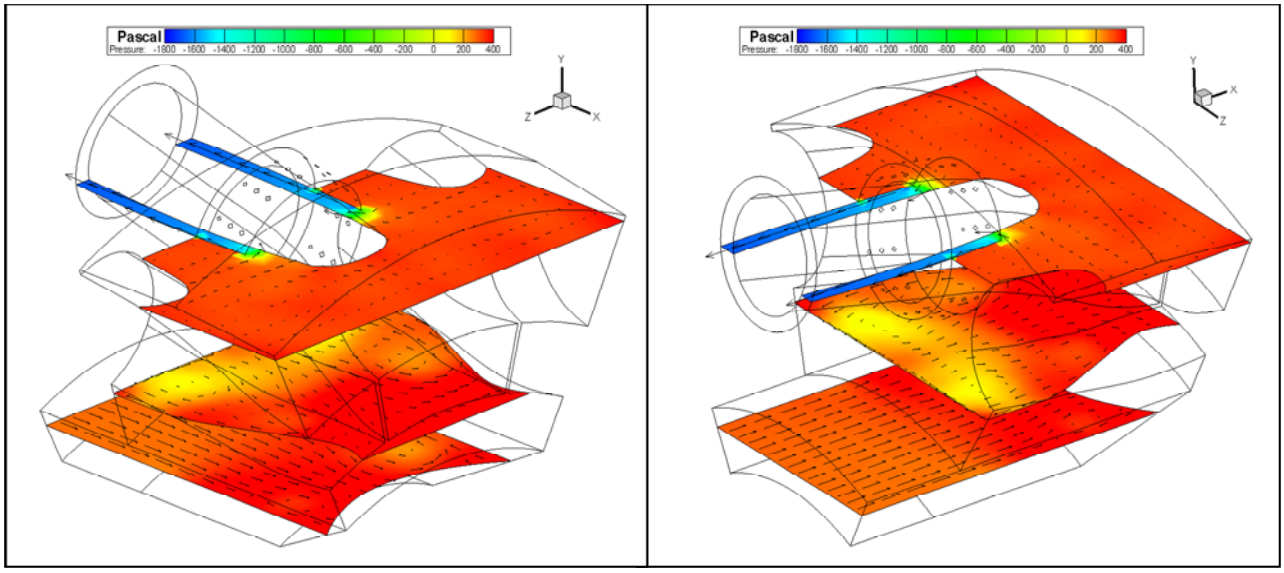

Figure 5.5 Velocity vector plots on different Y-direction planes with colored pressure distribution (Case 1)

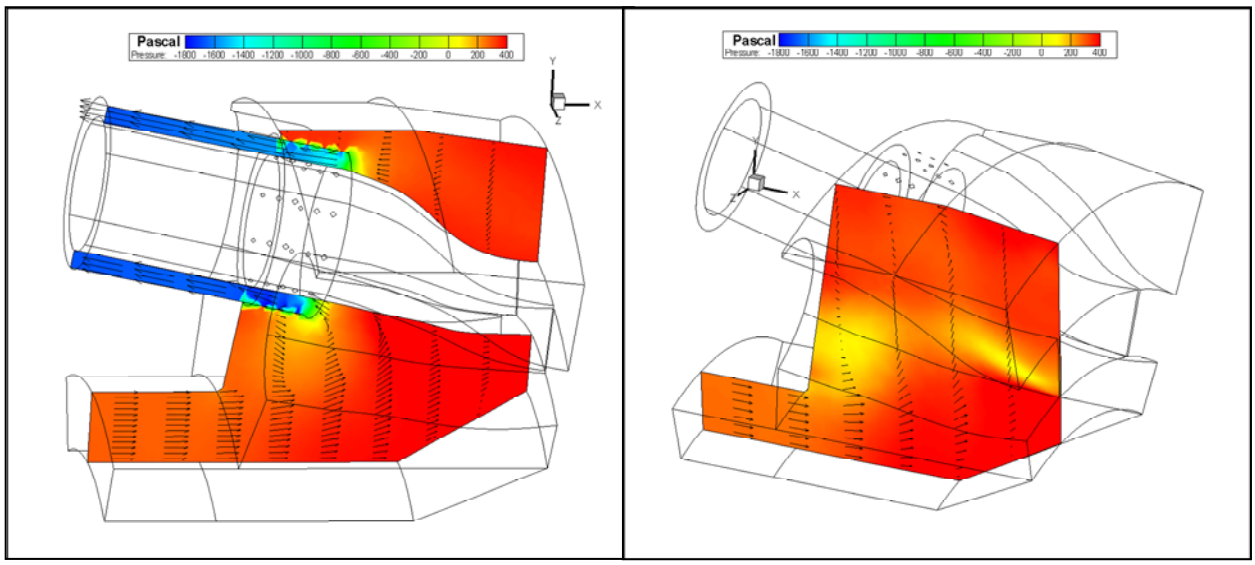

Figure 5.6 Velocity vector plots on different Z-direction planes with colored pressure distribution (Case 1)

The velocity profiles and pressure contours at different locations are shown in Fig. 5.7. It is clear to observe the flow separation happening inside the dump-diffuser in Fig. 5.7 (a), (b), and (c). The velocity is accelerated in the combustor sleeve leading to vacuum (or a negative static pressure) inside the sleeve.

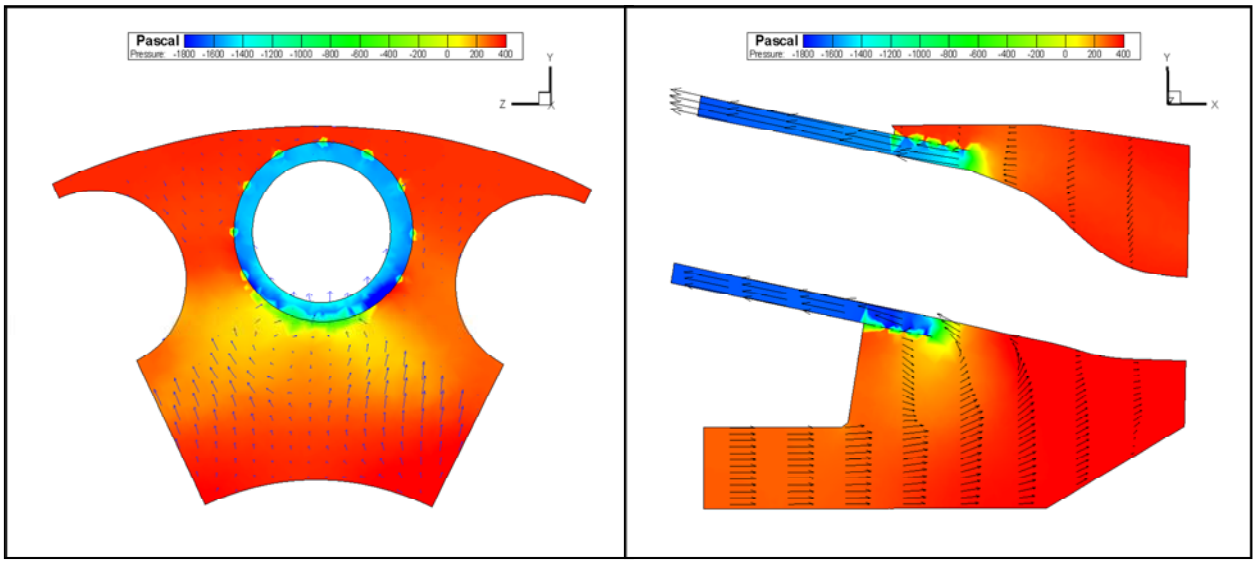

(a) X=0.6 plane velocity profile and static pressure contours

(b) Z=0 plane velocity profile and static pressure contours

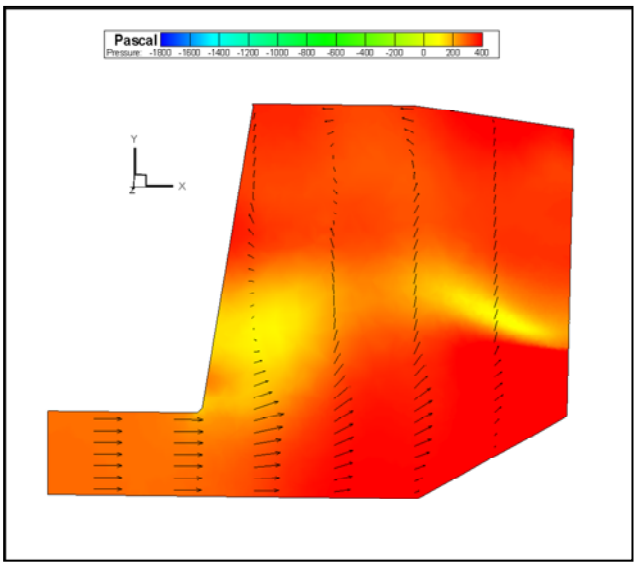

(c) Radial plane halfway between two combustors

Figure 5.7 Velocity profile colored by static pressure contours at different locations (Case 1)

The CFD result is compared with the experimental data in Fig. 5.8. The measured pressure data are listed in Appendix C. It can be seen that typically the CFD results are more smoothly distributed with higher values than the experimental data. The areas of pressure recession in the middle combustor's front and back locations have been accurately captured by the CFD (see Fig. 5.8). However, the descending trend of pressure distribution in the bottom of the middle combustor has not been adequately captured by the CFD simulation.

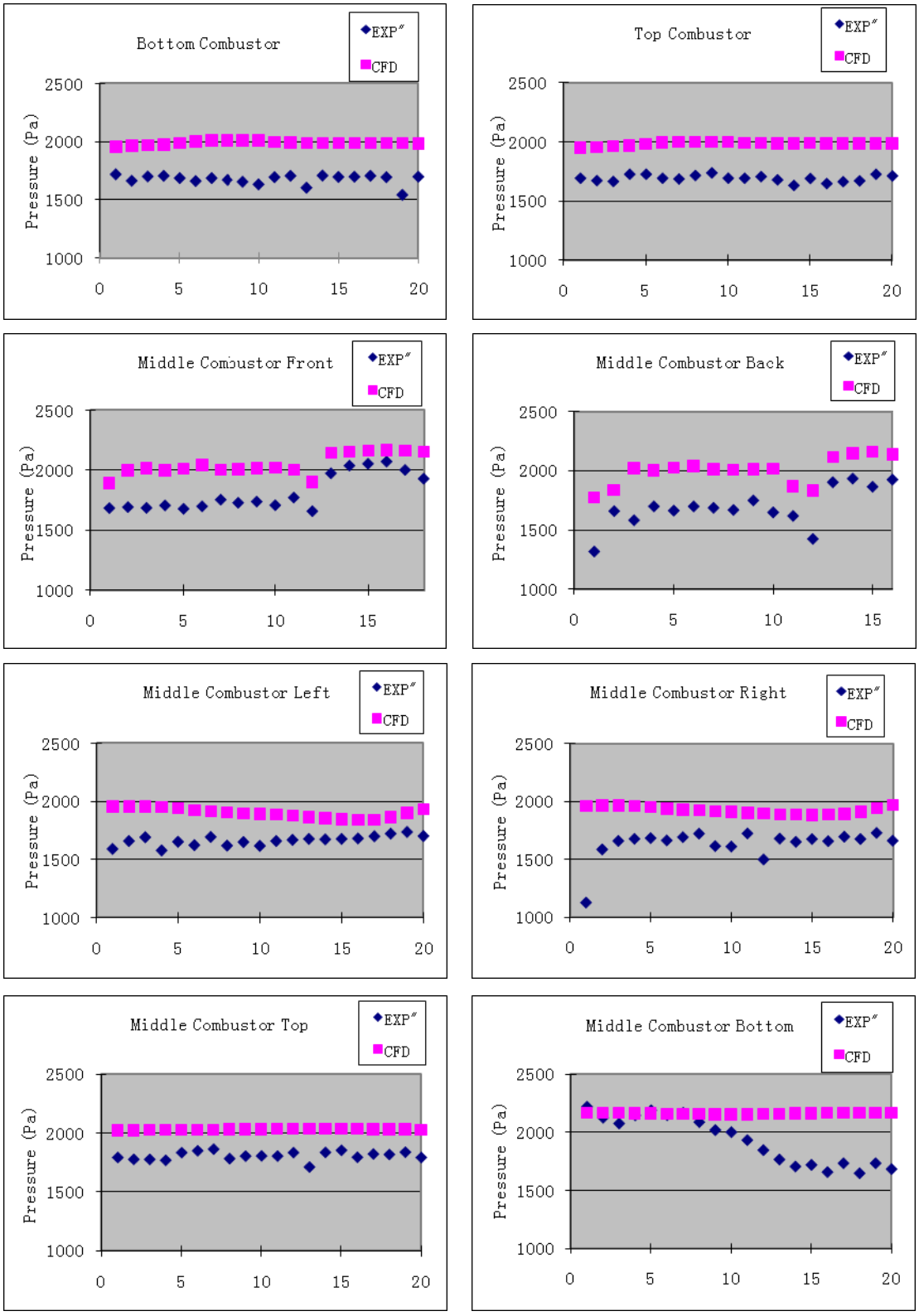

Figure 5.8 Comparison of static pressure between experimental and CFD data (Case 1)

5.1.2 Case 4 (sheathed, unheated)

The effect of installing a sheath on the fluid flow field and pressure distribution can be seen in Case 4. Fig.5.9 shows the 3-D computational model, and Fig.5.10 provides a translucent view of 470 cooling holes on the sheath. Pressure distribution on the mid-chamber and transitional piece walls is shown in Fig 5.11. The representative pathlines for Case 4 is shown in Fig. 5.12. From the color (representing length of time) of the pathlines, more time will be needed by some pathlines to enter the sheath through those impinging holes. The animation movie (not shown here) of the flow motion shows that some flow particles will take five times longer to find their ways into the sheath.

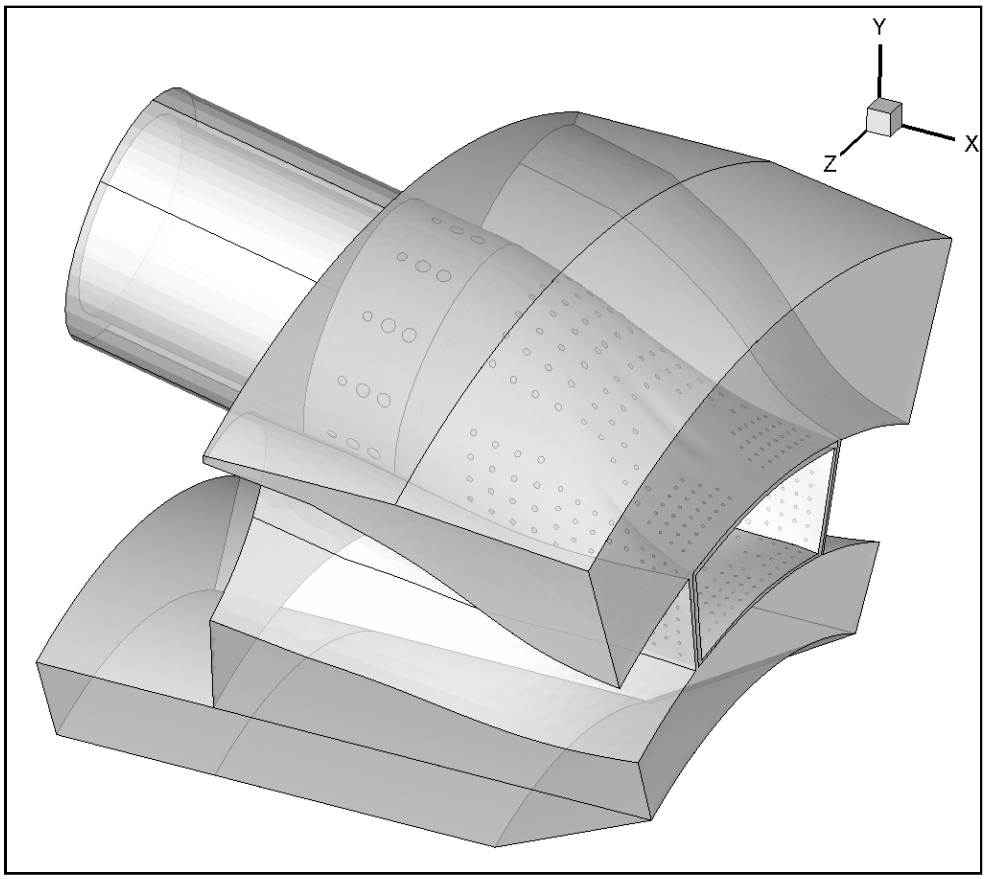

Figure 5.9 3-D model of sheathed Case simulating one full chamber and two adjacent half chambers (Case 4)

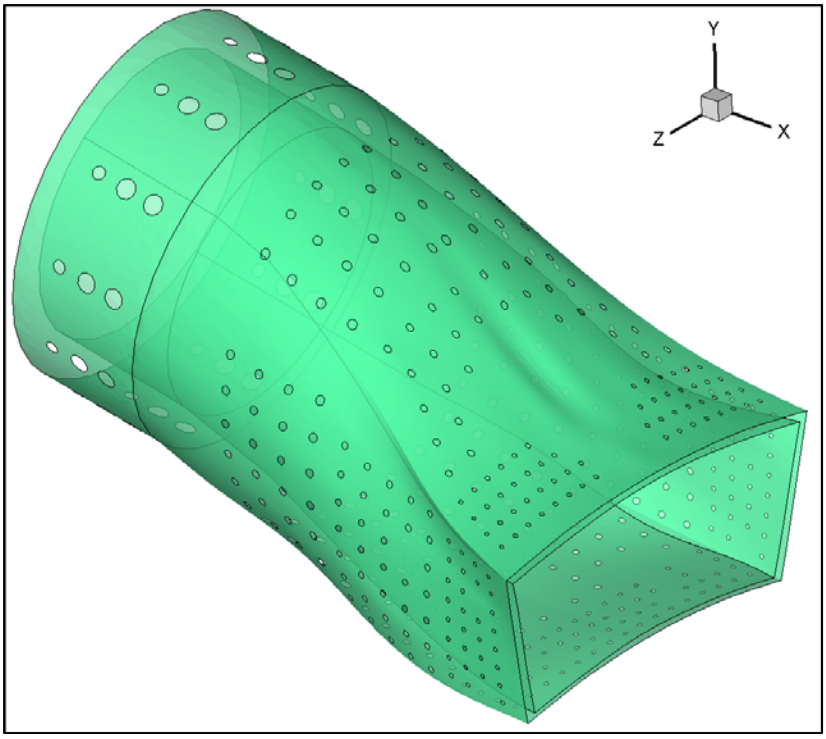

Figure 5.10 Sheath outside the transitional piece walls

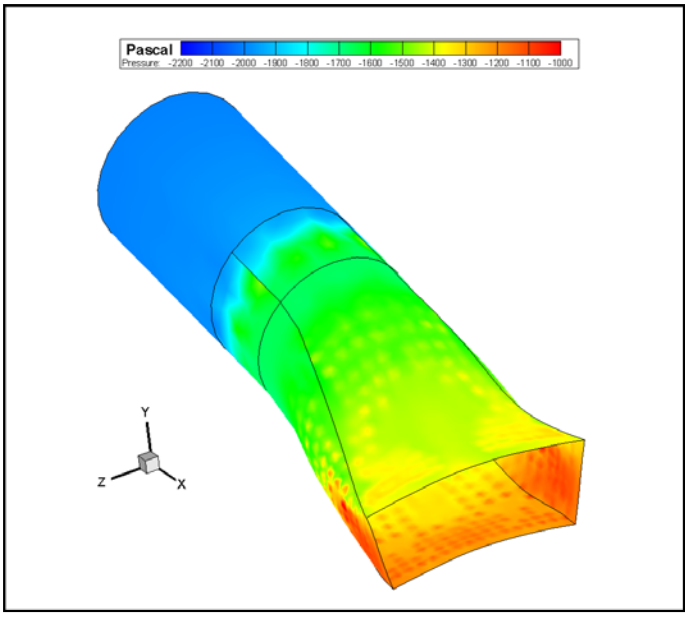

Figure 5.11 Pressure contour on mid-chamber and transitional piece walls (Case 4)

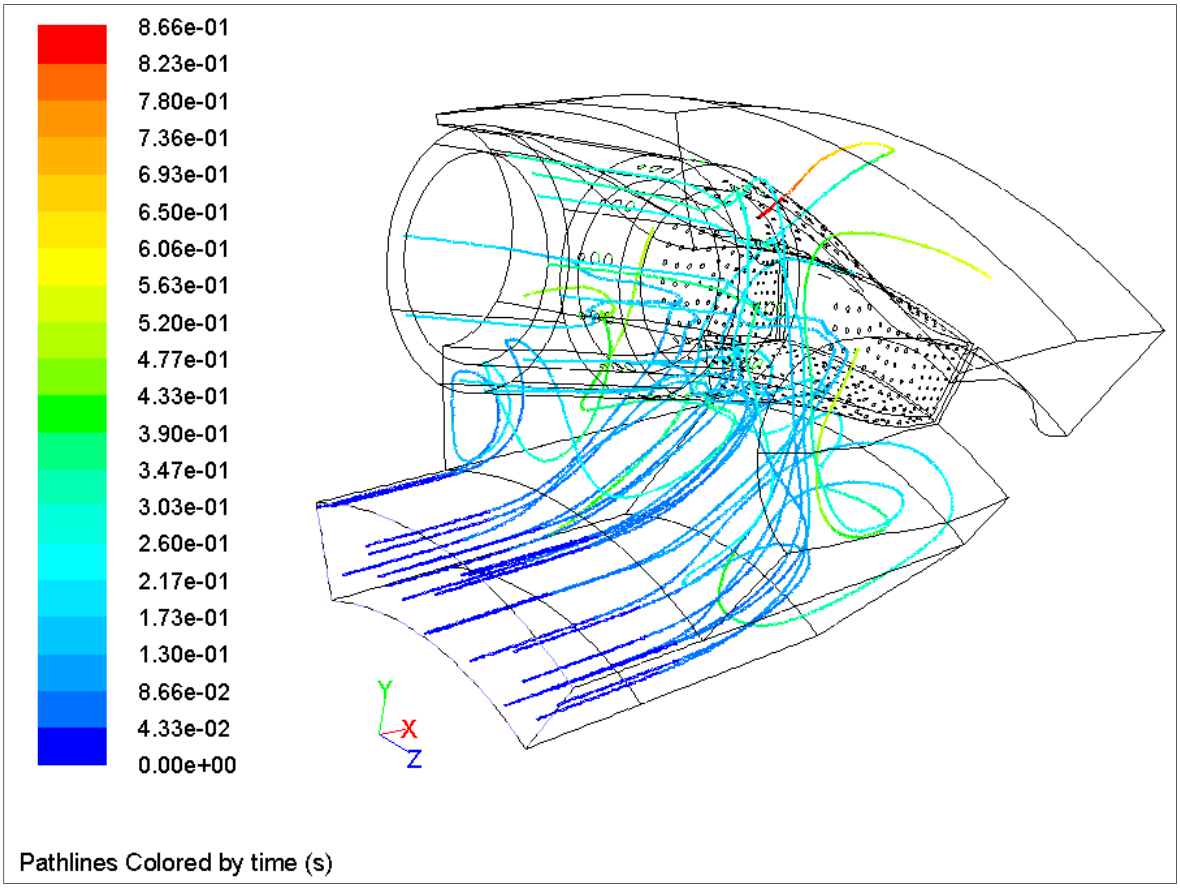

Figure 5.12 Representative pathlines from inlet to exit of sheathed case (Case 4)

Velocity vector plots with colored static pressure distributions are shown in different planes in the direction of X (main flow direction in the dump-diffuser), Y (vertical) and Z (horizontal) respectively (Figs 5.13 - 5.15). Larger areas of slow moving flow is seen in the outer dump diffuser for sheathed Case 4 than in the no-sheath Case 1 (Fig.5.4 - 5.7)

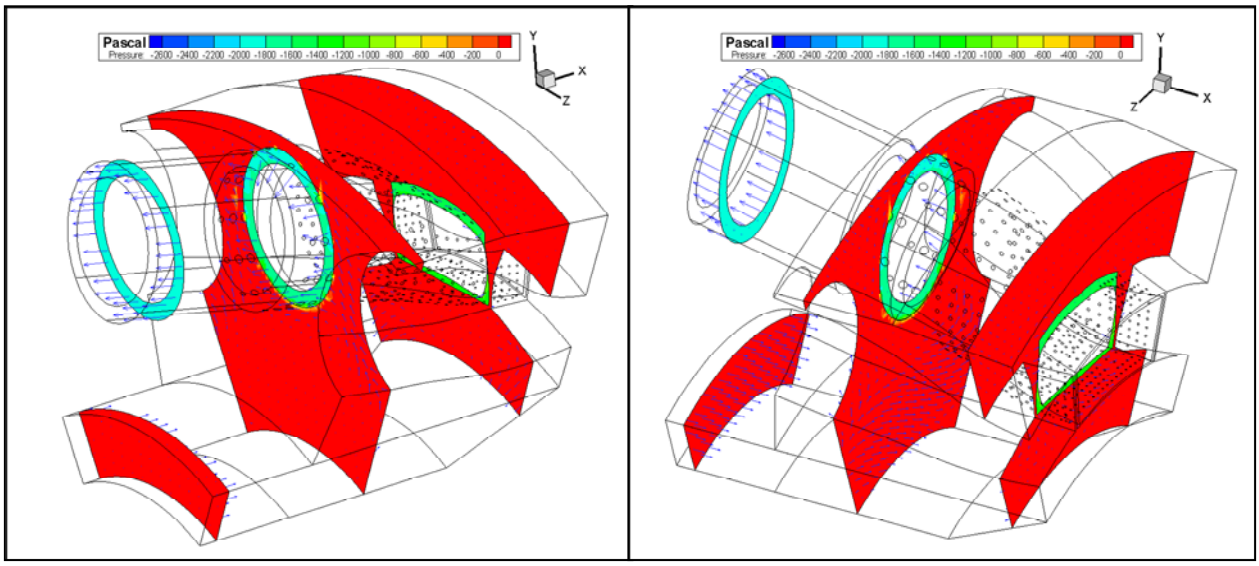

Figure 5.13 Velocity vector plots on different X-direction planes colored by static pressure distribution (Case 4)

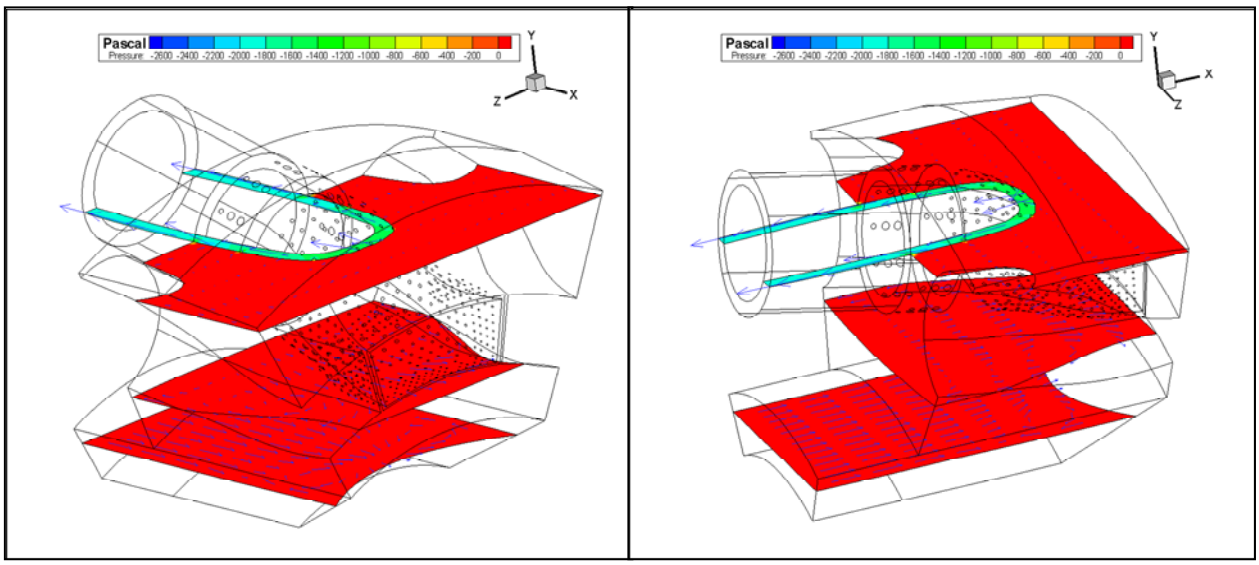

Figure 5.14 Velocity vector plots on different Y-direction planes with colored static pressure distribution (Case 4)

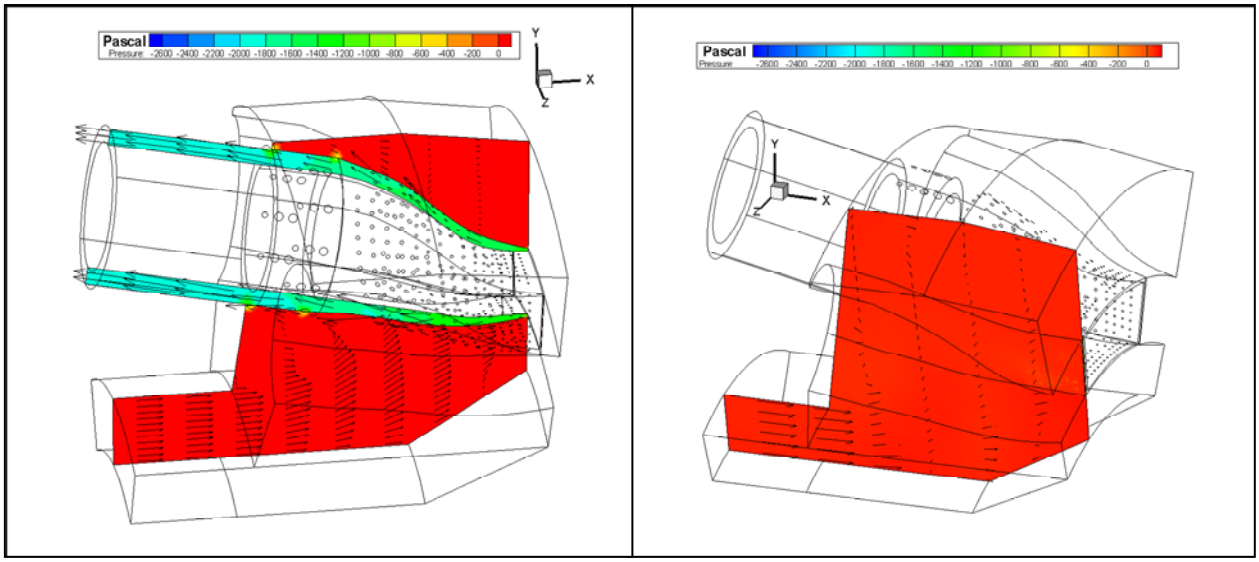

Figure 5.15 Velocity vector plots on different Z-direction planes with colored static pressure distribution (Case 4)

Fig 5.16 shows the velocity profiles at different locations. Flow separation is seen to happen inside the dump-diffuser in Fig. 5.16 (a), (b), and (c).

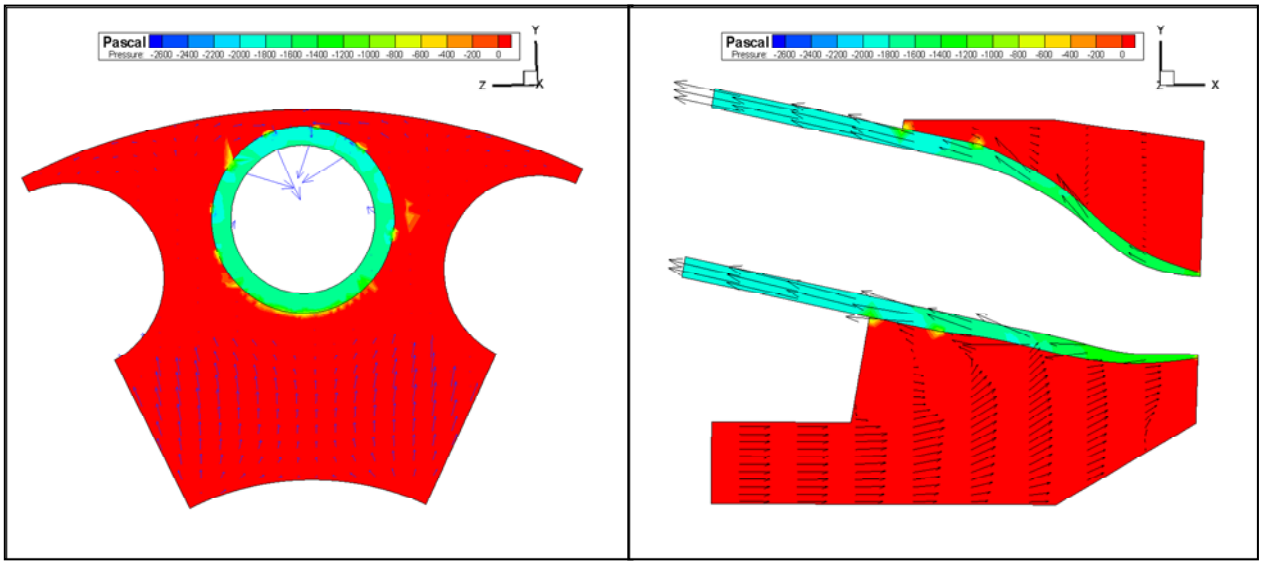

(a) X=0.6 plane velocity profile and static pressure contour

(b) Z=0 plane velocity profile and static pressure contour

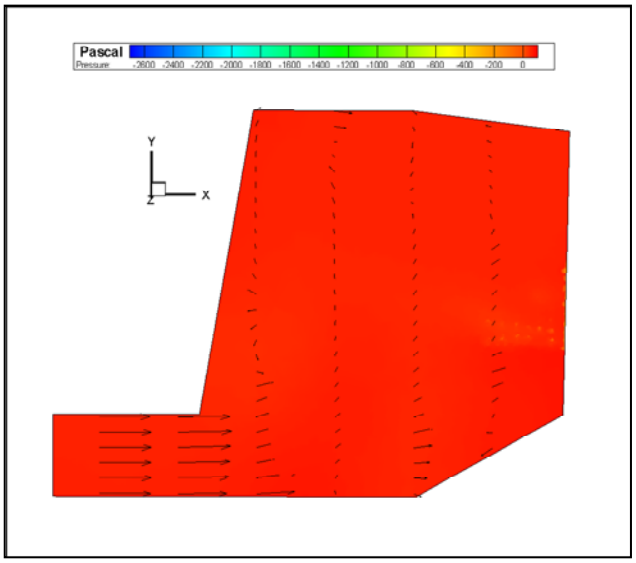

(c) Radial plane halfway between two combustors.

Figure 5.16 Velocity profile imposed by colored pressure distribution at different locations (Case 4)

Case 1 is compared with the Experimental Case 3. The measured pressure data are listed in Appendix C. After employing the sheath, the pressure drop on the mid-chamber and transitional piece walls is large compared with the no-sheath Case 1. Fig.5.17 shows the comparison between the Experimental Case 3 and CFD results of Case 4.

It can be seen that typically the CFD results are more smoothly distributed with higher values than the experimental data. The areas of pressure recession in the middle combustor's front and back locations have been accurately captured by the CFD result (see Fig. 5.17). However, the descending trend of pressure distribution either at the top of the middle combustor, or in the left and right of the middle combustor has not been captured by the CFD simulation.

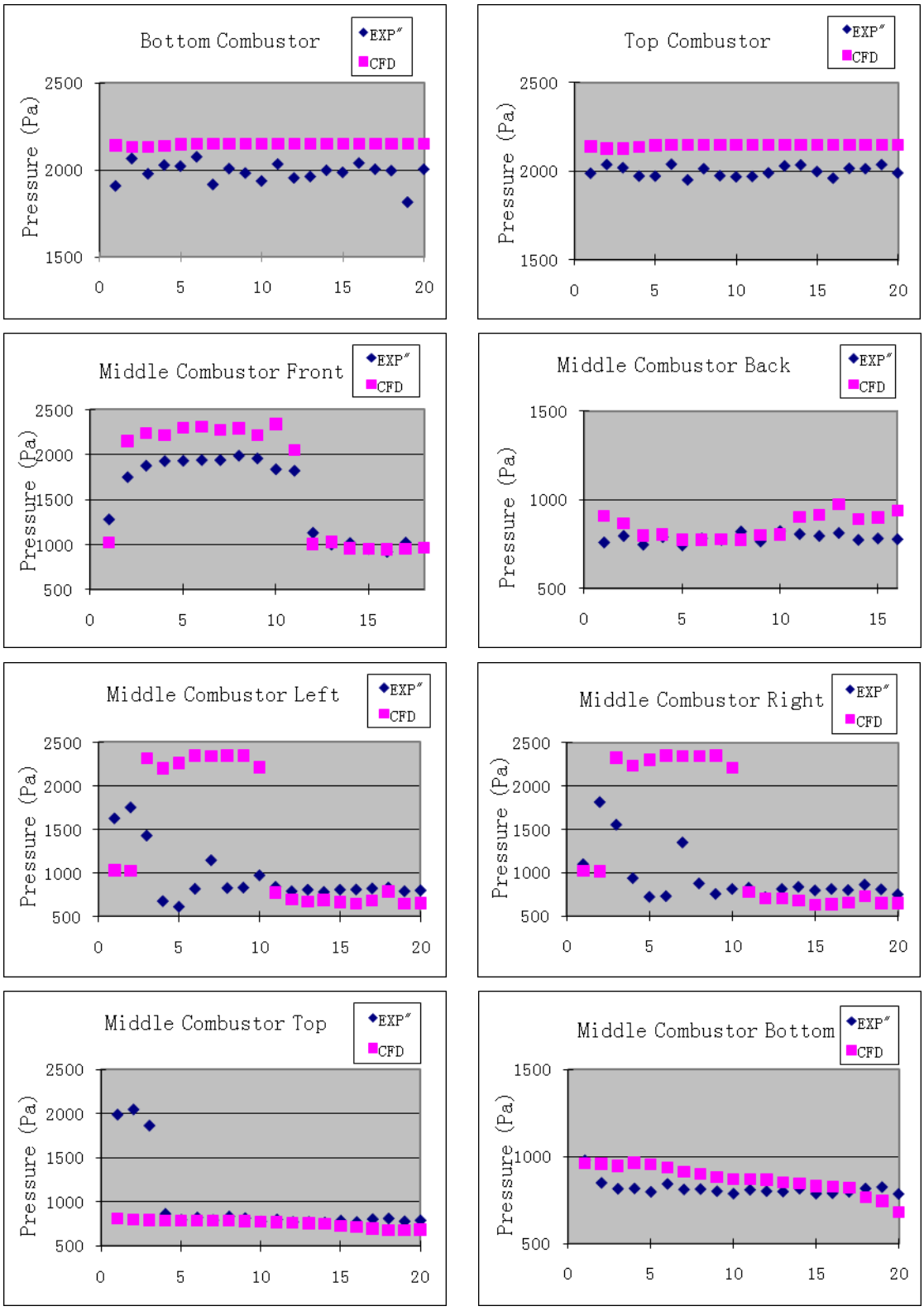

Figure 5.17 Comparison between the experimental and CFD static pressure data (Case 4)

5.1.3 Case 1(no-sheath, unheated) versus Case 4 (sheathed, unheated)

To make a comparison between Case 1 and Case 4 and to show the pressure losses caused by employing the sheath, the same global color scale is used in Fig. 5.18. (Note: The pressure contours shown in Fig. 5.2 and Fig. 5.11 in the previous section used local color scale to show more clearly views of the pressure variations).

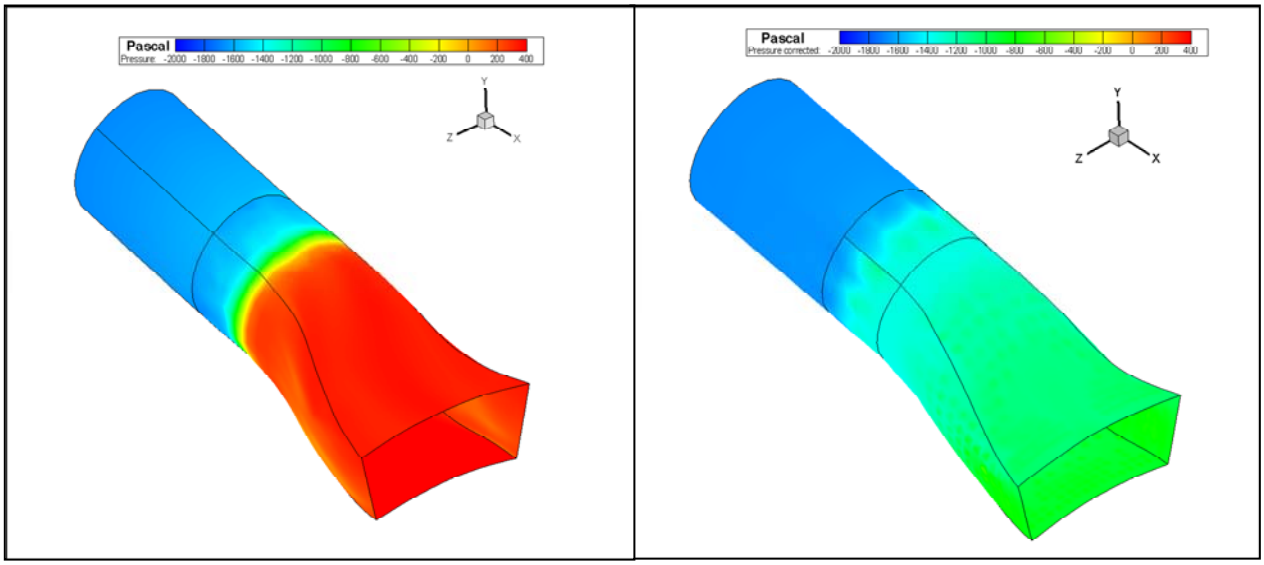

(a) Case 1 **(b) Case 4**

Figure 5.18 Comparison of CFD simulated static pressure contour between Case 1 (unheated, no-sheath) and Case 4 (unheated, sheathed)

It is easy to observe that the main pressure difference between Cases 1 and 2 happen at the transitional piece part. The result in Fig. 5.18 indicates that the pressure losses caused by employing the sheath could be up to 4% of the total pressure at the inlet in comparison to 1% of no-sheath Case.

5.1.4 Case 2 (no-sheath, heated)

Case 2 adds constant heat flux (1,500W/m^2) on the mid-chamber and transitional piece walls. This uniformly heated case is not compared with the experimental case because the experiment was conducted by applying forced convective heating from inside the combustion chamber. This experimental setup simulated more closely the combustion heat transfer; but it will not provide the same thermal boundary condition as the CFD case. Even without a direct comparison with the experimental data, the information obtained by comparing the no-sheath CFD results with the sheathed CFD results is still useful. The temperature distributions on mid-chamber and transitional piece walls and inside the dump-diffuser plenum are shown in Fig. 5.19.

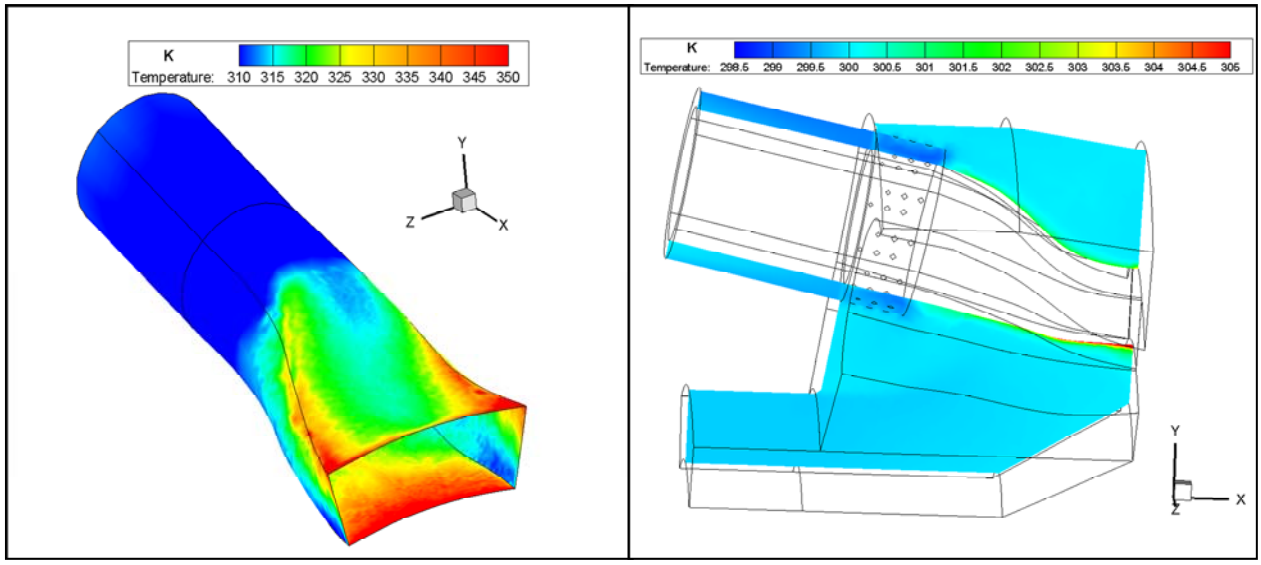

(a) **(b)**

Figure 5.19 (a) Temperature distributions on mid-chamber and transitional piece walls (b) Temperature distributions in the dump diffuser around the combustor (Case 2)

5.1.5 Case 5 (sheathed, heated)

The same approach is taken for the sheathed case as the non-sheathed case by adding constant heat flux on the mid-chamber and transitional piece walls to simulate the Experimental Case 4. The quantity of the heat flux is estimated based on an analytical calculation documented in Appendix A. Besides employing the constant heat flux, other boundary conditions all remain the same as in the experiment of Case 4. The temperature distributions on mid-chamber and transitional piece walls and inside dump-diffuser are shown in Fig 5.20.

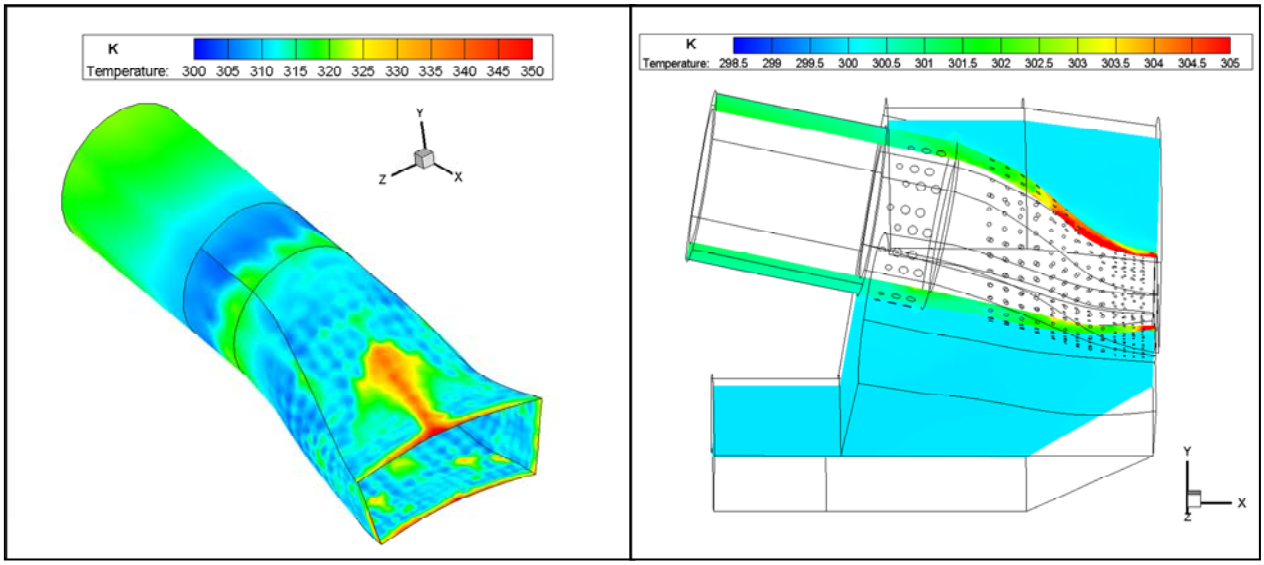

(a) **(b)**

Figure 5.20 (a) Temperature distributions on mid-chamber and transitional piece walls (b) Temperature distributions in the dump diffuser around the combustor (Case 5)

5.1.6 Case 2(no-sheath, heated) versus Case 5 (sheathed, heated)

The same color scale for the two cases is used to provide a direct comparison between Cases 2 and 5 and to examine the effect of employing the sheath. Fig. 5.21 shows the temperature distribution on the mid-chamber for the two cases using the same global color scale. The cooling effect of the numerous impinging jets is clearly seen in Case 5 (Fig. 5.21).

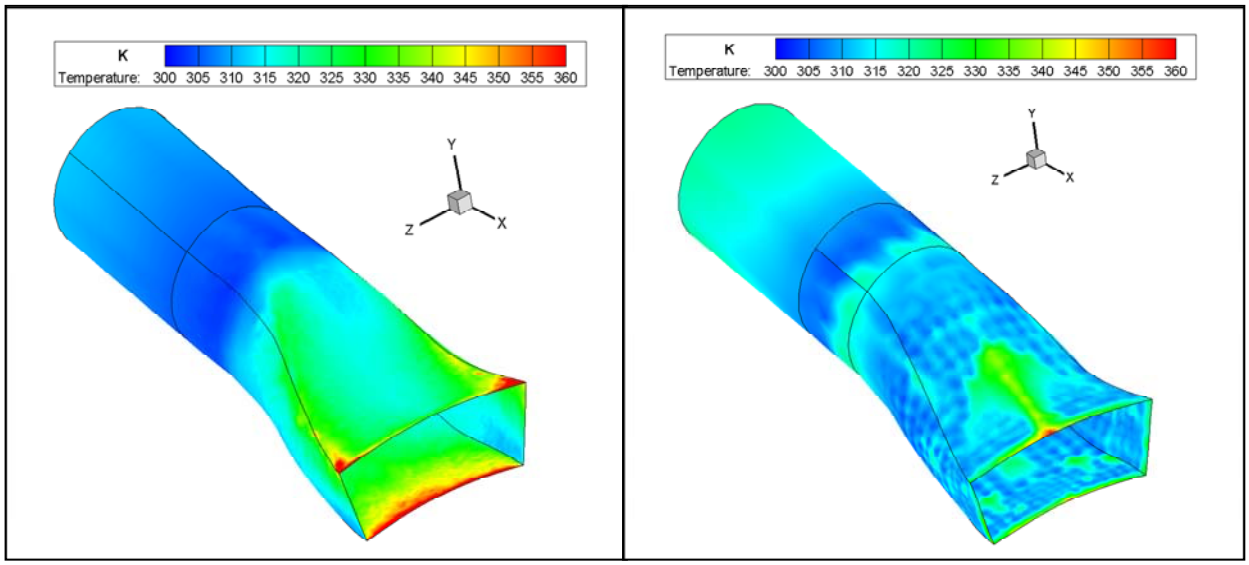

(a) Case 2 **(b) Case 5**

Figure 5.21 Comparison of temperature distributions on mid-chamber between Case 2 (no-sheath, heated) and Case 5 (sheathed, heated)

Figure 5.21 provides a global temperature comparison between Cases 2 and 5 in a more qualitative way, while Figure 5.22 shows quantitative comparison at selected locations where thermocouples are instrumented. The direct comparison with the experimental data is not shown here due to different thermal boundary conditions, rather it is shown in Appendix D. Employing the sheath enhances the cooling effectiveness by about 20K near the transition piece exit close to the turbine from the no-sheath case. A narrow region on the top-middle of the transitional piece for the sheathed case is seen to be even hotter than the no-sheath case. This is a region where

flanges are located to hold two molded transition pieces together in the experimental test piece with no impinging hole being placed nearby.

In Fig. 5.22, the temperature distributions on the left and right portion of the chamber are generally symmetric. The temperature on Top Right and Top Left for the sheathed case reduces sharply at the near turbine region (lower location counts); it then increases to the peak value and decreases again. At the Top-middle region, cooling jet holes are not employed in this area due to the flanges' location, which explains the phenomena that the peak value of sheathed case in this area is even higher than the corresponding no-sheath case value. The temperature on Right and Left for the sheathed case slightly decreases in the near turbine region and increases away from the turbine inlet. The temperature on Bottom Right and Bottom Left for the sheathed case shows a similar tendency as those on the Right and Left surfaces. General speaking, all the temperatures for the no-sheath case are higher than those of the sheathed case, and it slowly decreases from the near turbine region to the other end near the combustor region except on the Top-middle Right and Top-middle Left surfaces.

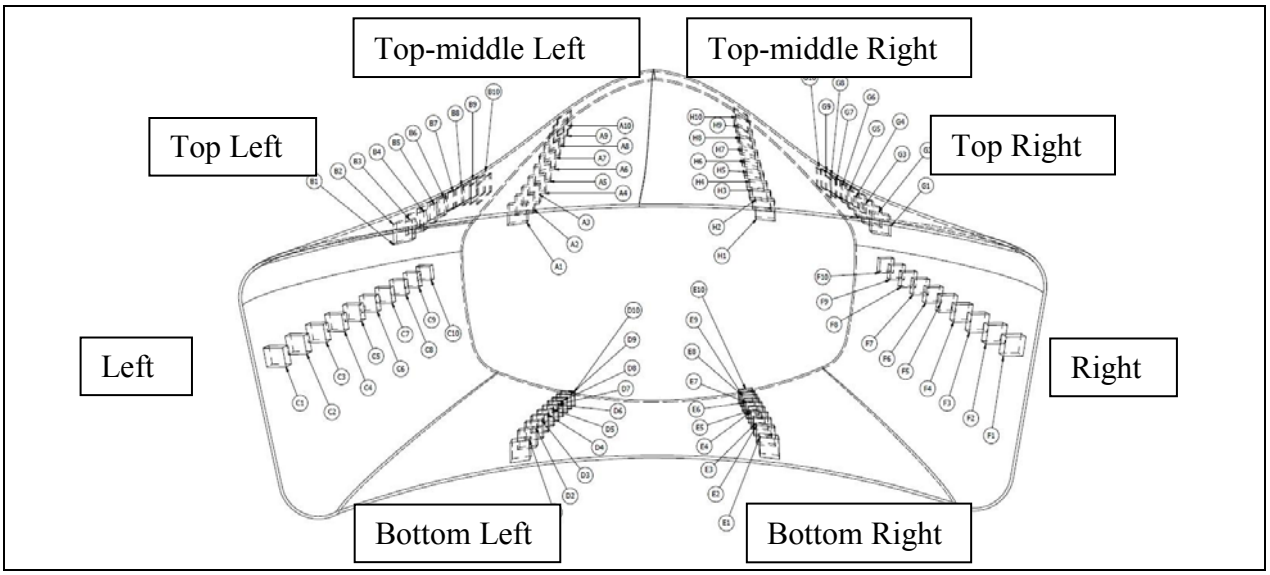

(a)

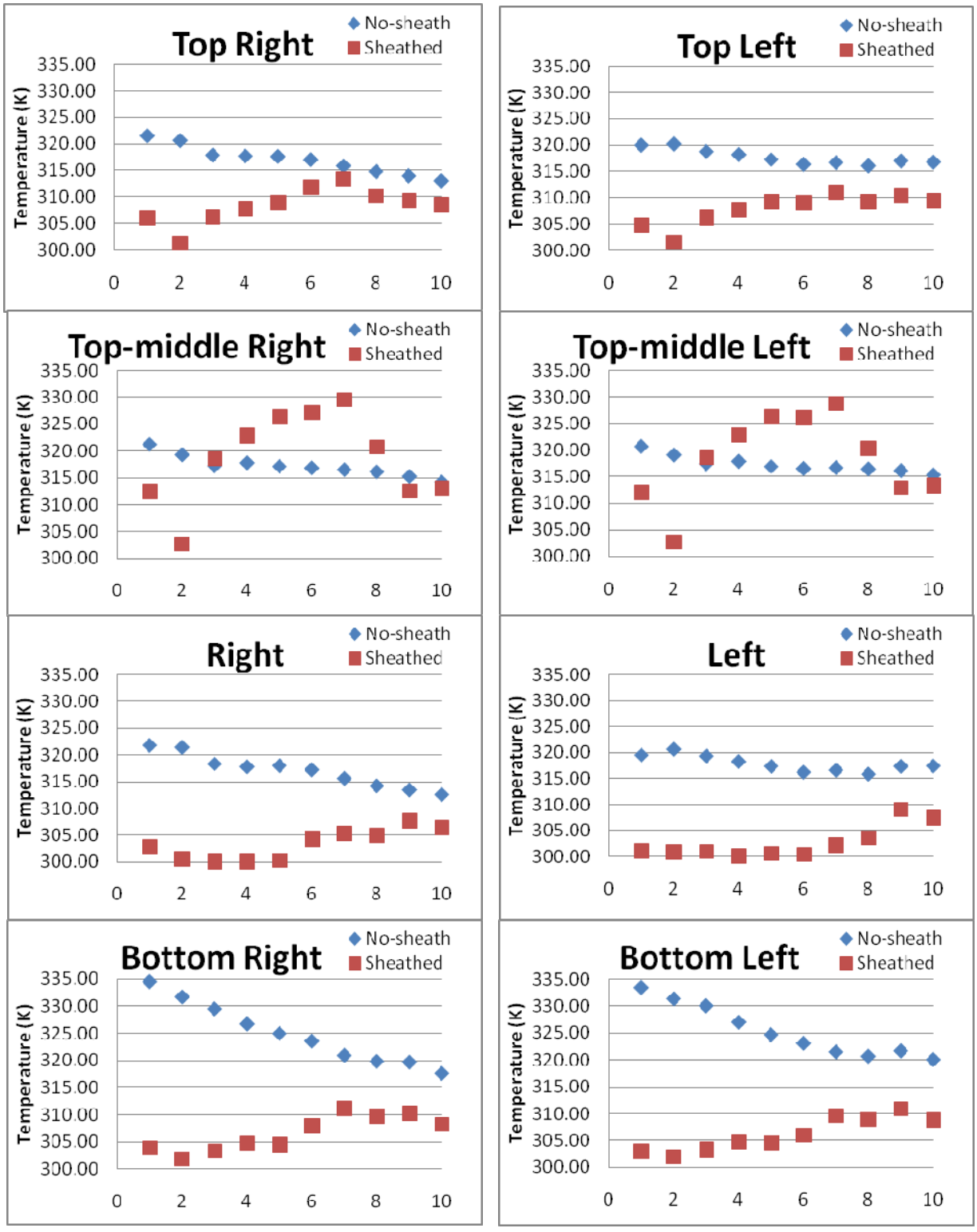

(b)

Figure 5.22 (a) Temperature measurement locations' reference; (b) Temperature comparisons between Case 2 (no-sheath, heated) and Case 5 (sheathed, heated)

5.1.7 Case 3 (elevated gas turbine condition, no-sheath)

It is easier and more cost effective to use CFD simulation than actually conduct experiments to obtain a preliminary idea of the real GT combustor's aerodynamic and thermodynamic behaviors in very high pressure (16atm) and high temperature (3000°F) conditions. Case 3 is conducted for this reason. There are 14 identical individual combustion chambers in the studied real gas turbine system. A section of 1/14th of the system (Fig. 5.23) is simulated by applying periodic wall conditions with the combustor centered in the computational domain. This is different from Cases 1, 2, 4 and 5, where each has the computational domain exactly like the experimental set up with one full combustor and two half combustors on either side of the full combustor. Pressure distributions on the mid-chamber and transitional pieces are shown in Fig 5.24.

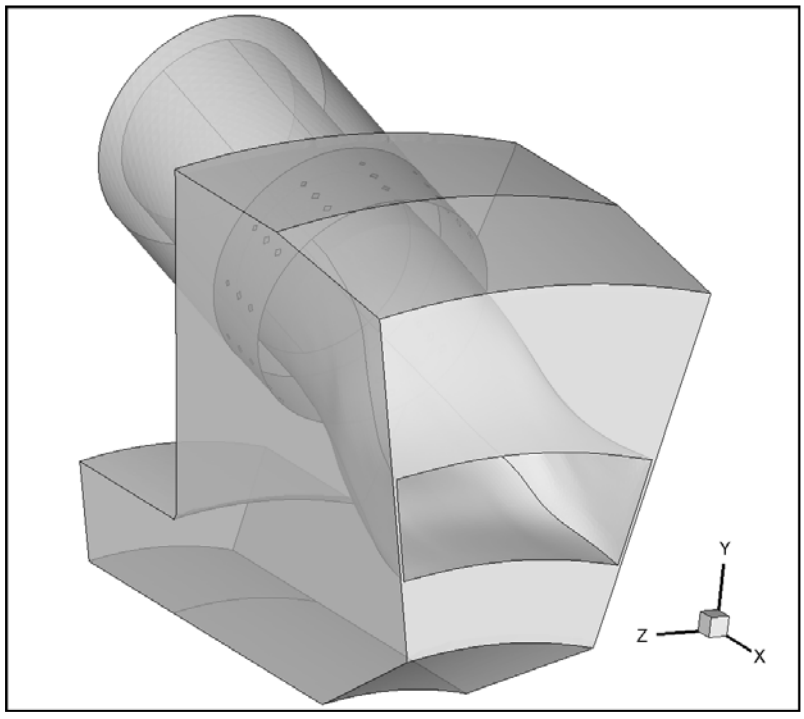

Figure 5.23 3-D model for elevated real gas turbine operating condition with a 1/14th computational domain without sheath by employing the periodic wall condition (Case 3)

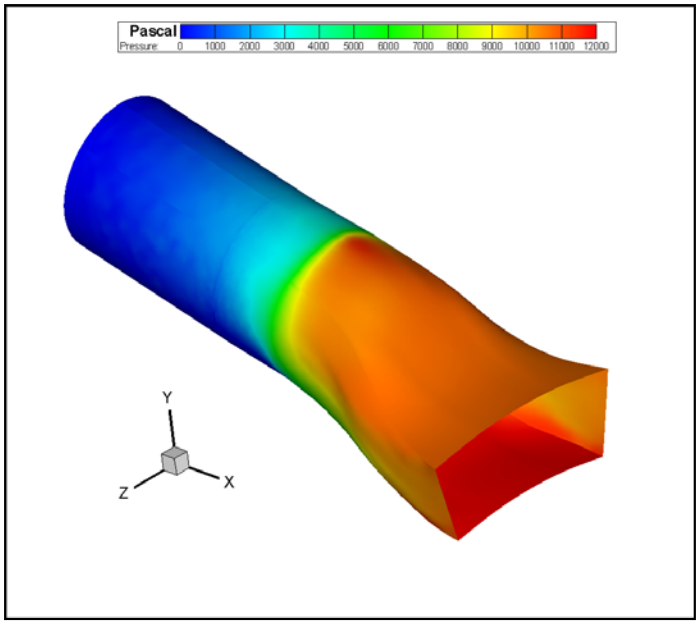

Figure 5.24 Pressure contour on chamber and transitional piece walls for elevated conditions of Case 3 (elevated gas turbine condition, no-sheath)

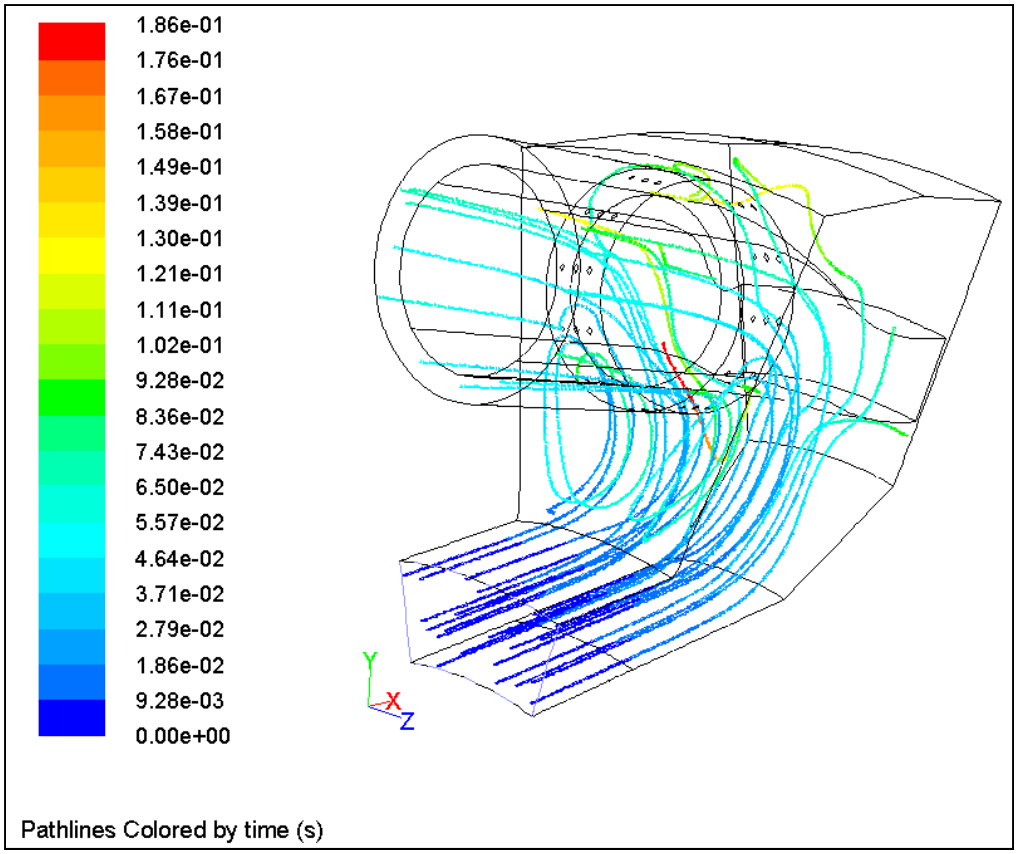

Figure 5.25 Representative pathlines (Case 3)

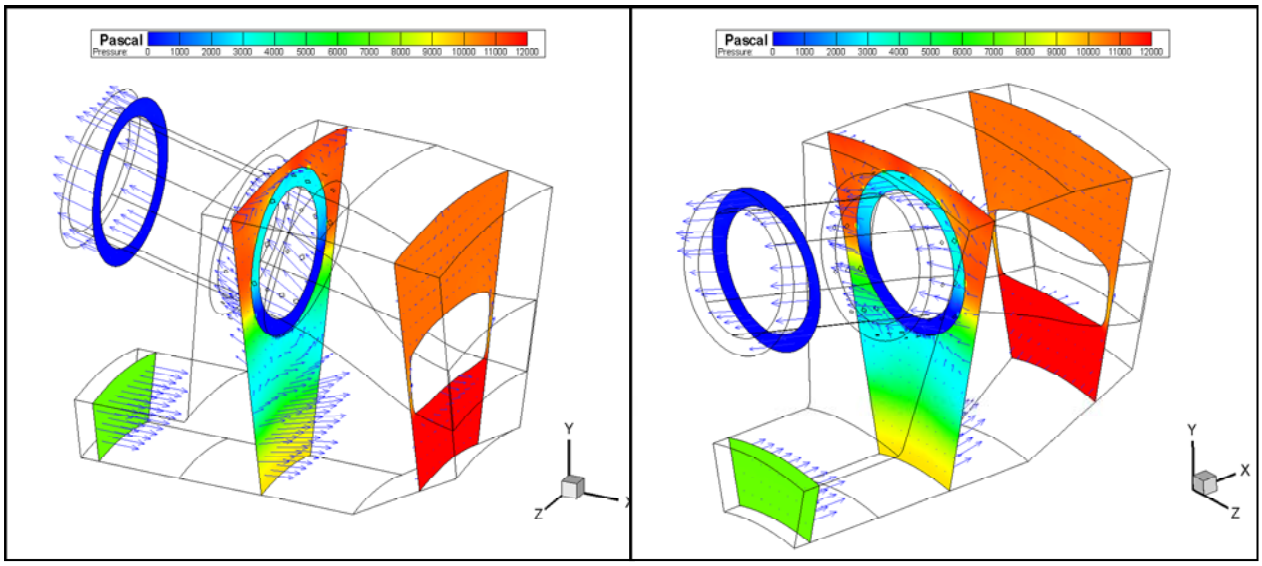

Figure 5.26 Different views of velocity vector on X- planes colored by pressure (Case 3)

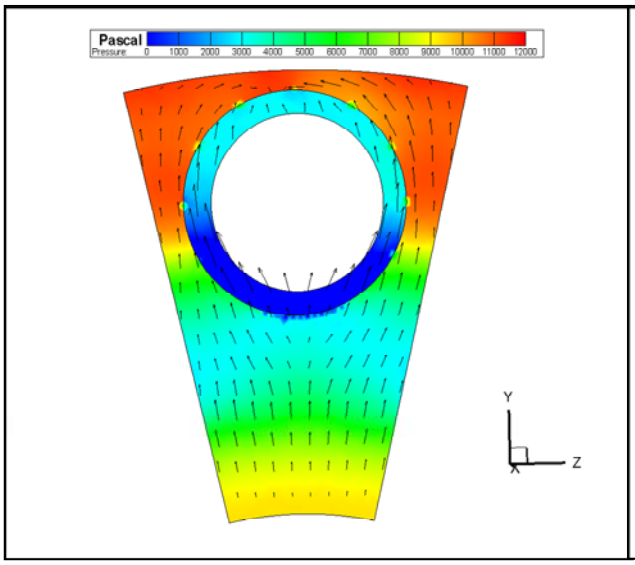

Figure 5.27 X=0 plane velocity profile with colored pressure contour (Case 3)

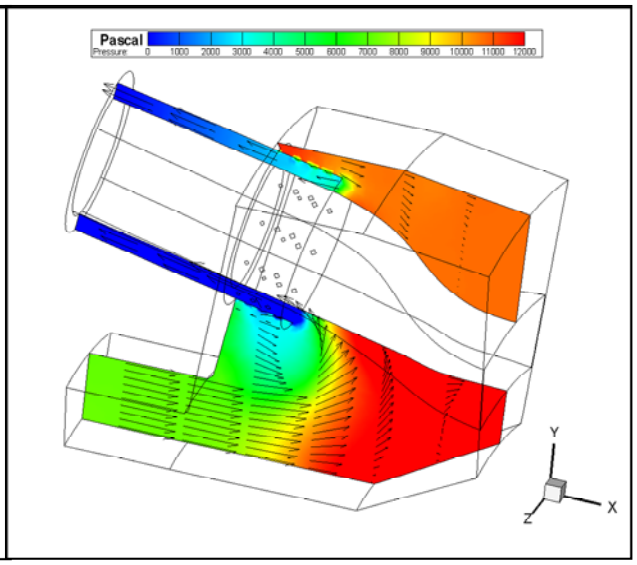

Figure 5.28 Z=0 plane velocity profile with colored pressure contour (Case 3)

Velocity vector profiles colored by static pressure are shown in different 2-D planes in Figs. 5.26 - 5.28. Larger pressure variations can be seen in the elevated condition (Case 3) than at lower pressure condition in Case 1 (Figs. 5.4 - 5.7). The temperature distribution on the combustor chamber and transitional piece walls and inside the dump-diffuser is shown in Fig

5.29. The constant heat flux (300,000 W/m^2) is placed as the boundary condition for the elevated condition case. This heat flux amount is estimated from information taken from a real gas turbine's running condition (see Appendix B).

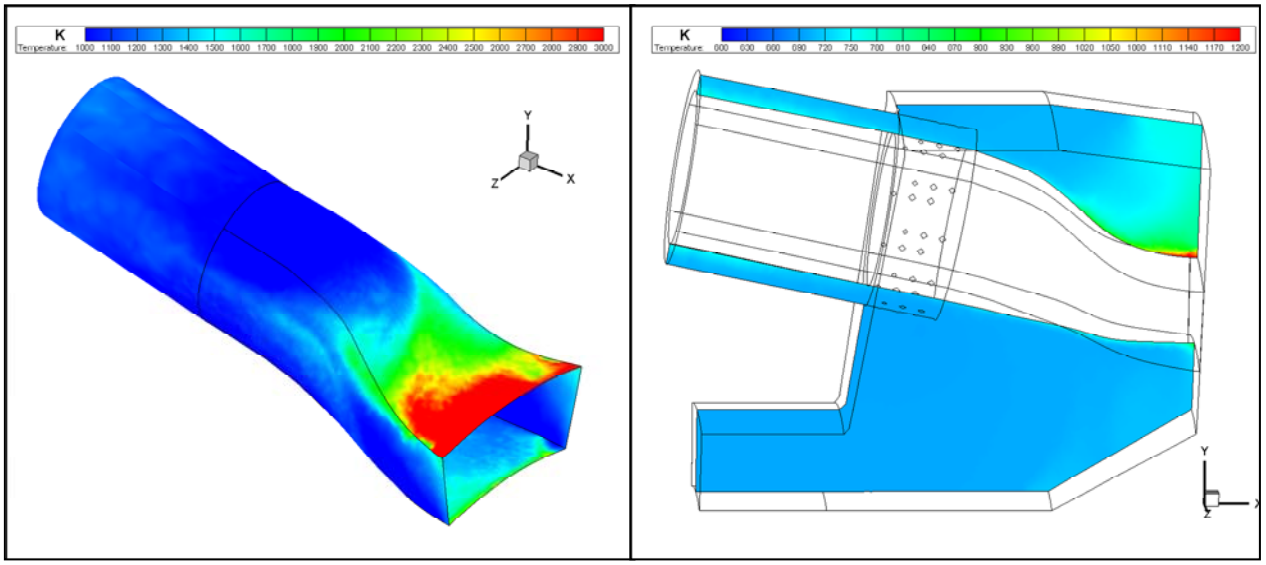

(a) **(b)**

Figure 5.29 (a) Temperature distributions on mid-chamber and transitional piece walls (b) Temperature distributions in the dump diffuser around the combustor for Case 3 (elevated gas turbine condition, no-sheath)

5.1.8 Case 6 (elevated gas turbine condition, sheathed)

To investigate the difference of aerodynamic and thermodynamic behaviors between employing a sheath and without a sheath, Case 6 is set up to compare with Case 3. The 3-D computational model with-sheath is shown in Fig 5.30. Pressure distribution on the chamber and transitional pieces is shown in Fig 5.31. Many small circles of high pressure areas are directly associated with the stagnation region of impingement jets.

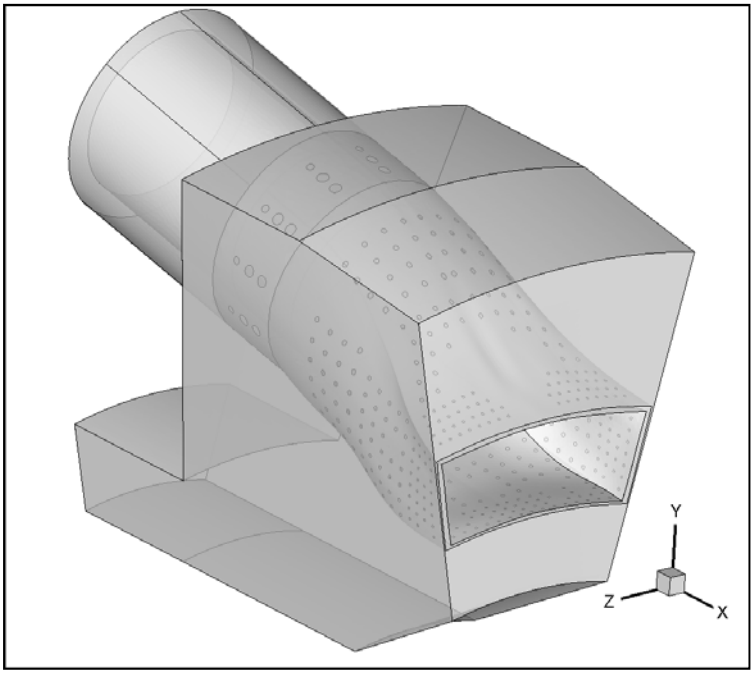

Figure 5.30 3-D model for elevated real gas turbine operating conditions with a 1/14th computational domain with sheath by employing periodic wall condition (Case 6)

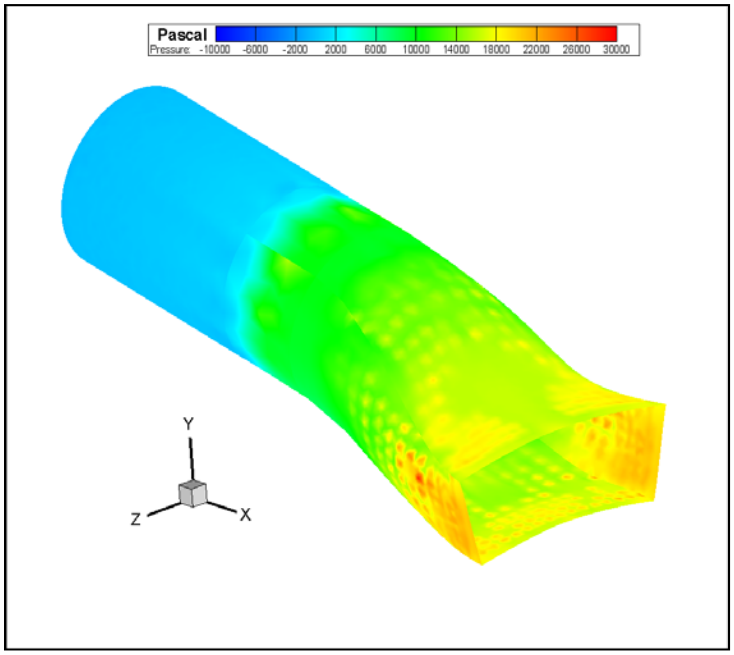

Figure 5.31 Static pressure contour (Case 6)

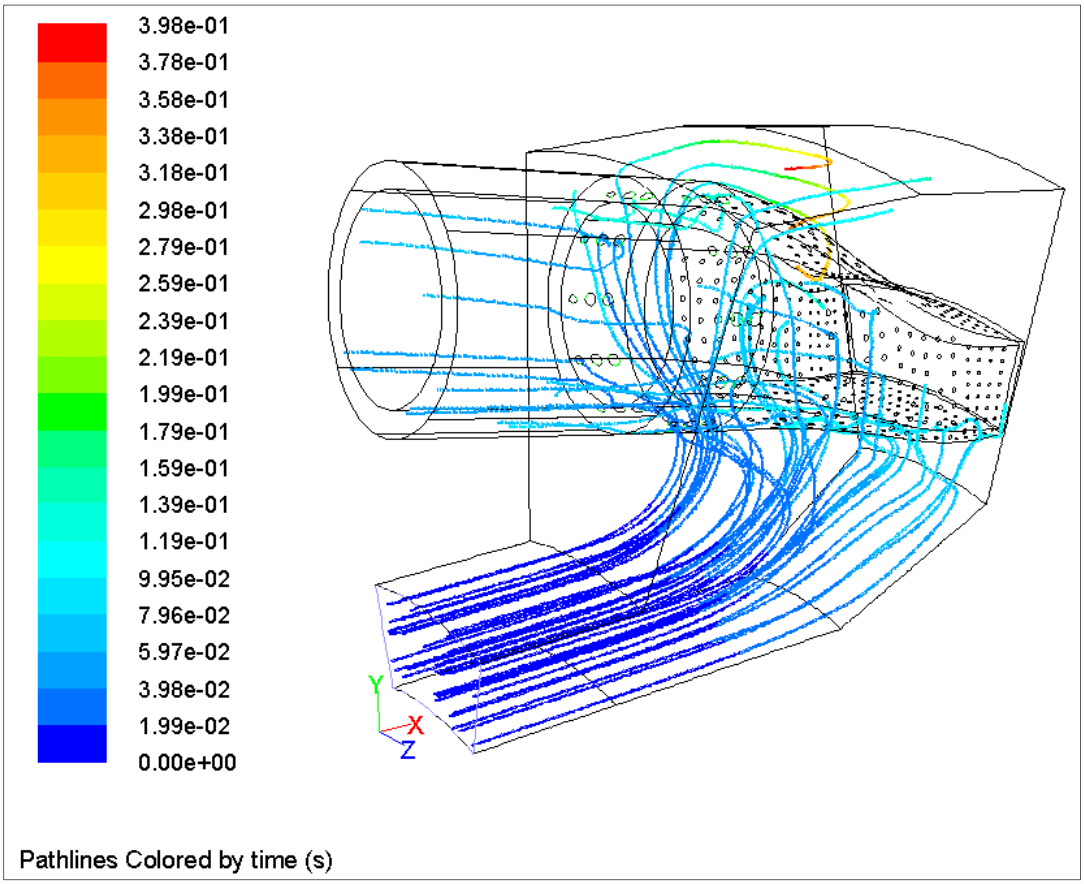

Figure 5.32 Representative pathlines (Case 6)

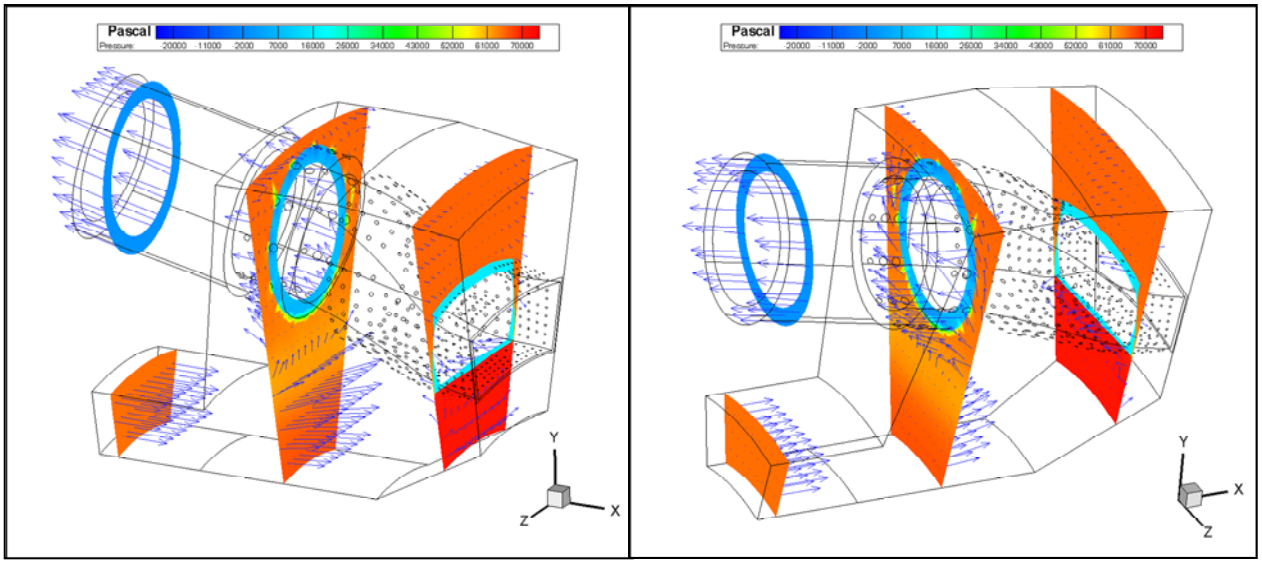

Figure 5.33 Velocity vectors on different X-direction planes colored by static pressure (Case 6)

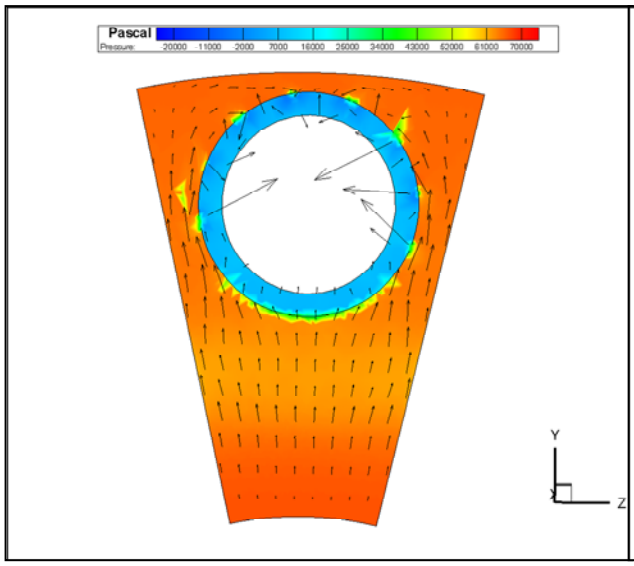

Figure 5.34 X=0 plane velocity profile with colored pressure contour (Case 6)

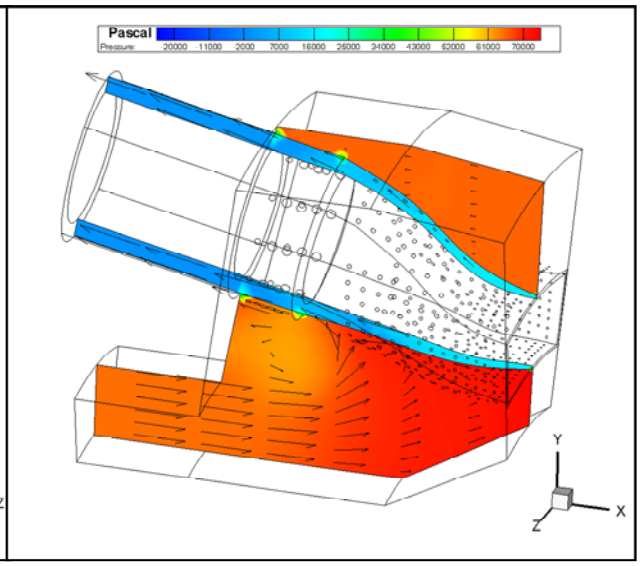

Figure 5.35 Z=0 plane velocity profile with colored pressure contour (Case 6)

Velocity vector profiles colored by static pressure are shown in different planes in Figs. 5.33 - 5.35. Due to the flow resistance induced by the sheath, the flow coming out of the compressor discharge in Fig. 5.35 does not immediately turn backwards in the dump diffuser; however in Fig. 5.28, most of the flow turns backward into the combustor sleeve instead of diffusing (ie. slows down and gains pressure) further in the dump diffuser. The static pressure distribution of Case 6 (Figs. 3.33 -3.35) is apparently with higher values than in Case 5 (Figs. 5.26 – 5.28).

The temperature distributions on chamber and transitional piece walls and inside dump-diffuser are shown in Fig 5.36. The constant heat flux (300,000 W/m^2) put on chamber and transitional piece walls is calculated by using an elevated gas turbine condition (see Appendix B).

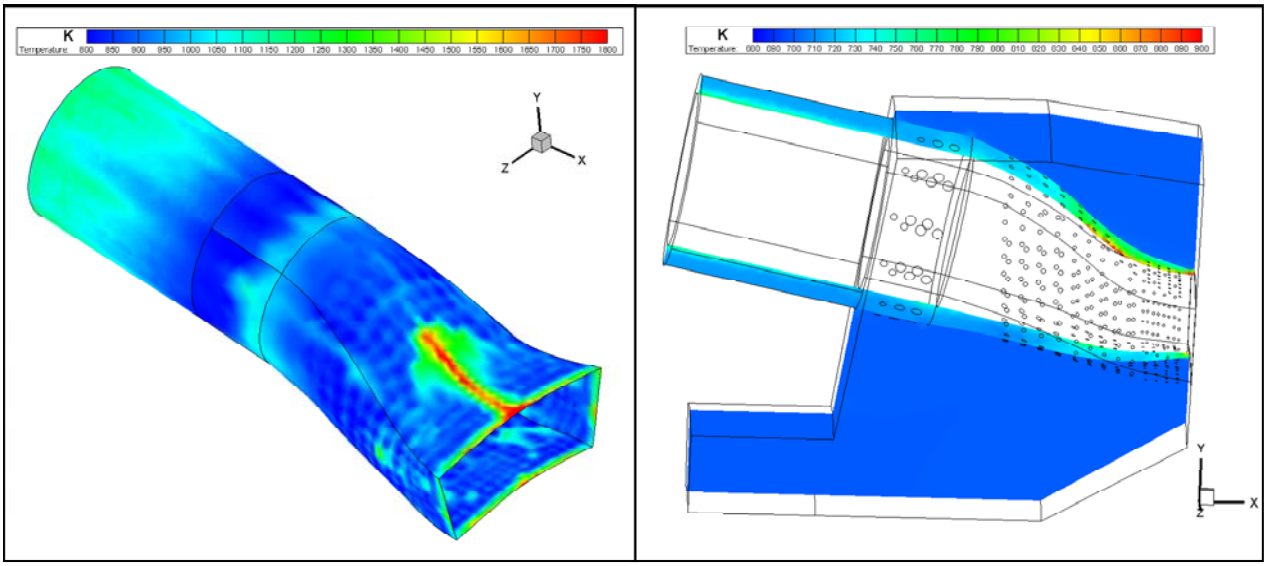

(a) **(b)**

Figure 5.36 (a) Temperature distributions on mid-chamber and transitional piece walls (b) Temperature distributions in the dump diffuser around the combustor for Case 6 (elevated gas turbine condition, sheathed)

5.1.9 Case 3 (elevated, no-sheath) versus Case 6 (elevated, sheathed)

To make a comparison between Case 3 and Case 6, the same global color scale is used for both Cases in Fig. 5.37 for pressure and Fig. 5.38 for temperature. The pressure losses of the sheathed case are 3.74% of the total pressure versus only 0.6% in the no-sheath case. From the temperature distribution comparison in Fig. 5.38, employing the sheath provides significant cooling enhancement.

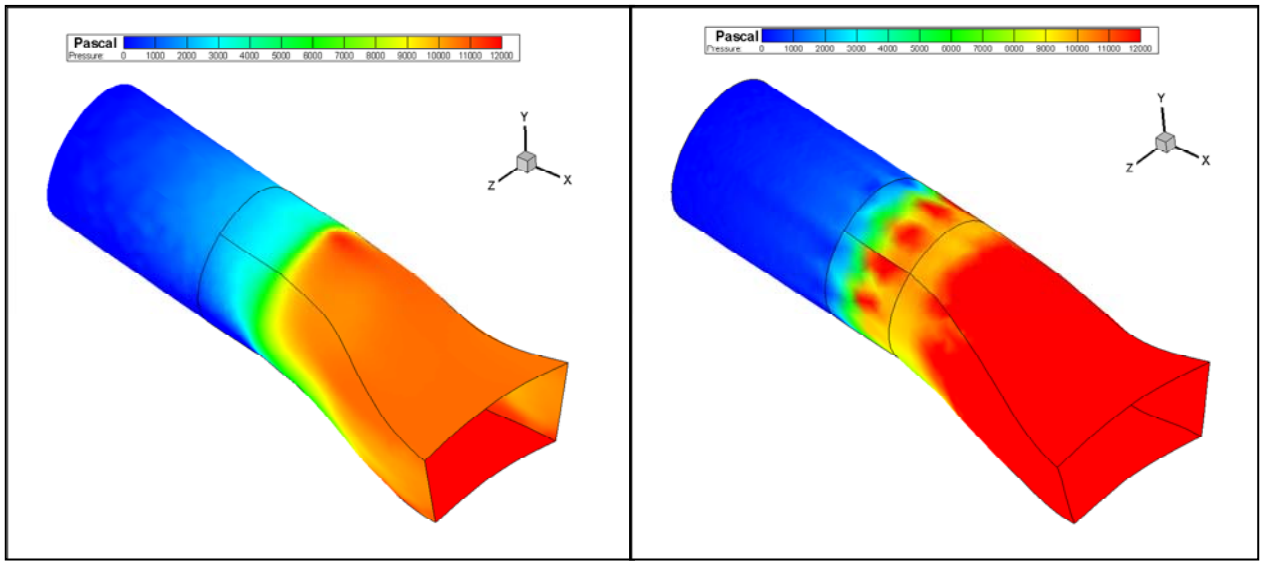

(a) Case 3 **(b) Case 6**

Figure 5.37 Comparison of pressure distribution between Case 3 (elevated, no-sheath,) and Case 6 (elevated, sheathed)

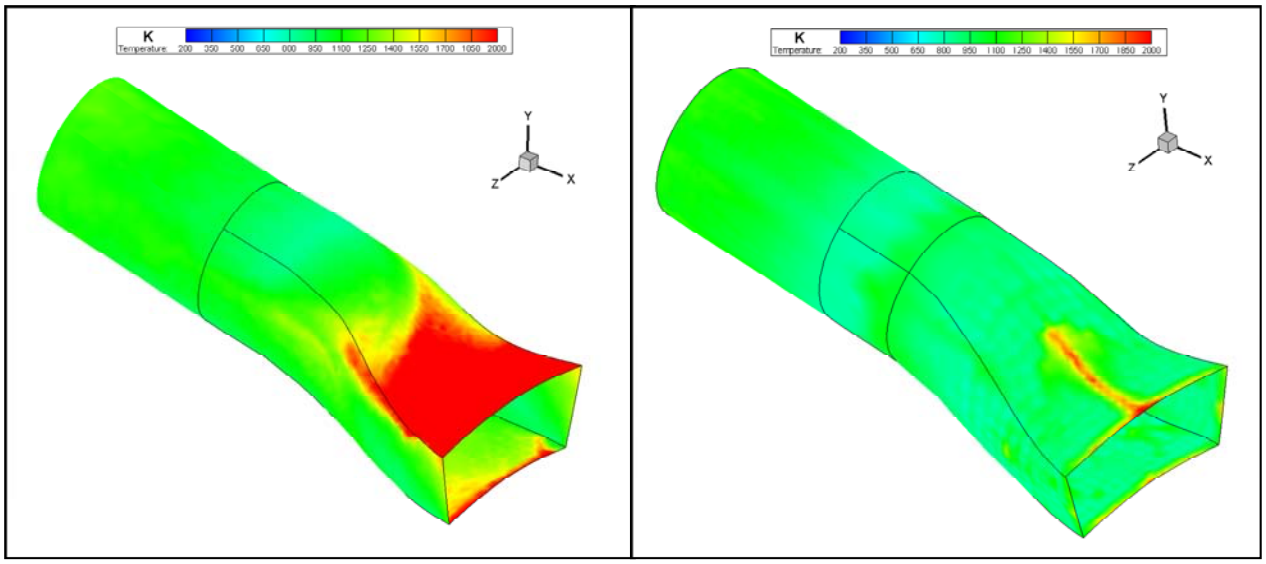

(a) Case 3 **(b) Case 6**

Figure 5.38 Comparison of temperature distribution between Case 3 (elevated, no-sheath,) and Case 6 (elevated, sheathed)

CHAPTER SIX

CONCLUSIONS

In this study, both experimental and computational models of a gas turbine dump-diffuser and reverse-flow combustor assembly have been simulated. Four experimental cases and six computational cases have been conducted. The objective is to investigate whether it is possible to remove the cooling sheath to recover pressure losses without subjecting the combustor chamber and transitional piece walls to detrimental high temperature heating. The results are summarized below.

6.1 Experiment Cases

6.1.1 Laboratory condition, fluid mechanics study only

For the no-sheath case, the total pressure difference between inlet and exit is 1200 Pascal (0.174psi), which is 1.15% of the absolute total inlet pressure. For the sheathed case, the total pressure difference between inlet and exit is 2000 Pascal (0.29 psi), which is 1.9% of the absolute total inlet pressure. The average pressure difference from the local pressure measurements over the combustor and transition piece surface shows a similar value of pressure difference.

6.1.2 Laboratory condition, heat transfer study

For the no-sheath case, the highest temperature on the mid-chamber is 315K (107°F); for the sheathed case, the highest temperature on the mid-chamber is 311K (100°F). The highest

temperature difference between sheathed and no-sheath cases is 10K (18°F). The temperature difference in most area is between 3~ 5K (5.4~9°F).

6.2 Computational Cases

6.2.1 Laboratory condition CFD simulation, fluid mechanics study only

For the CFD no-sheath case, the mass-weighted average total pressure difference between inlet and exit is 1,236 Pascal (0.179 psi), which is 1.19% of the absolute total inlet pressure. These values are 1,958 Pascal (0.284 psi) and 1.89% respectively for sheathed case and are very close to the experimental data.

6.2.2 Laboratory condition CFD simulation, heat transfer study

For the CFD no-sheath case, the highest temperature on the mid-chamber is 334K (141°F); for the sheathed case, the highest temperature on the mid-chamber is 329K (132°F). The highest temperature difference is 20K (36°F). In most area, the temperature difference is in the range of 5~10K (9 ~19°F). Since the CFD's thermal boundary condition is different from the experimental cases, the CFD results can't be compared quantitatively with the experimental case. However, it is comfortable to see that the CFD results show that the highest temperature and the average temperature differences between sheathed and no-sheathed cases are both about twice the values of the experimental data.

6.2.3 Real gas turbine condition simulation

The simulation of elevated conditions in real gas turbine environment shows the highest temperature on the mid-chamber wall is 1370K (2006°F) for no-sheath case and 1160K (1628°F) for sheathed case. The sheath provides a significant cooling enhancement over 210K (378°F). However, the pressure losses of the sheathed case are 3.74% of the total pressure versus of 0.6% in the no-sheath. In summary, removing the sheath can harvest a significant pressure recovery of approximately 3% of the total pressure, but it will subject wall temperature increase of about 200K (360°F) on combustor and transition pieces. Unless advanced materials can tolerate the significant wall temperature increment, removing the sheath is not recommended.

6.3 Future work

The following future work is recommended:

- Use finer meshes with smaller near-wall meshes (low first mesh Y+ value)
- Simulate conjugate force convection boundary condition instead of uniform heat flux in the CFD model or conduct experiment with uniformly heated walls.

REFERENCES

1. Kapat, J.S., Wang, T., Ryan, W.R., and Diakunchak, I.S., and Bannister, R.L., "Experimental Studies of Air Extraction for Cooling and/or Gasification in Gas Turbine Applications," ASME Journal of Gas Turbine and Power, Vol. 119, pp. 807-814, 1997.

2. Wang, T., Kapat, J.S., Ryan, W.R., and Diakunchak, I.S., and Bannister, R.L., "Effect of Air Extraction for Cooling and/or Gasification on Combustor Flow Uniformity," ASME Journal of Engineering for Gas Turbines and Power, Vol. 121, No.1, pp. 46-54, 1999.

3. Zhou, D., Wang, T., and Ryan, W.R., "Cold Flow Computations for the Diffuser-Combustor Section of an Industrial Gas Turbine," ASME paper 96-GT-513 presented at the ASME 1996 International Gas Turbine and Aeroengine Congress, Biringham. U.K. June 1996.

4. Kapat, J.S., Wang, T., Ryan, W.R., Diakunchak, I.S., and Bannister, R., "Cold Flow Experiments in a Sub-Scale Model of the Diffuser-Combustor Section of an Industrial Gas Turbine," ASMEA paper 96-GT-518 presented at the ASME 1996 International Gas Turbine and Aeroengine Congress, Biringham, U.K. June 1996.

5. Kapat, J.S., Wang, T., Ryan, W.R., and Diakunchak, I.S., and Bannister, R.L., "Experimental Studies of Air Extraction for Cooling and/or Gasification in Gas Turbine Applications," ASME paper 96-TA-10, presented at the ASME Turbo Expo'96 Asia, Jakarta, Indonesia, November 1996.

6. Wang, T., Kapat, J.S., Ryan, W.R., and Diakunchak, I.S., and Bannister, R.L., "Effect of Air Extraction for Cooling and/or Gasification on Combustor Flow Uniformity," ASME paper 98-GT-102, presented at the ASME Turbo Expo'98, Stockholm, Sweden, 1998.

7. J. Ramachandran and M.C. Conway, “MS6001FA – an advanced-technology 70-MW class 50/60... Hz gas turbine,” GER-3765B, GE Energy, 1996.

8. Timothy G. and Thomas B., “Uprate Options for the MS7001 Heavy Duty Gas Turbine,” GER-3808C, GE Energy, 2006.

9. Brandt, D.E., and Wesorick, R.R., “GE Gas Turbine Design Philosophy,” GER-3434D, GE Energy, August 1944.

10. Brooks, F.J., “GE Gas Turbine Performance Characteristics,” GER-3567E, GE Energy, August 1994.

11. Johnston, J.R., Robert, “Performance and Reliability Improvements for Heavy-Duty Gas Turbines,” GER-3571E, GE Energy, August 1994.

12. Junge, R.M., “The MS7001E Heavy-Duty Gas Turbine,” Gas Turbine Engineering and Manufacturing Department, Gas Turbine Division, Schenectady, NY, 1979.

13. Kelley, L.A., Luessen, H.P., “Uprate Options for the MS7001 and MS9001 Gas Turbines,” GER-3667, GE Energy, 1991.

14. Kelley, L.A., Luessen, H.P., “Uprate Options for the MS7001 and MS9001 Gas Turbines,” GER-3667, GE Energy, 1991.

15. Eldrid, R., Marks, P., “Continuing Evolution of F Technology” Dec 1999.

16. Eric G., “The F Technology Experience Story,” GER 3950C, GE Energy. 2000.

17. Frank. P and David P., “Fundamentals of heat and mass transfer” Fourth Edition, 2001.

18. Frank M. W., “Fluid Mechanics” Fifth Edition, 2003.

APPENDIX A

ESTIMATE OF THE HEATING POWER NEEDED TO EXERIMENTAL TEST RIG

Problem Description:

To simulate the heat release from the combustor, it is decided to employ a forced convective heat transfer scheme in the mock combustor chamber for the test rig. This forced scheme is deemed more closely simulating the combustion heat release than using the conventional experimental method of providing a uniformly heated surface or a constant temperature surface. The task is to estimate the heat energy to be provided so the test surface temperature will not be higher than 66^{o}C (150^{o}F).

Approach:

Since the flow pattern surrounding the combustor and the transitional piece is very complicated, the heat load calculation is simplified by first using a flow moving perpendicular to a cylinder, followed employing flow moving parallel to the cylinder. The results of these two flow condition are compared and an average is taken as the estimated value.

Case 1: Flow moves perpendicual to a cylinder (cross flow condition)

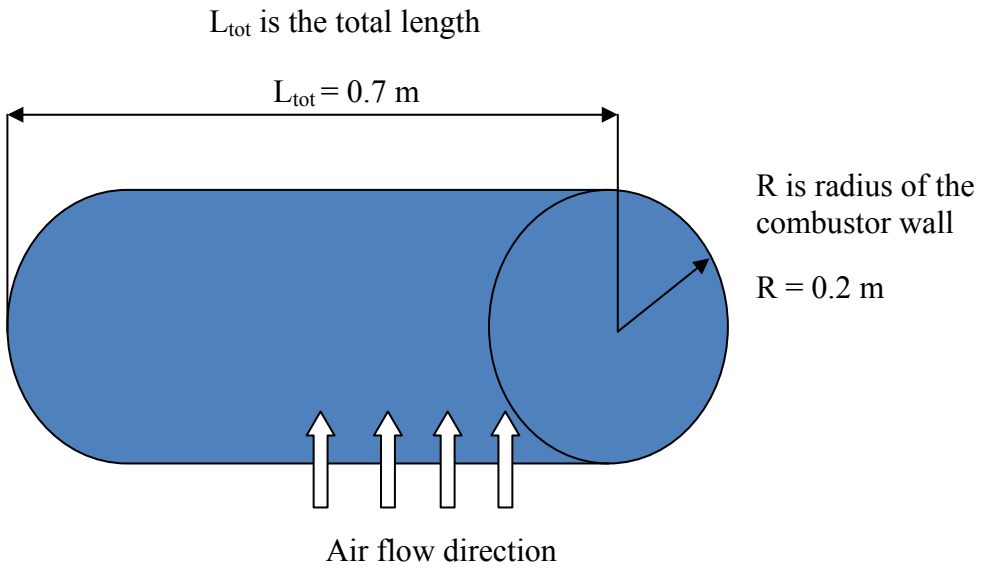

Figure A-1 Schematic diagram of air flow moves perpendicular to a cylinder to simulate the cross flow passing through the combustion chamber and the transition piece

Assumptions:

1. The geometry of the combustor chamber and transitional piece is cylinder, as showing in Fig.A-1.
2. The volumetric flow rate is Q_{air} = 6 m^3 /s and flow direction is perpendicular to the cylinder.
3. The inner wall temperature is limited to T_{in}=150^{o}F to avoid distortion of the Acrylic surface. The air flow temperature is set as T_{air} =60F.
4. For simplicity, assume the air property is constant and the flow is steady state.

Calculation:

$$\mathrm{Re}_D = \frac{Q_{air} \times 2R}{\mu \times A} = \frac{6m^3/s \times 0.4m}{1.5\times10^{-5} m^2/s \times 2\pi RL_{tot}} = \frac{6m^3/s \times 0.4m}{1.5\times10^{-5} m^2/s \times 2 \times \pi \times 0.2m \times 0.7m} = 1.8\times10^5$$

$$\mathrm{Pr}_{air} = 0.7$$

$$Nu_D = 0.3 + \frac{0.62\,\mathrm{Re}_D^{\frac{1}{2}}\,\mathrm{Pr}^{\frac{1}{3}}}{\left[1+\left(\frac{0.4}{\mathrm{Pr}}\right)^{\frac{2}{3}}\right]^{\frac{1}{4}}}\left[1+\left(\frac{\mathrm{Re}_D}{282000}\right)^{\frac{5}{8}}\right]^{\frac{4}{5}} = 321$$

The heat transfer coefficient can be calculated as:

$$h = \frac{Nu_D \times k}{2R} = \frac{321 \times 0.025 W/m \cdot K}{0.4m} = 20 W/m^2 \cdot K$$

$$Q = h \times A \times \Delta T = 20 \times 2\pi \times 0.2 \times 0.7 \times (150 - 60) = 1.58 kW$$

Case 2: Flow moves in parallel with a cylinder

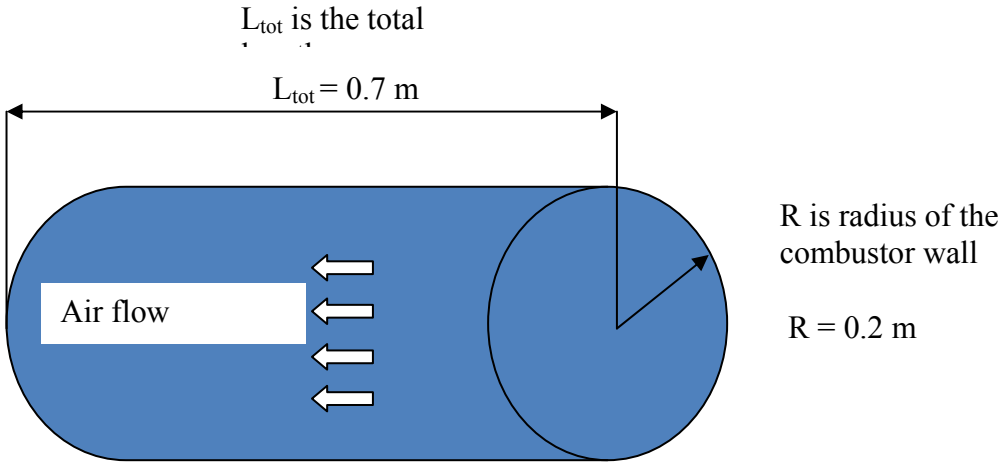

Figure A-2 Schematic diagram of air flow moves in parallel with the combustion chamber and the transitional piece

Assumptions are the same as in Case 1.

Calculation:

$$\mathrm{Re}_x = \frac{Q_{air} \times L_{tot}}{\mu \times 2\pi R \times L_{tot}} = \frac{6 \times 0.7}{1.5 \times 10^{-5} \times 2 \times 0.2 \times \pi \times 0.7} = 3.18 \times 10^5$$

$$Nu_x = 0.0296 \mathrm{Re}_x^{\frac{4}{5}} \mathrm{Pr}^{\frac{1}{3}} = 663$$

The heat transfer coefficient is: $h = \frac{Nu_x \times k}{L_{tot}} = \frac{663 \times 0.025 W/m \cdot K}{0.7m} = 23.7 W/m^2 \cdot K$

$$Q = h \times A \times \Delta T = 23.7 \times 2\pi \times 0.2 \times 0.7 \times (150 - 60) = 1.88 kW$$

The calculated results from both cases are very close, which makes the estimate more acceptable. A heat gun of 1.5kW is then used to provide the heat in the mock combustor.

Reference:

The Nusselt number for case 1 can be obtained from Eq.7.57 and Nusselt number for case 2 can be obtained from Eq.7.37 in "Fundamentals of heat and mass transfer" Fourth Edition (1996)

Frank P. Incropera and David P. Dewitt "Fundamentals of heat and mass transfer, Fourth Edition,." John Wilet & Sons, 1996

APPENDIX B

HEAT FLUX ESTIMATION FOR ELEVATED CONDITIONS

Problem Description:

To provide an adequate thermal boundary condition on the combustor and transitional walls under elevated gas turbine operating conditions, the heat flux goes through the walls are estimated in this appendix.

Step One: calculate the convection heat transfer coefficient

Case 1:

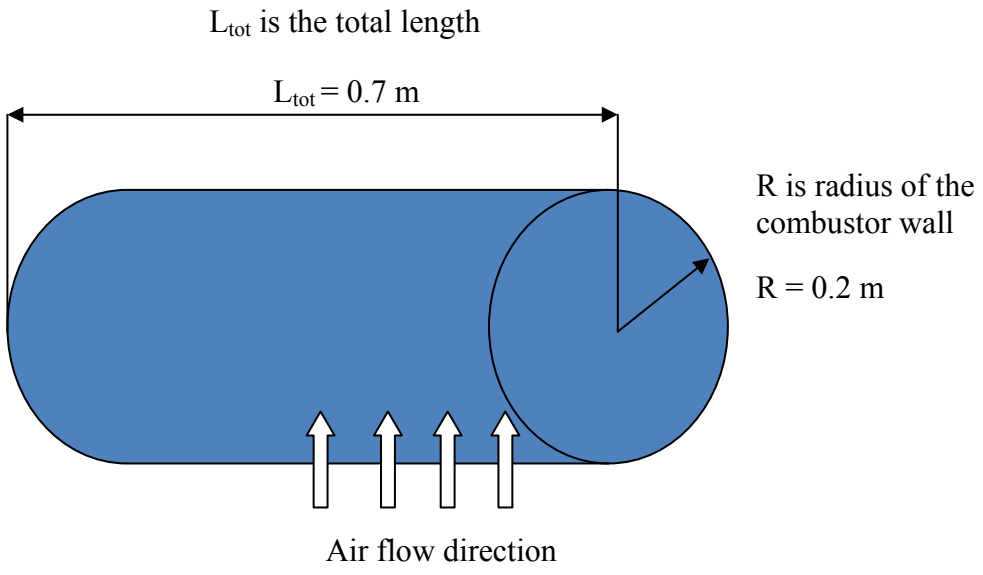

Figure B-1 Schematic diagram of air flow moves perpendicular to a cylinder to simulate the cross flow passing through the combustion chamber and the transition piece

Assumptions:

1. The geometry of the combustor chamber and transitional piece walls is cylinder, as showing in Fig.B-1.
2. The volumetric flow rate is Q_{air} = 72.7 m^3 /s and flow direction is perpendicular to the geometry. (Total mass flow rate is 445 kg/s for whole gas turbine system. There are 14 combustor chambers, so the mass flow rate for each chamber is about 32 kg/s)
3. The inner wall temperature T_{in}=3300 F (combustion flame temperature) and air flow temperature T_{air} =800F (base on the pressure ratio 16:1).
4. For simplicity, assume air property is constant and steady state.

Calculation:

$$\mathrm{Re}_D = \frac{Q_{air} \times 2R}{\mu \times A} = \frac{72.7 m^3/s \times 0.4m}{1.5\times10^{-5} m^2/s \times 2\pi R L_{tot}} = \frac{72.7 m^3/s \times 0.4m}{1.5\times10^{-5} m^2/s \times 2\times\pi\times 0.2m \times 0.7m} = 2.2\times10^6$$

$\mathrm{Pr}_{air} = 0.7$

$$Nu_D = 0.3 + \frac{0.62\,\mathrm{Re}_D^{\frac{1}{2}}\,\mathrm{Pr}^{\frac{1}{3}}}{\left[1+\left(\frac{0.4}{\mathrm{Pr}}\right)^{\frac{2}{3}}\right]^{\frac{1}{4}}}\left[1+\left(\frac{\mathrm{Re}_D}{282000}\right)^{\frac{5}{8}}\right]^{\frac{4}{5}} = 2431$$

$$h = \frac{Nu_D \times k}{2R} = \frac{2431\times 0.025 W/m\cdot K}{0.4m} = 152 W/m^2\cdot K$$

Case 2:

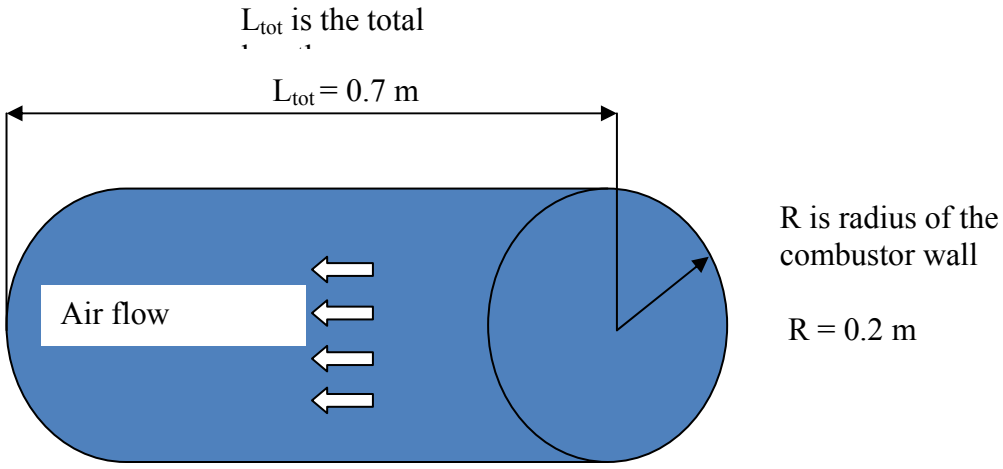

Figure B-2 Schematic diagram of air flow moves in parallel with the combustion chamber and the transitional piece

Assumptions are the same as in Case 1.

Calculation:

$$\mathrm{Re}_x = \frac{Q_{air} \times L_{tot}}{\mu \times 2\pi R \times L_{tot}} = \frac{72.7 m^3/s \times 0.7m}{1.5 \times 10^{-5} m^2/s \times 2 \times 0.2m \times \pi \times 0.7m} = 3.85 \times 10^6$$

$$Nu_x = 0.0296 \mathrm{Re}_x^{\frac{4}{5}} \mathrm{Pr}^{\frac{1}{3}} = 4875$$

$$h = \frac{Nu_x \times k}{L_{tot}} = \frac{4875 \times 0.025 W/m \cdot K}{0.7m} = 174 W/m^2 \cdot K$$

These two approaches give a similar result for the heat transfer coefficient in the range of 150~170W/m^2

Step Two: Heat flux calculation

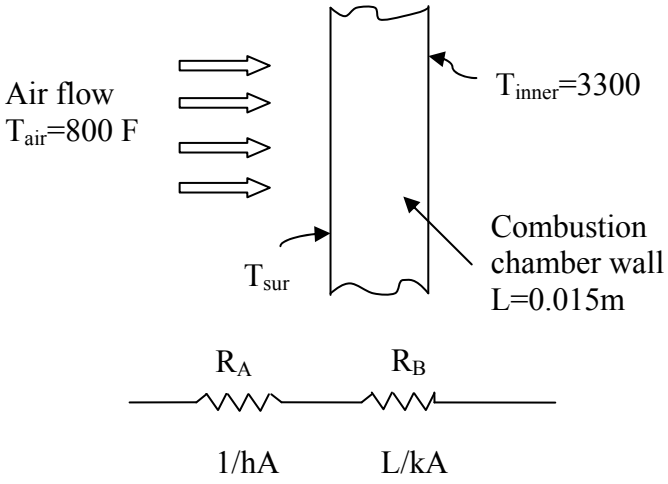

Figure B-3 Overall heat transfer through the wall and resistance analogy

T_{air}=800°F, T_{inner}=3300°F

h = 150~170W/m^2·K

k = 11.7 W/m·K

$$T_{sur} = T_{air} + \frac{(T_{inner} - T_{air})\left(\frac{1}{h}\right)}{\frac{1}{h} + \frac{L}{k}} = 800 + \frac{(3300 - 800)\left(\frac{1}{150}\right)}{\frac{1}{150} + \frac{0.015}{11.7}} = 2894°F \quad \text{(for h=150W/m}^2\text{·K)}$$

or

T_{sur}=2877°F (for h=170W/m^2·K)

Then, use T_{sur} to calculate the heat flux

$$q'' = k \times \frac{(T_{inner} - T_{sur})}{L} = 3.1 \times 10^5 \, W/m^2 \quad \text{(for } T_{sur}\text{=2894°F)}$$

or

$q'' = 3.3 \times 10^5 \, W / m^2$ (for T_{sur}=2877°F)

These two results show the range of heat flux we should put into CFD model.

Reference:

The Nusselt number for case 1 can be obtained from Eq.7.57 and Nusselt number for case 2 can be obtained from Eq.7.37 in "Fundamentals of heat and mass transfer" Fourth Edition (1996)

Thermal conductivity value can be obtained from Table A.1, Nickel Inconel X-750 in "Fundamentals of heat and mass transfer" Fourth Edition (1996)

Frank P. Incropera and David P. Dewitt "Fundamentals of heat and mass transfer, Fourth Edition,." John Wilet & Sons, 1996

APPENDIX C

LABORATORY PRESSURE MEASUREMENT DATA AND COMPARISON WITH THE CFD RESULTS

The pressure transducer's readings for both no-sheath and sheathed cases are shown in Tables C-1 and Table C-2, respectively. The upper left corner of each table shows the motor frequency at which the measurements were taken (only showing the highest speed here). The corrected voltage is obtained by either adding or subtracting the corresponding offset voltage for that particular module. The offset voltage is obtained by shorting (connecting) the low and high pressure ports to get zero pressure difference. The corrected voltages are relative to the same absolute zero reference, so all the voltages versus pressures figures would contain only the positive values.

Tables C-3 and Table C-4 document the gauge pressure of the module at the given channel locations. The low pressure ports were disconnected; therefore, open to the atmosphere during the experimental process.

Table C-1 Displayed pressure transducer voltage values (raw data) and corrected voltage values at 60Hz for the no-sheath case

60Hz	Voltage (Volt)				Corrected Voltge (Volt)			
Channel	Module 1	Module 2	Module 5	Module 6	Module 1	Module 2	Module 5	Module 6
1	5.376	4.082	4.103	2.743	5.386	4.077	4.09	2.735
2	5.147	4.102	4.054	3.849	5.157	4.097	4.041	3.841
3	5.025	4.087	4.035	4.025	5.035	4.082	4.022	4.017
4	5.195	4.136	4.186	4.069	5.205	4.131	4.173	4.061
5	5.303	4.068	4.186	4.084	5.313	4.063	4.173	4.076
6	5.2	4.117	4.103	4.035	5.21	4.112	4.09	4.027
7	5.249	4.253	4.088	4.103	5.259	4.248	4.075	4.095
8	5.054	4.19	4.162	4.176	5.064	4.185	4.149	4.168
9	4.888	4.214	4.215	3.918	4.898	4.209	4.202	3.91
10	4.844	4.141	4.103	3.908	4.854	4.136	4.09	3.9
11	4.678	4.297	4.103	4.181	4.688	4.292	4.09	4.173
12	4.468	4.019	4.137	3.639	4.478	4.014	4.124	3.631
13	4.273	4.79	4.069	4.074	4.283	4.785	4.056	4.066
14	4.126	4.947	3.952	4.006	4.136	4.942	3.939	3.998
15	4.16	4.986	4.098	4.064	4.17	4.981	4.085	4.056
16	4.009	5.03	3.991	4.02	4.019	5.025	3.978	4.012
17	4.194	4.859	4.03	4.113	4.204	4.854	4.017	4.105
18	3.984	4.681	4.049	4.064	3.994	4.676	4.036	4.056
19	4.194	3.204	4.186	4.191	4.204	3.199	4.173	4.183
20	4.072	4.029	4.152	4.03	4.082	4.024	4.139	4.022
21	4.326	3.843	3.869	4.167	4.336	3.838	3.856	4.159
22	4.287	4.126	4.03	4.035	4.297	4.121	4.017	4.027
23	4.287	4.039	4.108	4.123	4.297	4.034	4.095	4.115
24	4.268	4.126	3.839	4.137	4.278	4.121	3.826	4.129
25	4.429	4.097	4.015	4.089	4.439	4.092	4.002	4.081
26	4.468	4.053	3.947	4.03	4.478	4.048	3.934	4.022
27	4.502	4.248	4.113	4.089	4.512	4.243	4.1	4.081
28	4.302	4.004	3.937	4.054	4.312	3.999	3.924	4.046
29	4.356	3.931	4.01	4.015	4.366	3.926	3.997	4.007
30	4.36	3.462	3.932	3.962	4.37	3.457	3.919	3.954
31	4.356	4.62	4.03	4.108	4.366	4.615	4.017	4.1
32	4.429	4.693	4.054	4.137	4.439	4.688	4.041	4.129
33	4.126	4.527	4.074	3.893	4.136	4.522	4.061	3.885
34	4.434	4.673	4.064	4.142	4.444	4.668	4.051	4.134
35	4.478	N/A	4.074	4.113	4.488	N/A	4.061	4.105
36	4.331	N/A	4.083	4.118	4.341	N/A	4.07	4.11
37	4.4	N/A	4.127	4.137	4.41	N/A	4.114	4.129
38	4.39	N/A	4.181	4.108	4.4	N/A	4.168	4.1
39	4.439	N/A	4.215	3.747	4.449	N/A	4.202	3.739
40	4.326	N/A	4.132	4.118	4.336	N/A	4.119	4.11

Table C-2 Displayed pressure transducer voltage values (raw data) and corrected voltage values at 60Hz for the sheathed case

60Hz	Voltage (Volt)				Corrected Voltge (Volt)			
Channel	Module 1	Module 2	Module 5	Module 6	Module 1	Module 2	Module 5	Module 6
1	2.339	3.091	4.796	2.638	2.368	3.096	4.812	2.654
2	2.022	4.229	4.918	4.372	2.051	4.234	4.934	4.388
3	1.939	4.537	4.874	3.742	1.968	4.542	4.89	3.758
4	1.943	4.659	4.757	2.248	1.972	4.664	4.773	2.264
5	1.895	4.668	4.757	1.725	1.924	4.673	4.773	1.741
6	2.007	4.688	4.923	1.745	2.036	4.693	4.939	1.761
7	1.929	4.688	4.704	3.244	1.958	4.693	4.72	3.26
8	1.934	4.805	4.86	2.101	1.963	4.81	4.876	2.117
9	1.904	4.732	4.762	1.808	1.933	4.737	4.778	1.824
10	1.87	4.439	4.747	1.945	1.899	4.444	4.763	1.961
11	1.924	4.4	4.752	1.979	1.953	4.405	4.768	1.995
12	1.904	2.73	4.801	1.715	1.933	2.735	4.817	1.731
13	1.899	2.412	4.899	1.945	1.928	2.417	4.915	1.961
14	1.939	2.456	4.913	2.004	1.968	2.461	4.929	2.02
15	1.87	2.295	4.821	1.906	1.899	2.3	4.837	1.922
16	1.875	2.217	4.728	1.945	1.904	2.222	4.744	1.961
17	1.895	2.466	4.865	1.916	1.924	2.471	4.881	1.932
18	1.943	1.192	4.86	2.067	1.972	1.197	4.876	2.083
19	1.963	1.827	4.918	1.935	1.992	1.832	4.934	1.951
20	1.865	1.914	4.801	1.794	1.894	1.919	4.817	1.81
21	4.776	1.797	3.912	4.606	4.805	1.802	3.928	4.622
22	4.917	1.9	4.215	4.992	4.946	1.905	4.231	5.008
23	4.478	1.787	3.434	4.777	4.507	1.792	3.45	4.793
24	2.07	1.88	1.617	4.899	2.099	1.885	1.633	4.915
25	1.904	1.861	1.461	4.884	1.933	1.866	1.477	4.9
26	1.968	1.973	1.959	5.016	1.997	1.978	1.975	5.032
27	1.899	1.841	2.75	4.626	1.928	1.846	2.766	4.642
28	1.997	1.978	1.979	4.85	2.026	1.983	1.995	4.866
29	1.953	1.939	1.993	4.787	1.982	1.944	2.009	4.803
30	1.86	1.914	2.333	4.675	1.889	1.919	2.349	4.691
31	1.914	1.953	2.013	4.914	1.943	1.958	2.029	4.93
32	1.846	1.861	1.891	4.718	1.875	1.866	1.907	4.734
33	1.846	1.88	1.935	4.738	1.875	1.885	1.951	4.754
34	1.831	1.87	1.871	4.826	1.86	1.875	1.887	4.842
35	1.885	N/A	1.935	4.797	1.914	N/A	1.951	4.813
36	1.846	N/A	1.94	4.928	1.875	N/A	1.956	4.944
37	1.924	N/A	1.969	4.841	1.953	N/A	1.985	4.857
38	1.943	N/A	1.993	4.821	1.972	N/A	2.009	4.837
39	1.865	N/A	1.891	4.377	1.894	N/A	1.907	4.393
40	1.89	N/A	1.915	4.841	1.919	N/A	1.931	4.857

Table C-3 Combustion chamber static gauge pressure at 60Hz for no-sheath case

60HZ	Pressure Measurement (Pascal)			
Channel	Module 1	Module 2	Module 5	Module 6
1	2225.0301	1685.0414	1690.4042	1131.4396
2	2130.563	1693.2918	1670.1907	1587.6867
3	2080.2356	1687.104	1662.3528	1660.2902
4	2150.364	1707.3175	1724.6434	1678.4411
5	2194.9162	1679.2662	1724.6434	1684.6289
6	2152.4266	1699.4796	1690.4042	1664.4154
7	2172.6401	1755.5824	1684.2164	1692.4668
8	2092.1987	1729.5936	1714.7429	1722.5808
9	2023.7204	1739.4941	1736.6064	1616.1506
10	2005.5695	1709.3801	1690.4042	1612.0254
11	1937.0912	1773.7332	1690.4042	1724.6434
12	1850.462	1659.0527	1704.4299	1501.0575
13	1770.0206	1977.1056	1676.3785	1680.5037
14	1709.3801	2041.8712	1628.1137	1652.4524
15	1723.4058	2057.9595	1688.3416	1676.3785
16	1661.1153	2076.1104	1644.202	1658.2276
17	1737.4315	2005.5695	1660.2902	1696.592
18	1650.8023	1932.1409	1668.1281	1676.3785
19	1737.4315	1322.8489	1724.6434	1728.7686
20	1687.104	1663.1779	1710.6177	1662.3528
21	1791.8841	1586.4492	1593.8745	1718.8681
22	1775.7958	1703.1923	1660.2902	1664.4154
23	1775.7958	1667.3031	1692.4668	1700.7172
24	1767.958	1703.1923	1581.4989	1706.4925
25	1834.3737	1691.2292	1654.1024	1686.6915
26	1850.462	1673.0784	1626.0511	1662.3528
27	1864.4876	1753.5198	1694.5294	1686.6915
28	1781.9836	1652.8649	1621.9259	1672.2533
29	1804.2597	1622.7509	1652.0398	1656.165
30	1805.9098	1429.279	1619.8633	1634.3015
31	1804.2597	1906.9772	1660.2902	1694.5294
32	1834.3737	1937.0912	1670.1907	1706.4925
33	1709.3801	1868.6128	1678.4411	1605.8376
34	1836.4363	1928.8408	1674.3159	1708.5551
35	1854.5872	N/A	1678.4411	1696.592
36	1793.9467	N/A	1682.1538	1698.6546
37	1822.4106	N/A	1700.3047	1706.4925
38	1818.2854	N/A	1722.5808	1694.5294
39	1838.4989	N/A	1736.6064	1545.6097
40	1791.8841	N/A	1702.3673	1698.6546

Table C-4 Combustion chamber static gauge pressure at 60Hz for sheathed case

60HZ	Pressure Measurement (Pascal)			
Channel	Module 1	Module 2	Module 5	Module 6
1	980.04476	1280.3593	1988.2436	1098.0255
2	849.27592	1749.8071	2038.5711	1813.3352
3	815.03676	1876.8632	2020.4202	1553.4476
4	816.68684	1927.1907	1972.1554	937.14268
5	796.88588	1930.9034	1972.1554	721.39472
6	843.08812	1939.1538	2040.6337	729.64512
7	810.91156	1939.1538	1950.2918	1348.0126
8	812.97416	1987.4186	2014.6449	876.50224
9	800.59856	1957.3046	1974.218	755.63388
10	786.57288	1836.4363	1968.0302	812.14912
11	808.84896	1820.348	1970.0928	826.1748
12	800.59856	1131.4396	1990.3062	717.26952
13	798.53596	1000.2582	2030.7332	812.14912
14	815.03676	1018.4091	2036.5085	836.4878
15	786.57288	951.9934	1998.5566	796.06084
16	788.63548	919.81684	1960.1923	812.14912
17	796.88588	1022.5343	2016.7075	800.18604
18	816.68684	496.98384	2014.6449	862.47656
19	824.93724	758.93404	2038.5711	808.02392
20	784.51028	794.82328	1990.3062	749.8586
21	1985.356	746.55844	1623.576	1909.8648
22	2043.5213	789.048	1748.5695	2069.0976
23	1862.425	742.43324	1426.3914	1980.4058
24	869.07688	780.7976	676.84256	2030.7332
25	800.59856	772.95972	612.48944	2024.5454
26	826.99984	819.16196	817.9244	2078.998
27	798.53596	764.70932	1144.2277	1918.1152
28	838.96292	821.22456	826.1748	2010.5197
29	820.81204	805.13628	831.95008	1984.531
30	782.44768	794.82328	972.20688	1938.3287
31	804.72376	810.91156	840.20048	2036.921
32	776.6724	772.95972	789.87304	1956.0671
33	776.6724	780.7976	808.02392	1964.3175
34	770.4846	776.6724	781.62264	2000.6192
35	792.76068	N/A	808.02392	1988.6562
36	776.6724	N/A	810.08652	2042.6963
37	808.84896	N/A	822.0496	2006.807
38	816.68684	N/A	831.95008	1998.5566
39	784.51028	N/A	789.87304	1815.3978
40	794.82328	N/A	799.77352	2006.807

Table C-5 Comparison of measured experimental pressure with the CFD results (no-sheath, unheated)

	BC		MCB		MCBC		MCF	
	EXP	CFD	EXP	CFD	EXP	CFD	EXP	CFD
1	1719	1957	2225	2169	1323	1773	1685	1893
2	1664	1963	2131	2168	1663	1837	1693	1999
3	1701	1970	2080	2167	1586	2020	1687	2018
4	1706	1974	2150	2165	1703	2004	1707	1999
5	1687	1988	2195	2164	1667	2026	1679	2011
6	1662	2002	2152	2161	1703	2040	1699	2042
7	1687	2010	2173	2159	1691	2014	1756	2006
8	1672	2011	2092	2157	1673	2007	1730	2009
9	1656	2012	2024	2156	1754	2011	1739	2017
10	1634	2009	2006	2155	1653	2018	1709	2021
11	1695	1998	1937	2156	1623	1869	1774	2003
12	1706	1992	1850	2158	1429	1833	1659	1902
13	1606	1989	1770	2160	1907	2114	1977	2145
14	1709	1987	1709	2163	1937	2148	2042	2156
15	1697	1988	1723	2166	1869	2157	2058	2163
16	1699	1989	1661	2167	1929	2139	2076	2169
17	1706	1989	1737	2168			2006	2165
18	1695	1990	1651	2169			1932	2155
19	1546	1987	1737	2171				
20	1699	1984	1687	2167				

	MCL		MCR		MCT		TC	
	EXP	CFD	EXP	CFD	EXP	CFD	EXP	CFD
1	1594	1955	1131	1963	1792	2024	1690	1949
2	1660	1956	1588	1965	1776	2025	1670	1956
3	1692	1954	1660	1964	1776	2026	1662	1962
4	1581	1949	1678	1960	1768	2028	1725	1967
5	1654	1940	1685	1952	1834	2028	1725	1981
6	1626	1925	1664	1939	1850	2030	1690	1996
7	1695	1914	1692	1929	1864	2031	1684	2001
8	1622	1904	1723	1922	1782	2032	1715	2000
9	1652	1897	1616	1915	1804	2033	1737	2000
10	1620	1891	1612	1909	1806	2034	1690	1999
11	1660	1887	1725	1903	1804	2035	1690	1991
12	1670	1878	1501	1895	1834	2035	1704	1989
13	1678	1864	1681	1890	1709	2036	1676	1988
14	1674	1855	1652	1886	1836	2036	1628	1988
15	1678	1847	1676	1884	1855	2035	1688	1989
16	1682	1841	1658	1886	1794	2035	1644	1988
17	1700	1838	1697	1892	1822	2034	1660	1985
18	1723	1862	1676	1912	1818	2033	1668	1985
19	1737	1899	1729	1942	1838	2031	1725	1987
20	1702	1932	1662	1968	1792	2028	1711	1986

*Pressure unit is Pascal

Table C-6 Comparison of measured experimental pressure with the CFD results (sheathed, unheated)

	BC		MCB		MCBC		MCF	
	EXP	CFD	EXP	CFD	EXP	CFD	EXP	CFD
1	1910	2142	980	962	759	907	1280	1021
2	2069	2133	849	958	795	865	1750	2153
3	1980	2131	815	947	747	798	1877	2238
4	2031	2138	817	965	789	804	1927	2215
5	2025	2147	797	955	742	773	1931	2302
6	2079	2150	843	937	781	774	1939	2314
7	1918	2150	811	914	773	777	1939	2276
8	2011	2149	813	899	819	775	1987	2294
9	1985	2149	801	882	765	802	1957	2217
10	1938	2149	787	871	821	803	1836	2339
11	2037	2149	809	869	805	901	1820	2053
12	1956	2149	801	865	795	913	1131	1005
13	1964	2149	799	853	811	975	1000	1027
14	2001	2150	815	846	773	890	1018	957
15	1989	2150	787	831	781	898	952	951
16	2043	2150	789	825	777	939	920	943
17	2007	2150	797	820			1023	952
18	1999	2150	817	765			497	963
19	1815	2150	825	745				
20	2007	2150	785	681				

	MCL		MCR		MCT		TC	
	EXP	CFD	EXP	CFD	EXP	CFD	EXP	CFD
1	1624	1028	1098	1022	1985	813	1988	2139
2	1749	1027	1813	1015	2044	801	2039	2128
3	1426	2316	1553	2326	1862	791	2020	2128
4	677	2198	937	2236	869	790	1972	2138
5	612	2261	721	2299	801	788	1972	2146
6	818	2348	730	2350	827	787	2041	2148
7	1144	2343	1348	2345	799	786	1950	2148
8	826	2344	877	2348	839	784	2015	2148
9	832	2347	756	2351	821	780	1974	2148
10	972	2210	812	2211	782	775	1968	2148
11	840	772	826	778	805	770	1970	2148
12	790	693	717	707	777	764	1990	2148
13	808	672	812	704	777	758	2031	2148
14	782	689	836	683	770	749	2037	2148
15	808	663	796	632	793	728	1999	2148
16	810	646	812	638	777	716	1960	2148
17	822	681	800	656	809	696	2017	2148
18	832	785	862	732	817	680	2015	2149
19	790	645	808	648	785	677	2039	2149
20	800	654	750	648	795	683	1990	2149

*Pressure unit is Pascal

APPENDIX D

EXPERIMENTAL TEMPERATURE DATA AND COMPARISON WITH THE CFD RESULTS

Besides 80 thermocouples installed in the combustor and transition piece walls, four additional thermocouples are used to measure other reference temperatures. The first one is located in the rectangular-to-circular transition section upstream of the test section; the second one is located near the test section exit; and the third one is put inside the combustion chamber. These three thermocouples are used to measure the variation of air flow temperature at specific locations. The forth thermocouple is dipped into the ice bath to measure the temperature difference between isothermal box and the ice bath. Tables D-1 and Table D-2 are thermocouple measured raw data in microvolts on middle-chamber for no-sheath case and sheathed case respectively. The corrected voltage is calculated by adding the corresponding temperature difference between the isothermal box and the ice bath temperature. The corrected raw data in microvolts are then converted to temperature in Celsius or Kelvin. Fig.D-1. shows the calibration curve for converting from millivolts to Celsius in temperature. The curve is generated by interpolating the “E type” thermocouples’ manufacture table which also shows temperature versus millivolts relationship.

Table D-1 Experimental thermocouple data (μV) for no-sheath case

Original	TR	TMR	TML	TL	L	BL	BR	R
1	589.09	927.25	978.91	608.76	794.43	882.28	1148.43	552.31
2	655.32	821.09	882.14	1194.87	780.11	769.96	813.23	561.72
3	760.60	860.48	850.55	1167.16	751.32	699.56	742.02	682.07
4	774.20	850.25	859.06	581.58	738.88	720.71	767.90	731.47
5	801.41	842.94	837.33	690.45	729.57	741.87	760.80	740.48
6	815.01	835.64	793.88	799.32	721.47	727.80	746.73	741.34
7	791.40	831.32	772.15	781.45	741.50	710.79	738.83	767.94
8	764.76	827.00	789.79	732.80	717.84	719.17	730.93	763.29
9	738.13	750.33	766.77	699.25	745.95	697.57	713.23	724.40
10	705.02	737.37	712.62	704.27	636.18	675.57	677.34	685.51
upstream	544.97							
downstream	535.97							
inside	1187.14							
refference	1350.33							

Corrected	TR	TMR	TML	TL	L	BL	BR	R
1	1939.42	2277.58	2329.24	1959.09	2144.75	2232.61	2498.75	1902.63
2	2005.64	2171.41	2232.46	2545.20	2130.43	2120.28	2163.55	1912.05
3	2110.93	2210.80	2200.87	2517.49	2101.64	2049.88	2092.35	2032.40
4	2124.53	2200.57	2209.38	1931.91	2089.20	2071.04	2118.23	2081.80
5	2151.73	2193.27	2187.66	2040.78	2079.90	2092.20	2111.13	2090.81
6	2165.34	2185.97	2144.21	2149.64	2071.80	2078.13	2097.05	2091.67
7	2141.72	2181.65	2122.48	2131.78	2091.82	2061.12	2089.16	2118.27
8	2115.09	2177.33	2140.12	2083.12	2068.16	2069.50	2081.26	2113.62
9	2088.46	2100.66	2117.10	2049.58	2096.28	2047.89	2063.56	2074.72
10	2055.35	2087.70	2062.95	2054.59	1986.50	2025.89	2027.66	2035.83
upstream	1895.30							
downstream	1886.29							
inside	2537.47							

Table D-2 Experimental thermocouple data (μV) for sheathed case

Original	TR	TMR	TML	TL	L	BL	BR	R
1	763.92	932.76	722.65	805.04	744.63	646.83	656.02	524.98
2	613.65	743.27	803.53	781.64	723.31	697.54	720.34	490.82
3	578.48	913.70	761.63	720.97	747.26	687.17	628.05	587.56
4	609.34	820.63	774.23	523.15	730.19	641.67	664.26	633.00
5	671.05	765.11	758.46	637.90	718.28	596.17	658.42	607.64
6	701.91	709.59	726.92	752.66	691.69	640.71	663.89	699.55
7	673.97	703.94	711.16	708.24	705.24	640.73	662.49	695.52
8	680.03	698.30	693.05	663.48	694.34	649.71	661.08	673.48
9	686.09	680.89	711.78	653.66	726.03	683.93	672.69	666.35
10	667.56	701.82	676.64	646.84	646.51	693.55	687.12	659.21
upstream	500.08							
downstream	485.16							
inside	1169.18							
refference	1323.26							

Corrected	TR	TMR	TML	TL	L	BL	BR	R
1	2087.18	2256.02	2045.92	2128.30	2067.89	1970.09	1979.28	1848.24
2	1936.91	2066.53	2126.79	2104.90	2046.58	2020.80	2043.60	1814.09
3	1901.74	2236.96	2084.89	2044.23	2070.52	2010.43	1951.32	1910.82
4	1932.60	2143.89	2097.49	1846.41	2053.45	1964.93	1987.52	1956.26
5	1994.31	2088.37	2081.72	1961.17	2041.54	1919.43	1981.68	1930.90
6	2025.17	2032.85	2050.19	2075.92	2014.95	1963.97	1987.15	2022.81
7	1997.23	2027.21	2034.42	2031.50	2028.50	1963.99	1985.75	2018.78
8	2003.29	2021.56	2016.31	1986.75	2017.60	1972.97	1984.35	1996.75
9	2009.35	2004.15	2035.04	1976.92	2049.29	2007.19	1995.96	1989.61
10	1990.82	2025.08	1999.91	1970.10	1969.77	2016.81	2010.38	1982.47
upstream	1823.34							
downstream	1808.42							
inside	2492.44							

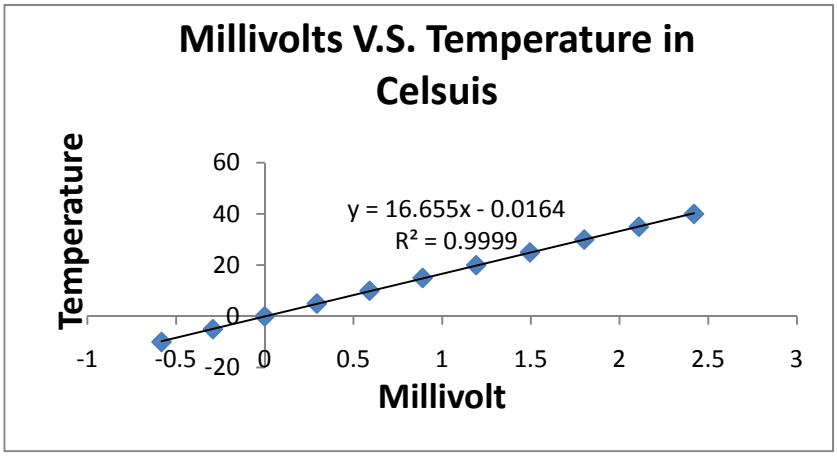

Figure D-1 E-type Thermocouple (Millivolts) V.S. Temperature (°C) curve

By using the calibration curve in Fig.D-1, the actual temperature of each thermocouple is calculated. The temperature of different locations on transitional piece and combustion chamber walls for no-sheath and sheathed case are showing in Table D-3 and Table D-4, respectively. The temperature comparison between no-sheath and sheathed cases is list in Table D-5.

Table D-3 Temperature measurement (K) for no-sheath case

Temperature (K)	TR	TMR	TML	TL	L	BL	BR	R
1	305.45	311.09	311.95	305.78	308.88	310.34	314.78	304.84
2	306.56	309.32	310.34	315.55	308.64	308.47	309.19	305.00
3	308.31	309.98	309.81	315.09	308.16	307.29	308.00	307.00
4	308.54	309.81	309.95	305.33	307.95	307.65	308.43	307.83
5	308.99	309.68	309.59	307.14	307.80	308.00	308.32	307.98
6	309.22	309.56	308.87	308.96	307.66	307.77	308.08	307.99
7	308.83	309.49	308.50	308.66	307.99	307.48	307.95	308.43
8	308.38	309.42	308.80	307.85	307.60	307.62	307.82	308.36
9	307.94	308.14	308.42	307.29	308.07	307.26	307.52	307.71
10	307.39	307.93	307.51	307.37	306.24	306.90	306.92	307.06
upstream	304.72							
downstream	304.57							
inside	315.42							

Table D-4 Temperature measurement (K) for sheathed case

Temperature(K)	TR	TMR	TML	TL	L	BL	BR	R
1	307.92	310.73	307.23	308.60	307.59	305.97	306.12	303.93
2	305.41	307.57	308.58	308.21	307.24	306.81	307.19	303.37
3	304.83	310.41	307.88	307.20	307.64	306.64	305.65	304.98
4	305.34	308.86	308.09	303.90	307.35	305.88	306.26	305.73
5	306.37	307.94	307.83	305.82	307.16	305.12	306.16	305.31
6	306.88	307.01	307.30	307.73	306.71	305.86	306.25	306.84
7	306.42	306.92	307.04	306.99	306.94	305.86	306.23	306.78
8	306.52	306.82	306.74	306.24	306.76	306.01	306.20	306.41
9	306.62	306.53	307.05	306.08	307.29	306.58	306.40	306.29
10	306.31	306.88	306.46	305.97	305.96	306.74	306.64	306.17
upstream	303.52							
downstream	303.27							
inside	314.67							

Table D-5 Experimental temperature comparison between the no-sheath and sheathed case

Temperature	TR		TMR		TML		TL	
(K)	No-shaeth	Sheathed	No-shaeth	Sheathed	No-shaeth	Sheathed	No-shaeth	Sheathed
1	305.45	307.92	311.09	310.73	311.95	307.23	305.78	308.60
2	306.56	305.41	309.32	307.57	310.34	308.58	315.55	308.21
3	308.31	304.83	309.98	310.41	309.81	307.88	315.09	307.20
4	308.54	305.34	309.81	308.86	309.95	308.09	305.33	303.90
5	308.99	306.37	309.68	307.94	309.59	307.83	307.14	305.82
6	309.22	306.88	309.56	307.01	308.87	307.30	308.96	307.73
7	308.83	306.42	309.49	306.92	308.50	307.04	308.66	306.99
8	308.38	306.52	309.42	306.82	308.80	306.74	307.85	306.24
9	307.94	306.62	308.14	306.53	308.42	307.05	307.29	306.08
10	307.39	306.31	307.93	306.88	307.51	306.46	307.37	305.97

Temperature	L		BL		BR		R	
(K)	No-sheath	Sheathed	No-sheath	Sheathed	No-sheath	Sheathed	No-sheath	Sheathed
1	308.88	307.59	310.34	305.97	314.78	306.12	304.84	303.93
2	308.64	307.24	308.47	306.81	309.19	307.19	305.00	303.37
3	308.16	307.64	307.29	306.64	308.00	305.65	307.00	304.98
4	307.95	307.35	307.65	305.88	308.43	306.26	307.83	305.73
5	307.80	307.16	308.00	305.12	308.32	306.16	307.98	305.31
6	307.66	306.71	307.77	305.86	308.08	306.25	307.99	306.84
7	307.99	306.94	307.48	305.86	307.95	306.23	308.43	306.78
8	307.60	306.76	307.62	306.01	307.82	306.20	308.36	306.41
9	308.07	307.29	307.26	306.58	307.52	306.40	307.71	306.29
10	306.24	305.96	306.90	306.74	306.92	306.64	307.06	306.17

Table D-6 CFD temperature comparisons between Case 2(no-sheath, heated) and Case 5 (sheathed, heated)

Temperature (K)	TR		TMR		TML		TL	
	No-sheath	Sheathed	No-sheath	Sheathed	No-sheath	Sheathed	No-sheath	Sheathed
1	321.58	306.00	321.27	312.47	320.73	312.04	319.96	304.71
2	320.67	301.30	319.29	302.70	319.13	302.76	320.18	301.48
3	317.93	306.21	317.22	318.60	317.49	318.59	318.76	306.18
4	317.76	307.66	317.79	322.88	317.94	322.89	318.20	307.67
5	317.68	308.94	317.14	326.28	317.00	326.36	317.27	309.19
6	317.06	311.84	316.84	327.12	316.61	326.16	316.37	308.98
7	315.87	313.40	316.50	329.54	316.77	328.74	316.70	311.00
8	314.81	310.24	316.10	320.73	316.53	320.37	316.09	309.16
9	314.01	309.33	315.22	312.56	316.22	312.89	317.01	310.32
10	313.09	308.58	314.18	313.00	315.41	313.28	316.78	309.41

Temperature (K)	L		BL		BR		R	
	No-sheath	Sheathed	No-sheath	Sheathed	No-sheath	Sheathed	No-sheath	Sheathed
1	319.58	301.04	333.41	302.94	334.49	303.80	321.73	302.76
2	320.71	300.84	331.33	301.93	331.66	301.82	321.37	300.60
3	319.39	300.98	330.02	303.30	329.46	303.32	318.29	300.01
4	318.33	300.07	326.97	304.74	326.67	304.73	317.74	300.05
5	317.41	300.61	324.66	304.59	324.93	304.43	317.95	300.28
6	316.25	300.38	323.05	305.96	323.51	307.87	317.17	304.20
7	316.66	302.13	321.44	309.57	320.90	311.18	315.56	305.34
8	315.88	303.56	320.65	308.96	319.79	309.68	314.17	305.00
9	317.41	309.04	321.64	310.89	319.64	310.23	313.41	307.72
10	317.47	307.47	320.03	308.74	317.57	308.19	312.54	306.37

APPENDIX E

THERMOCOUPLE TEMPERATURE MEASUREMENT INSTRUCTION

Step by step instructions on how to take thermocouple measurements in the ECCC's lab

Computer: ECCC 11, with 2 Keithley 2700 Multimeters

Turn on computer. A Linux boot loader menu will appear, you must use the arrows to choose 'windows' before it automatically boots into Linux. If it does this, you can hit CTRL-ALT-DEL to restart the machine.

Log into the system use 'nkakafuah' as user name and a blank as password. This is the user account that the necessary software is installed under. The software does not work under all user accounts, and reinstalling it to be used under different accounts can cause problems.

Make sure that the Keithley instruments are on and working normally. According to Keithley, rated accuracy is achieved after the instruments have been on and warmed up, which takes 2 hours.

Open Excel. In the menu bar you will see an additional ExceLINX menu which you will use to control the instruments.

Click **ExceLINX > Create > Configure Scanning DMM Channels** to start.

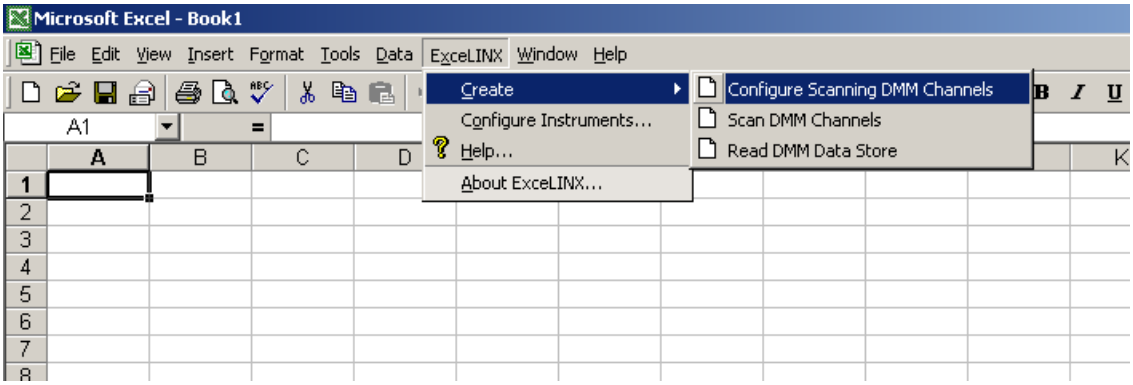

Excel will create a new sheet in the open spreadsheet which looks like this:

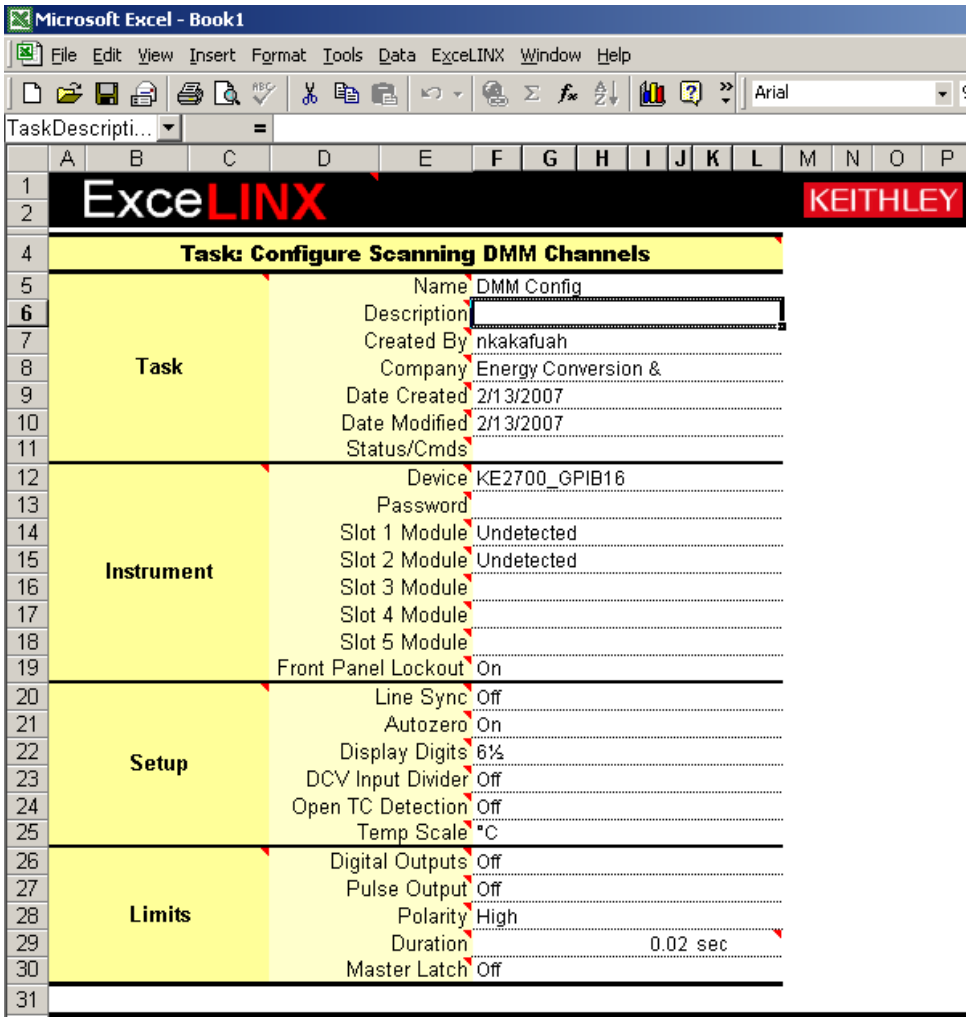

Look in the instrument table, under ‘Device’, and you will see the default device KE2700_GPIB16, which is the wrong instrument. This is changed by clicking to the right of this cell, and pulling the correct instrument from the drop down menu. The correct instruments are **KE2700_COM1** and **KE2700_COM2**. Only one instrument can be used per sheet, so select the first one.

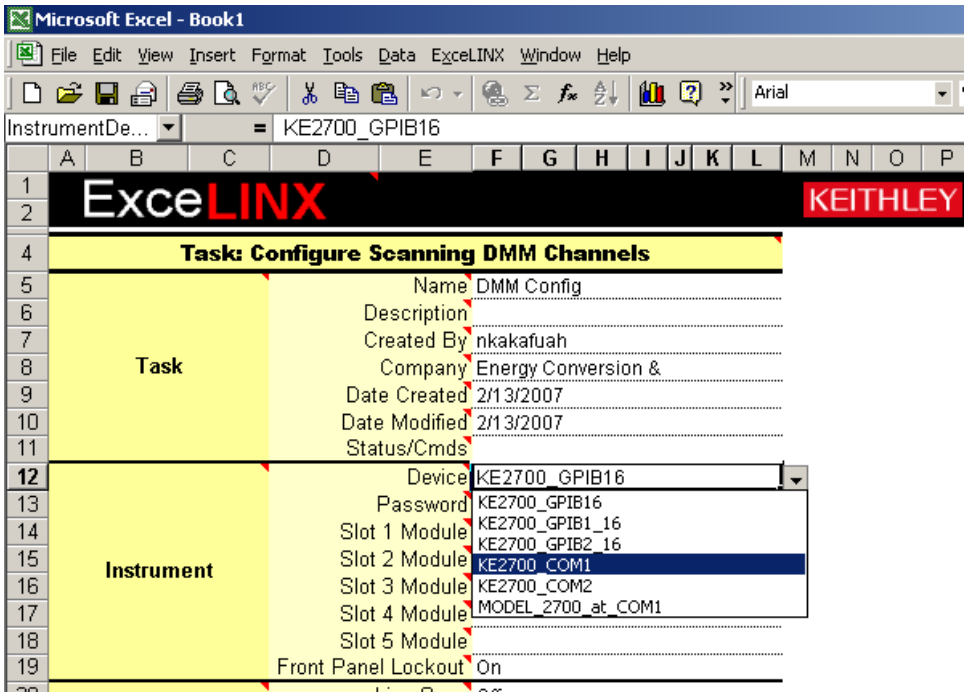

Once you have chosen the correct instrument, click **ExceLINX > DMM Config > Detect Device** to let the software see and configure the device.

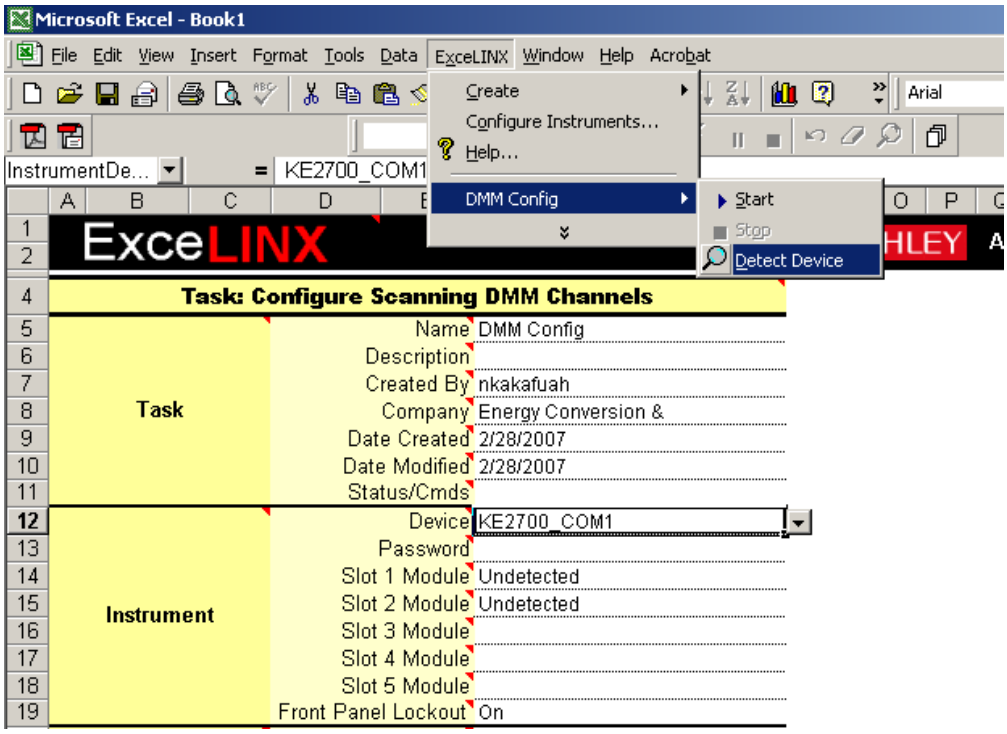

If all goes well the module numbers will appear, although this is strictly not necessary, data can be collected if the modules are undetected, but you still must go through the step of detecting the device.

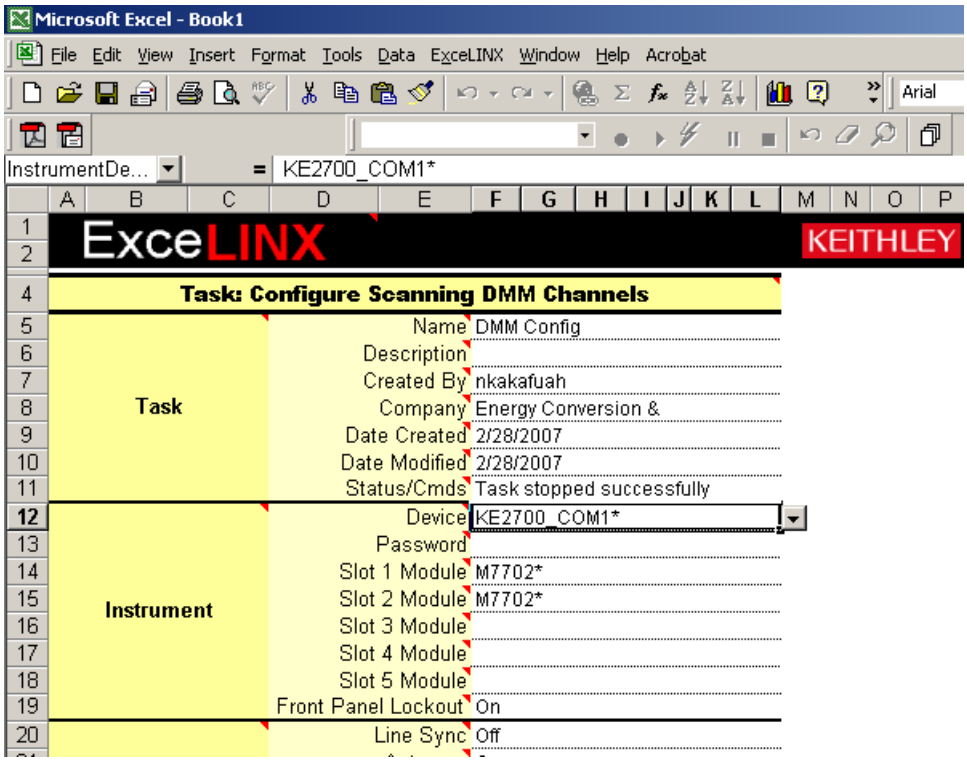

There are two sets of channels: 101-140 and 201-240. They must be changed in the list as follows:

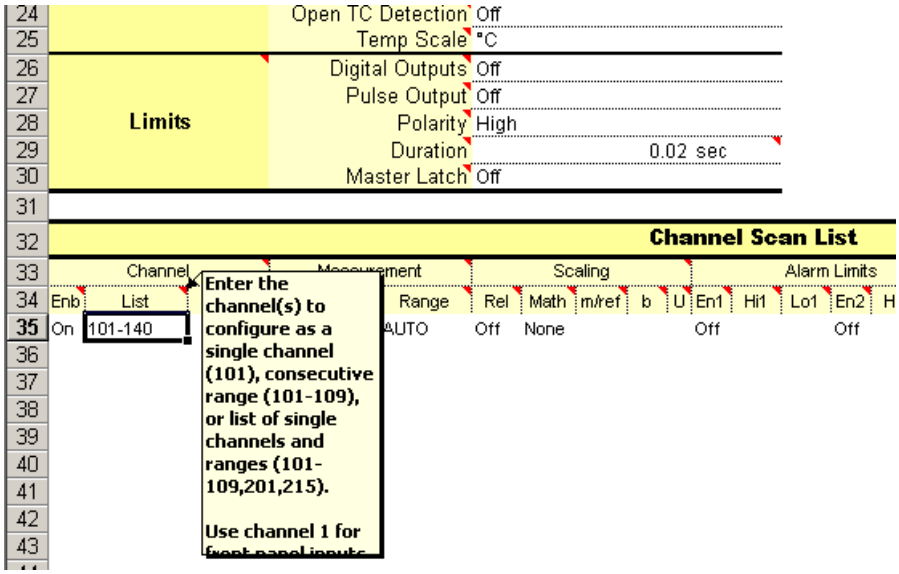

Other settings, such as scan speed, can also be changed here. The different rates are: Slow (12 Hz), Med (60 Hz) and Fast (600 Hz). See also the Keithley manual, in the Range, Digits, Rate, Bandwidth, and Filter chapter, under Rate and Bandwidth.

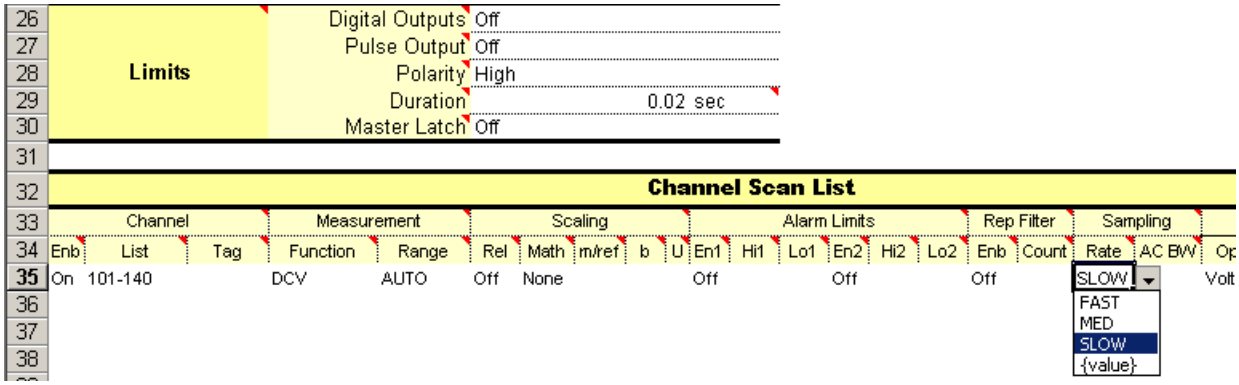

You must add the second set of channels manually. Enter the numbers in the list column, Click 'ON' in the 'Enb' column to the left, and click 'DCV' in the 'Function' column, and the rest of the row should get filled in. Set the sampling rate and anything else, if needed.

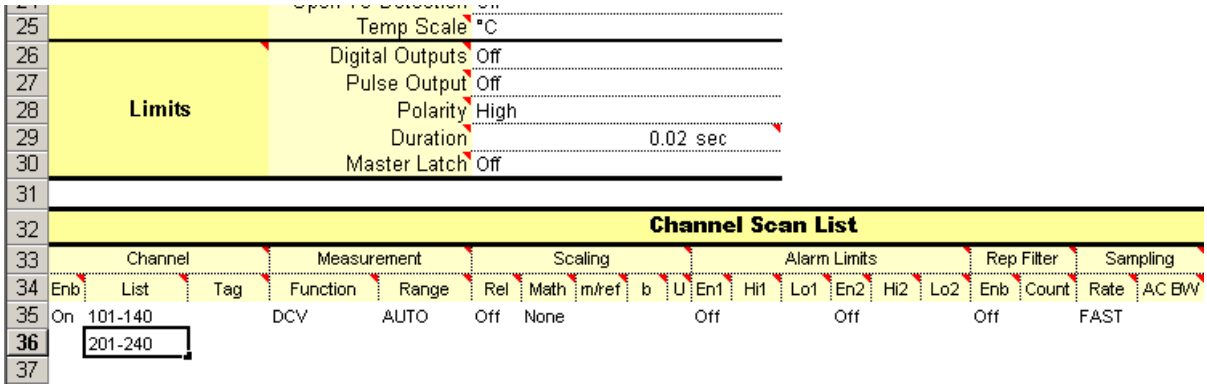

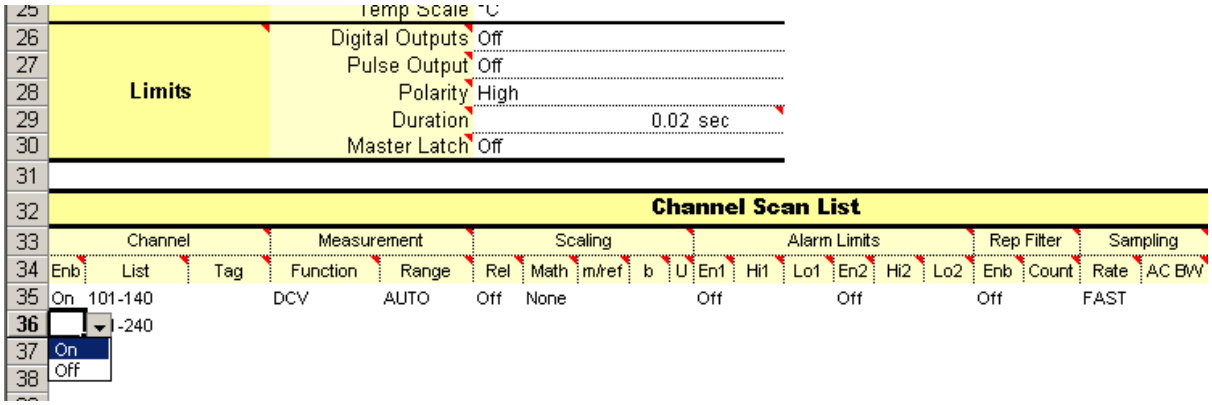

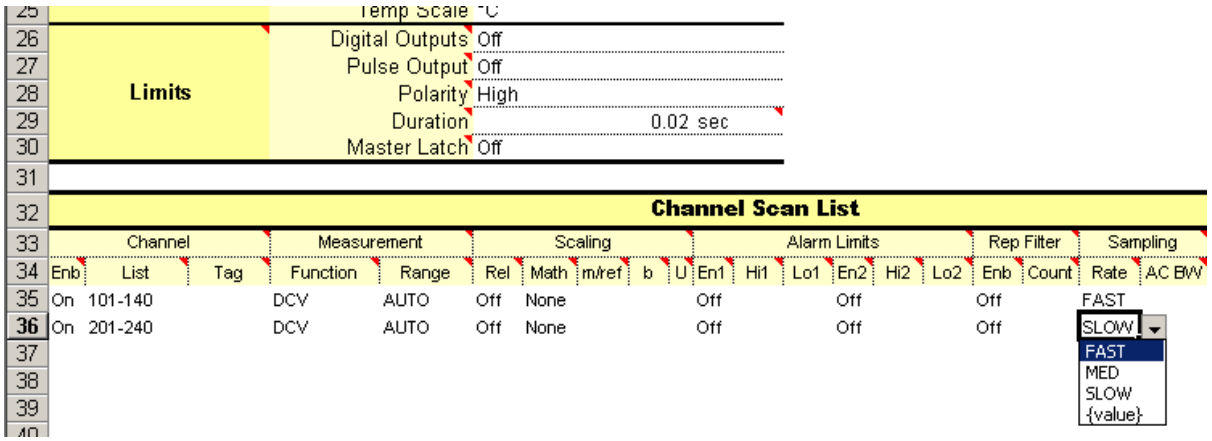

Once this is done, the device is configured. To create a scanning sheet, click **ExceLINX > Create > Scan DMM Channels**:

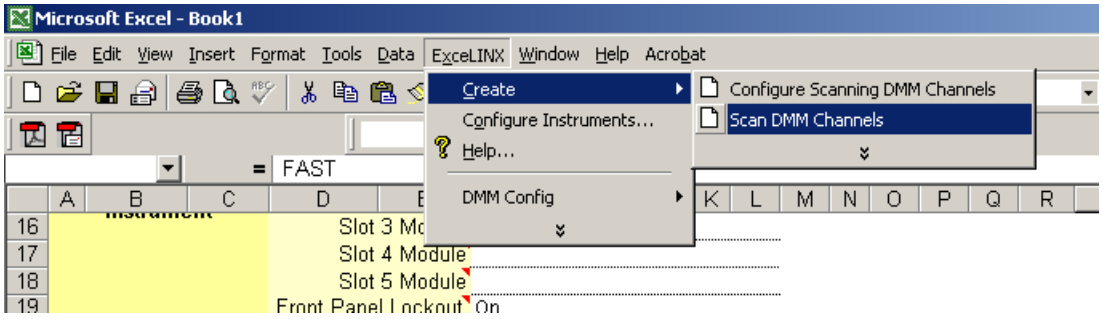

A new sheet appears. This sheet is where you can configure the data that will be collected. You can set the number of times to scan (1 – infinite), where to place the data (the default is in the same worksheet, but it can be put into a separate worksheet), how to arrange the data, etc.

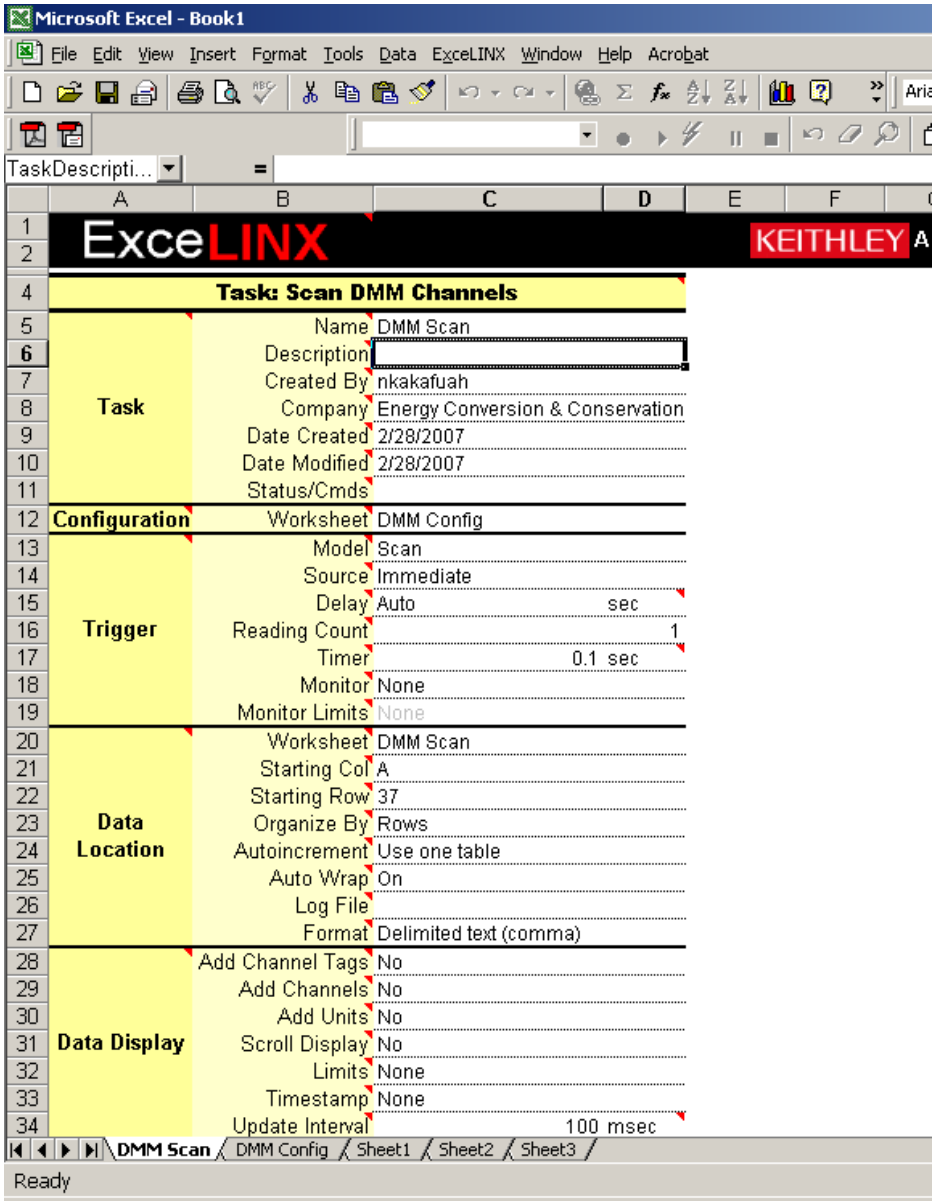

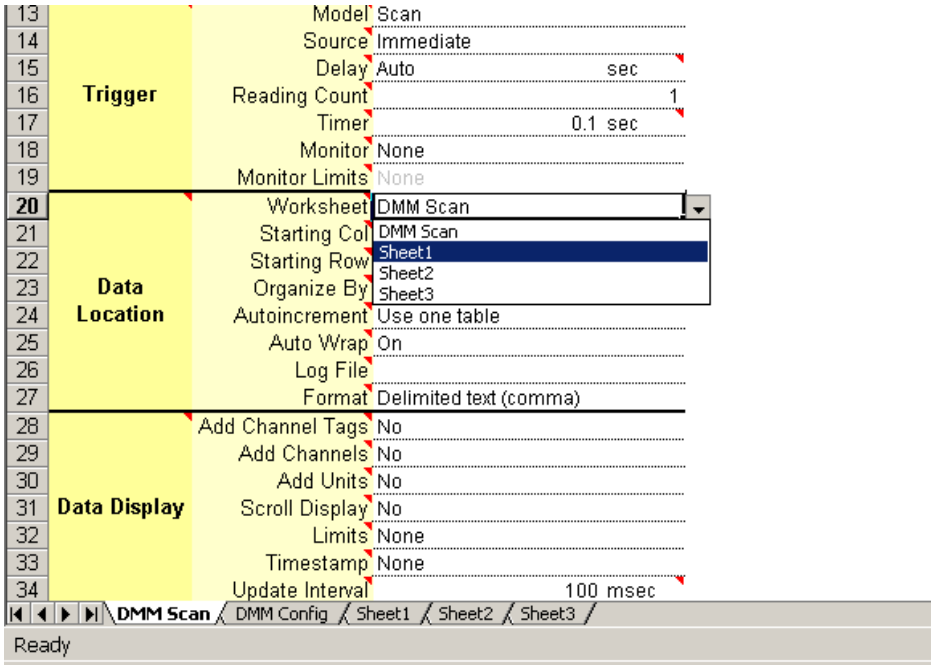
13 Model Scan
14 Source Immediate
15 Delay Auto sec
16 Trigger Reading Count 1
17 Timer 0.1 sec
18 Monitor None
19 Monitor Limits None
20 Worksheet DMM Scan
21 Starting Col
22 Starting Row
23 Data Organize By
24 Location Autoincrement Use one table
25 Auto Wrap On
26 Log File
27 Format Delimited text (comma)
28 Add Channel Tags No
29 Add Channels No
30 Add Units No
31 Data Display Scroll Display No
32 Limits None
33 Timestamp None
34 Update Interval 100 msec
DMM Scan
DMM Scan
Sheet1
Sheet2
Sheet3
DMM Scan DMM Config Sheet1 Sheet2 Sheet3
Ready

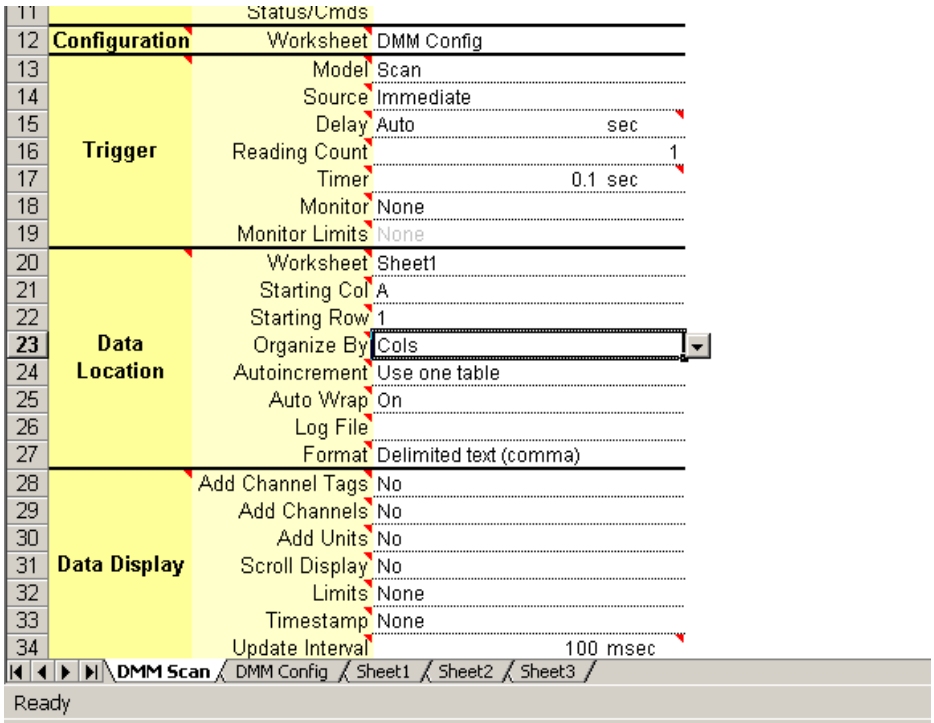
Status/Cmds
12 Configuration Worksheet DMM Config
13 Model Scan
14 Source Immediate
15 Delay Auto sec
16 Trigger Reading Count 1
17 Timer 0.1 sec
18 Monitor None
19 Monitor Limits None
20 Worksheet Sheet1
21 Starting Col A
22 Starting Row 1
23 Data Organize By Cols
24 Location Autoincrement Use one table
25 Auto Wrap On
26 Log File
27 Format Delimited text (comma)
28 Add Channel Tags No
29 Add Channels No
30 Add Units No
31 Data Display Scroll Display No
32 Limits None
33 Timestamp None
34 Update Interval 100 msec
DMM Scan DMM Config Sheet1 Sheet2 Sheet3
Ready

The same procedure must be done for the second instrument. Follow the same procedure, and the worksheets for this instrument will have a (2) in the names so that they can be kept track of.

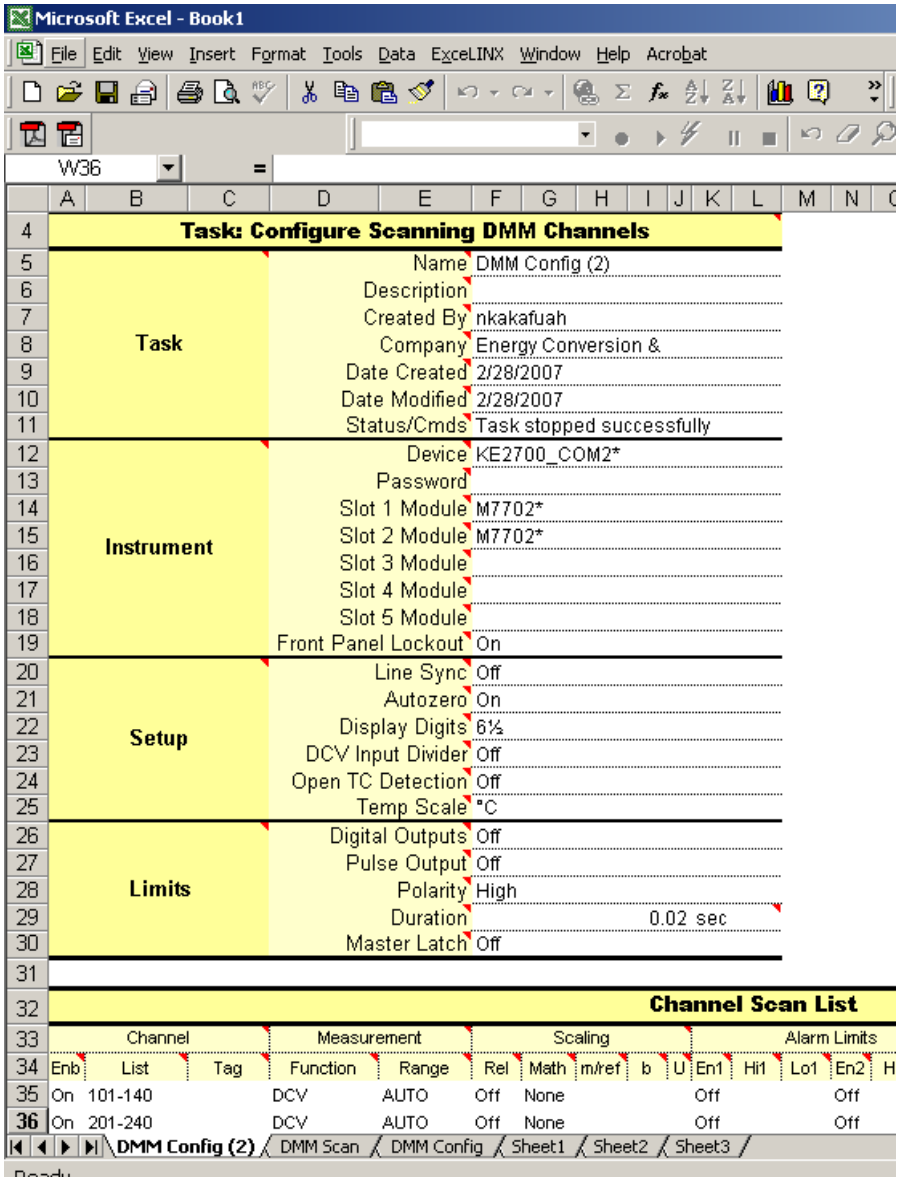

To begin taking data, click **ExceLINX > DMM Scan > Start**.

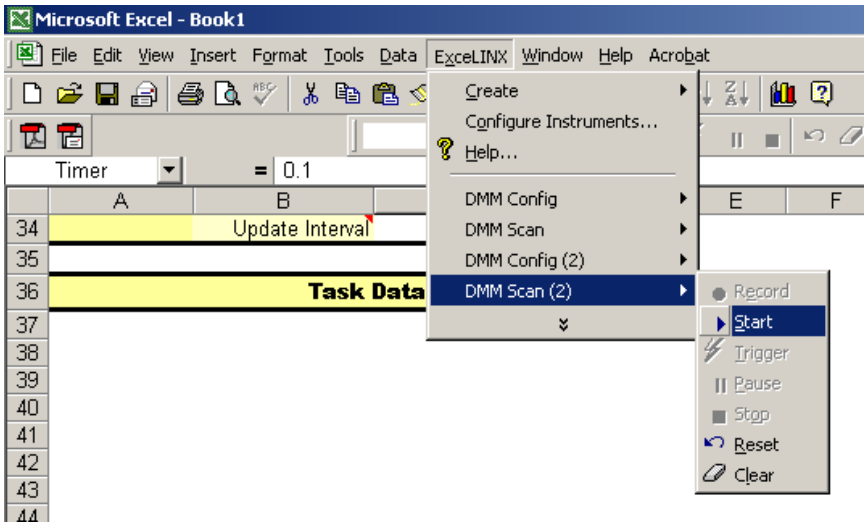

Data will be collected and entered into the spreadsheet as it was configured to be earlier:

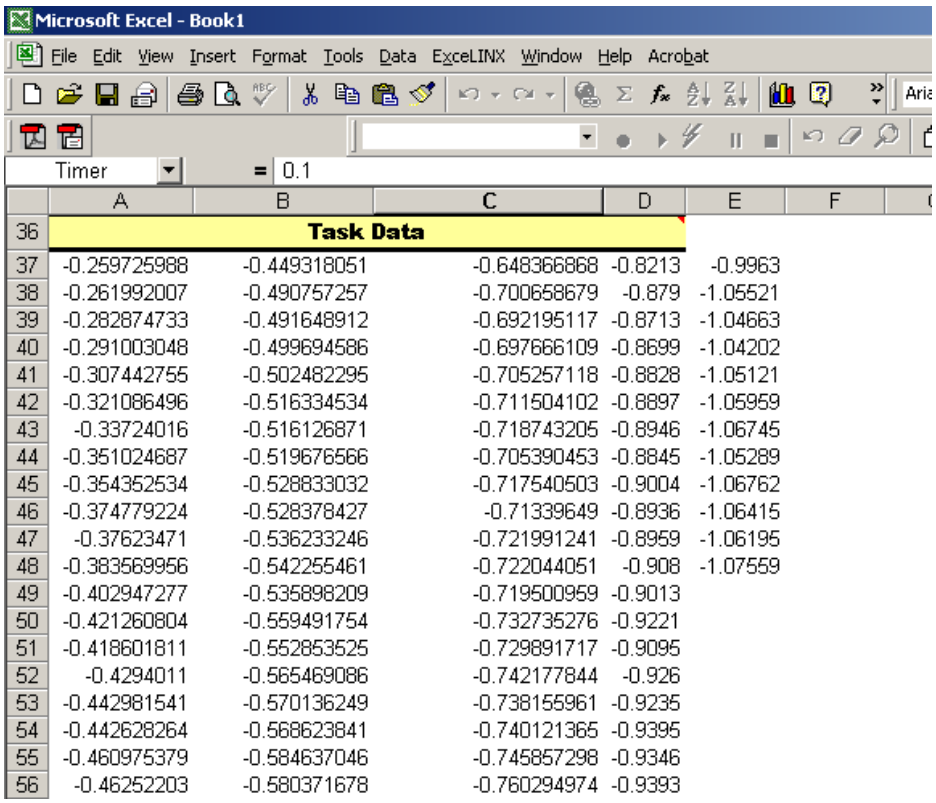

	A	B	C	D	E	F
36	Task Data					
37	-0.259725988	-0.449318051	-0.648366868	-0.8213	-0.9963	
38	-0.261992007	-0.490757257	-0.700658679	-0.879	-1.05521	
39	-0.282874733	-0.491648912	-0.692195117	-0.8713	-1.04663	
40	-0.291003048	-0.499694586	-0.697666109	-0.8699	-1.04202	
41	-0.307442755	-0.502482295	-0.705257118	-0.8828	-1.05121	
42	-0.321086496	-0.516334534	-0.711504102	-0.8897	-1.05959	
43	-0.33724016	-0.516126871	-0.718743205	-0.8946	-1.06745	
44	-0.351024687	-0.519676566	-0.705390453	-0.8845	-1.05289	
45	-0.354352534	-0.528833032	-0.717540503	-0.9004	-1.06762	
46	-0.374779224	-0.528378427	-0.71339649	-0.8936	-1.06415	
47	-0.37623471	-0.536233246	-0.721991241	-0.8959	-1.06195	
48	-0.383569956	-0.542255461	-0.722044051	-0.908	-1.07559	
49	-0.402947277	-0.535898209	-0.719500959	-0.9013		
50	-0.421260804	-0.559491754	-0.732735276	-0.9221		
51	-0.418601811	-0.552853525	-0.729891717	-0.9095		
52	-0.4294011	-0.565469086	-0.742177844	-0.926		
53	-0.442981541	-0.570136249	-0.738155961	-0.9235		
54	-0.442628264	-0.568623841	-0.740121365	-0.9395		
55	-0.460975379	-0.584637046	-0.745857298	-0.9346		
56	-0.46252203	-0.580371678	-0.760294974	-0.9393		

VITA

Liang Wang was born in China in 1980. He completed his Bachelors of Mechanical Engineering from Tongji University, China in 2003. He rerolled for a Master program into the University of New Orleans in 2007.